APPLICATION OF PALEOENVIRONMENTAL DATA FOR TESTING CLIMATE MODELS AND UNDERSTANDING PAST AND FUTURE CLIMATE VARIATIONS

by

KENJI IZUMI

A DISSERTATION

Presented to the Department of Geography
and the Graduate School of the University of Oregon
in partial fulfillment of the requirements
for the degree of
Doctor of Philosophy

September 2014

DISSERTATION APPROVAL PAGE

Student: Kenji Izumi

Title: Application of Paleoenvironmental Data for Testing Climate Models and Understanding Past and Future Climate Variations

This dissertation has been accepted and approved in partial fulfillment of the requirements for the Doctor of Philosophy degree in the Department of Geography by:

Patrick Bartlein	Chairperson
Daniel Gavin	Core Member
W. Andrew Marcus	Core Member
Sarah Shafer	Core Member
Joshua Roering	Institutional Representative

and

J. Andrew Berglund	Dean of the Graduate School

Original approval signatures are on file with the University of Oregon Graduate School.

Degree awarded September 2014

DISSERTATION ABSTRACT

Kenji Izumi

Doctor of Philosophy

Department of Geography

September 2014

Title: Application of Paleoenvironmental Data for Testing Climate Models and Understanding Past and Future Climate Variations

Paleo data-model comparison is the process of comparing output from model simulations of past periods with paleoenvironmental data. It enables us to understand both the paleoclimate mechanism and responses of the earth environment to the climate and to evaluate how models work. This dissertation has two parts that each involve the development and application of approaches for data-model comparisons. In part 1, which is focused on the understanding of both past and future climatic changes/variations, I compare paleoclimate and historical simulations with future climate projections exploiting the fact that climate-model configurations are exactly the same in the paleo and future simulations in the Coupled Model Intercomparison Project Phase 5. In practice, I investigated large-scale temperature responses (land-ocean contrast, high-latitude amplification, and change in temperature seasonality) in paleo and future simulations, found broadly consistent relationships across the climate states, and validated the responses using modern observations and paleoclimate reconstructions. Furthermore, I examined the possibility that a small set of common mechanisms controls the large-scale temperature responses using a simple energy-balance model to decompose the temperature changes shown in warm and cold climate simulations and found that the clear-sky longwave downward radiation is a key control of the robust responses.

In part 2, I applied the equilibrium terrestrial biosphere models, BIOME4 and BIOME5 (developed from BIOME4 herein), for reconstructing paleoclimate. I applied inverse modeling through the iterative forward-modeling (IMIFM) approach that uses the North American vegetation data to infer the mid-Holocene (MH, 6000 years ago) and the Last Glacial Maximum (LGM, 21,000 years ago) climates that control vegetation distributions. The IMIFM approach has the potential to provide more accurate quantitative climate estimates from pollen records than statistical approaches. Reconstructed North American MH and LGM climate anomaly patterns are coherent and consistent between variables and between BIOME4 and BIOME5, and these patterns are also consistent with previous data synthesis.

This dissertation includes previously published and unpublished coauthored material.

CURRICULUM VITAE

NAME OF AUTHOR: Kenji Izumi

GRADUATE AND UNDERGRADUATE SCHOOLS ATTENDED:

University of Oregon, Eugene
Nagoya University, Nagoya, Japan

DEGREES AWARDED:

Doctor of Philosophy, Geography, 2014, University of Oregon
Master of Science, Climate Science in Graduate School of Environmental Studies, 2008, Nagoya University
Bachelor of Science, Environmental Science, 2005, University of Oregon

AREAS OF SPECIAL INTEREST:

Large-scale climate changes in the past, present, and future
Paleo data-model comparison
Reconstruction of paleoclimate with a process-based vegetation model
Modification of an equilibrium vegetation model, BIOME5

PROFESSIONAL EXPERIENCE:

Research Assistant, Department of Geography, University of Oregon, 2008-2014

Research Assistant, College of Earth, Ocean, and Atmospheric Science, Oregon State University 2013

GRANTS, AWARDS, AND HONORS:

The Leverhulme Trust Travel Grant, the PMIP3 General Meeting (Namur, Belgium), 2014

Best young scientist (grad students and post-docs) poster at the PMIP3 General Meeting (Crewe, UK), 2012

PUBLICATIONS:

Izumi K, Bartlein P, and Harrison S (2014) Energy-balance mechanisms underlying consistent large-scale temperature responses in warm and cold climates. Climate Dynamics:1-17. doi:10.1007/s00382-014-2189-2

Izumi K, Bartlein PJ, and Harrison SP (2013) Consistent large-scale temperature responses in warm and cold climates. Geophysical Research Letters 40 (9):1817-1823. doi:10.1002/grl.50350

Harrison SP, Bartlein PJ, Brewer S, Prentice IC, Boyd M, Hessler I, Holmgren K, Izumi K, and Willis K (2013) Climate model benchmarking with glacial and mid-Holocene climates. Climate Dynamics:1-18. doi:10.1007/s00382-013-1922-6

Li G, Harrison SP, Bartlein PJ, Izumi K, and Colin Prentice I (2013) Precipitation scaling with temperature in warm and cold climates: An analysis of CMIP5 simulations. Geophysical Research Letters 40 (15):4018-4024. doi:10.1002/grl.50730

Daniau AL, Bartlein PJ, Harrison SP, Prentice IC, Brewer S, Friedlingstein P, Harrison-Prentice TI, Inoue J, Izumi K, Marlon JR, Mooney S, Power MJ, Stevenson J, Tinner W, Andric M, Atanassova J, Behling H, Black M, Blarquez O, Brown KJ, Carcaillet C, Colhoun EA, Colombaroli D, Davis BAS, D'Costa D, Dodson J, Dupont L, Eshetu Z, Gavin DG, Genries A, Haberle S, Hallett DJ, Hope G, Horn SP, Kassa TG, Katamura F, Kennedy LM, Kershaw P, Krivonogov S, Long C, Magri D, Marinova E, McKenzie GM, Moreno PI, Moss P, Neumann FH, Norstrom E, Paitre C, Rius D, Roberts N, Robinson GS, Sasaki N, Scott L, Takahara H, Terwilliger V, Thevenon F, Turner R, Valsecchi VG, Vanniere B, Walsh M, Williams N, and Zhang Y (2012) Predictability of biomass burning in response to climate changes. Global Biogeochemical Cycles 26. doi:10.1029/2011gb004249

ACKNOWLEDGMENTS

I wish to express sincere appreciation to Patrick Bartlein, Dan Gavin, Andrew Marcus, Sarah Shafer, and Josh Roering for their valuable feedback throughout the course of this dissertation work. In addition, special thanks are due to Sandy Harrison and Jed Kaplan for the development of my research.

TABLE OF CONTENTS

LIST OF FIGURES

LIST OF TABLES

CHAPTER I

INTRODUCTION

This thesis focuses in general on *paleo data-model comparison* – the process of comparing the output from paleoclimate simulations with paleoenvironmental data. Such comparisons enable us to understand the mechanisms responsible for paleoclimate variations and the responses of different environmental systems to those variations, and also allow us to evaluate how well climate models work (Harrison 2013).

Paleoenvironmental data record how climate has changed. But data alone cannot give an adequate explanation as to why a particular climate condition occurred or has changed, because most climatic variations have multiple causes, and because environmental systems generally show nonlinear responses to climate variations (Bartlein and Hostetler, 2003). In contrast, paleoclimate modeling can give consistent explanations of past climate changes (Schmidt 2010), but only if the models used are known to work. Climate models also provide a unique method for projecting future climates, and their capabilities and limitation have to be quantitatively evaluated. We generally evaluate a model's ability under the present climate state. Although the simulations of the modern climate can be compared with global data sets such as satellite remote sensing and reanalysis data, the data in the instrumental period includes smaller climate variations than those possible in the future (Fig. 1.1). In order to project future climate under potential larger forcings than those experienced in the instrumental period, we need to understand the climate responses to larger external forcings and to different internal boundary conditions, and examples of such are provided in the paleoclimatic record. Therefore, paleo data-model comparison also provides support for the projection of future climate while also furthering scientific understanding of past climate changes.

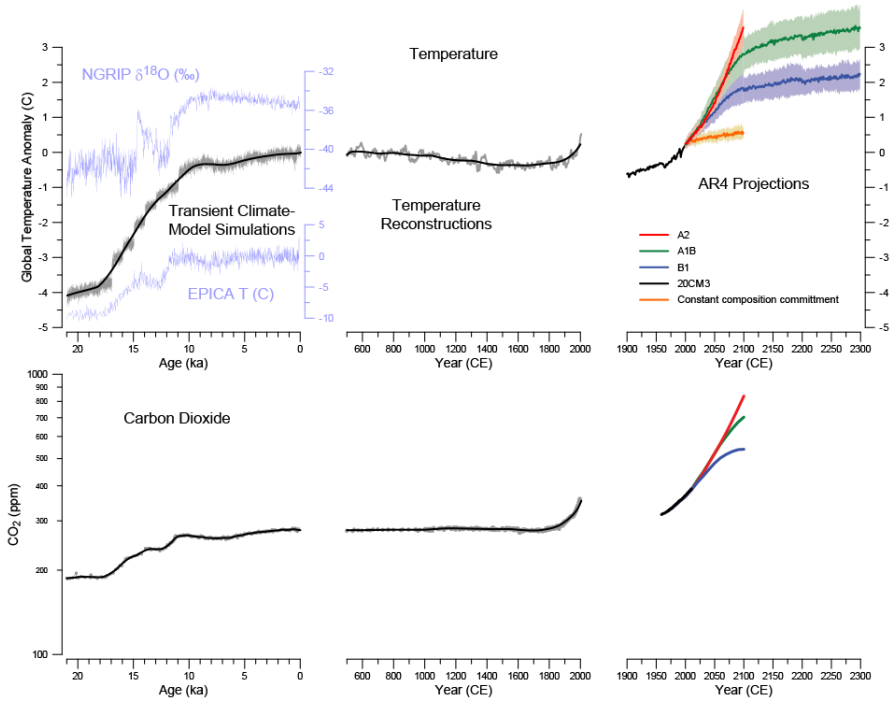

Figure 1.1. Estimates of global average temperature estimates (from paleo/future transient simulations and reconstructions) and atmospheric CO_2 concentration for the last 21ka and future

1. Modeling of past climates

The climate system is a complex, interactive system consisting of the atmosphere, hydrosphere, cryosphere, biosphere, and land-surface. Climate models that attempt to simulate the climate system evolved from atmosphere and ocean general circulation models (GCMs). GCMs are tools used for calculating the three-dimensional (3D) character of the atmosphere and ocean. Such models produce solutions of a set of differential equations (temporal and spatial derivatives) for three conservation laws (mass, momentum, and energy), the ideal gas law, and other dynamical and physical processes (Washington and Parkinson, 2005). In order to solve these equations in the time dimension, a set of initial conditions for the variables in 3D are also required, as well as a set of "boundary conditions" that include the time-varying controls of climate, like incoming solar radiation (insolation) or the composition of the atmosphere. Once

these initial and boundary conditions are known, the change of tendency terms in the equations can be solved to produce a new set of values for the next time step. Both the length of the time step and the spatial resolution of the grid points influence the accuracy of the model simulation (McGuffie and Henderson-Sellers, 2005). Processes that cannot be treated explicitly because they are sub-grid in scale are represented by parameterizations, and these are present in all models.

As for modern and future climate simulations, general circulation models (GCMs) have been used to simulate past climate changes. However, paleoclimate modeling has long faced the constraints of the computing power necessary to depict long time periods from the past in detail. One solution was to generate snapshots that focus on key periods in past climate (often using GCMs that had lower resolution and were older versions the standard models) (Braconnot et al. 2012). Another solution has been to carry out transient/continuous runs with Earth-system Models of Intermediate Complexity (EMICs; Claussen et al., 2002). EMICs provide some big-picture insights on climate variations, but they cannot represent some important processes because of very low spatial and temporal resolution of the models.

Climate: Long range Investigation, Mapping, and Prediction (CLIMAP; CLIMAP Project Members, 1976, 1981) was the first global project for data synthesis and was designed among other things to reconstruct the surface conditions at the Last Glacial Maximum (LGM: ca 21000 yr BP or 21 ka). Williams et al. (1974), Gates (1976) and Rind and Peteet (1985) ran atmospheric general circulation models (AGCMs) using boundary conditions from CLIMAP reconstructions. Broccoli and Manabe (1987) compared simulated SST with CLIMAP SSTs. The Cooperative Holocene Mapping Project (COHMAP; COHMAP Members, 1988) was the first international collaborative project for studying past climate changes using paleo data-model comparisons as a key element of a research design that included simulations of several past climatic states. The goal of the project was to understand the mechanisms of late Quaternary climate changes,

and AGCM simulations showed that both broad-scale spatial patterns and the temporal evolution of climate over the monsoon regions, in particular northern Africa, could be explained to first order as a consequence of orbital forcing (COHMAP Members, 1988; Kutzbach et al. 1993).

By the early 1990s several modeling groups had done paleo experiments, using different models and different external forcing. But, because different modeling groups did not always use the same external forcing or internal boundary conditions, there were different results among the models, and thus it was difficult to diagnose the causes of both data-model disagreement and differences among models.

To understand the causes of such intermodel differences, the Paleoclimate Modelling Intercomparison Project (PMIP; Joussaume et al., 1999) was established. In PMIP, all modeling groups used the identical forcing and boundary conditions for simulating the LGM and the mid-Holocene (MH: ca. 6000 yr BP or 6 ka) climates that are recognized as key targets for benchmarking climate models because there were a number of existing paleodata that could be used to produce well-documented large-scale data syntheses, and the nature of the boundary conditions at these times led to relatively "clean" experiments. The LGM simulations were designed to examine the climate response to the presence of large ice sheets, cold oceans, and lowered greenhouse gas concentration, leading to a large surface cooling over the ice sheets in Northern Hemisphere and a large-scale drying in both hemispheres. The MH simulations were designed to examine the climate response to a change in the seasonal and latitudinal distribution of incoming solar radiation caused by known changes in orbital forcing. These changes lead to an enhanced seasonal cycle of temperature in the Northern Hemisphere and reduced seasonal cycle of temperature in the Southern Hemisphere.

In PMIP2, coupled ocean-atmosphere models (OAGCMs) and ocean-atmosphere-vegetation models (OAVGCMs) were adopted for paleoclimate simulations (e.g. Braconnot et al., 2007a & 2007b). Some modeling was also underway to incorporate new

sub-system components, such as dynamic vegetation, interactive atmospheric chemistry, and interactive ice sheets. Moreover, by devoting an entire chapter of the Fourth Assessment Report (AR4; Solomon et al., 2007) to paleoclimate, the Intergovermenal Panel on Climate Change (IPCC) recognized that studying past climates is essential for comprehending the climate system, and thus for predicting the future climate. Because each climate-modeling group adopted different temporal and spatial resolutions and different parameterization schemes, the simulation results differ among the models, but PMIP2 provided the opportunity to examine multi-model ensembles and to analyze the causes of differences in model ability to reproduce observed climate changes in the past.

In PMIP3 (Braconnot et al., 2012), most project members ran the Coupled Model Intercomparsion Project Phase 5 (CMIP5; Taylor et al., 2012) paleoclimate simulations, such as those for the mid Holocene (MH), last glacial maximum (LGM), and last millennium (LM), with the same model components and the same resolution as used for the projections of future climate. These "CMIP5/PMIP3" simulations thus allow us to examine the climate responses in a systematic fashion across a range of climate states (e.g. Izumi et al. 2013). Furthermore, PMIP3 initiates several new simulations; the last millennium (Schmidt et al. 2012), the last interglacial (LIG, ca. 129~116 ka), mid-Pliocene (ca. 3.3~3.0 Ma; Haywood et al. 2010; Haywood et al. 2011), and abrupt climate changes (the 8.2 ka event and Younger Dryas 12.9 to 11.7 ka). Participants in the PMIP3 workshop in Namur, Belgium (2014) put more focus on examining different model sensitivities to the evolving climate forcing, ascertaining the time-evolving boundary conditions and forcing for climate simulations, and understanding physical mechanisms of climate changes between different climate states.

2. Data syntheses of past climates

The major paleoenvironmental data that have been synthesized for paleo data-model comparisons include terrestrial paleoecological data (pollen, plant macrofossil,

charcoal and tree-rings), geological data (borehole temperatures, lake levels, loess, and speleothem records), ice-core data, and marine data (from corals, marine microfossils), and these "proxy" data can be interpreted in climatic terms by various methods (Bradley 2014). These paleoclimate reconstructions are most often achieved based on data from a single location, and the proxy data are often representative of single site (Bradley 2014). Therefore, important tasks are to develop methodologies for dealing with these different characteristics and to make global data syntheses for data-model comparison. A variety of paleoclimate modeling simulations, in particular transient simulations with GCMs, have recently been conducted, and thus global data synthesis for evaluating these model results is also required.

Paleoenvironmental data enter into climate modeling in two different ways: as boundary conditions and as data sets for evaluating model output (Kohfeld and Harrison, 2000). Boundary conditions are prescribed characteristics of components of the earth system that are not explicitly simulated (e.g. ICE 6G for ice sheet extent and height; Toscano et al. 2011). Although the reconstructions for boundary conditions are initially based on paleoenvironmental data from individual sampling sites, they are spatially generalized to model resolution. In practice, the data sets used to specify boundary conditions should not be generally used for evaluation of the same experiment in order to avoid circularity in the data-model comparison process (Kohfeld and Harrison, 2000).

Large-scale data syntheses for data-model comparison are required in order to describe the diagnostic spatial patterns of key climate change mechanisms, and these data sets should have some desirable characteristics (Kohfeld and Harrison, 2000): (1) The data set should be continent- (or ocean basin-) wide to global extent in order to distinguish the changes in large-scale paleoenvironmental condition. (2) The data set should contain information that can be precisely located in time, and the time window should be limited to some extent. (3) The data set should be in a form that is directly comparable with climate model output or should be readily interpreted in terms of

climate variables by the model. If sub-system models, such as those for the terrestrial biosphere and dust cycle, are used, their output (i.e., vegetation type and dust deposition rate) can also be used in a model comparison. 4) The sources (including locations) of the primary data should be transparent to the user in order to minimize the uncertainties associated with extrapolation of information to regions without sufficient spatial coverage of data. 5) The data set should be adequately documented and publicly accessible because data users have to understand the assumption underlying transformation of the primary data and the transformation methods. 6) The data set should provide adequate metadata (e.g. site information and quality of chronology) in order to allow users to select data for a specific model comparison.

There are several global paleoclimate and paleoenvironmental data syntheses for data-model comparison (Table 1): Global Charcoal Database (GCD; Daniau et al. 2012; Power et al. 2010) for changes in fire regimes, the Paleovegetation Mapping Project (generally known as BIOME6000; Prentice and Webb, 1998) for changes in vegetation distribution, the Global Lake Status Database (GLSDB; Kohfeld and Harrison, 2000) for changes in regional water budgets, the Global Holocene Spatial and Temporal Climate Variability global database (GHOST; Kim and Schnider, 2004; Leduc et al., 2010) for alkenone-derived sea surface temperature, the Multiproxy Approach for the Reconstruction of the Glacial Ocean (MARGO) project (Kucera, 2005; MARGO Project Members, 2009) for sea surface temperature, the multiproxy estimate of marine productivity data (Kohfeld et al. 2005), and the global synthesis of quantitative climate reconstructions based on the pollen and plant macrofossil data (Bartlein et al. 2011).

Table 1.1. Global data syntheses for paleo data-model comparison

Data set (references)	Variable	Period coverage
BIOME 6000 (Prentice and Webb, 1998)	Major vegetation types based on pollen and plant macrofossil data	0ka, 6ka, and 21ka
GCD ((GCD; Daniau et al. 2012; Power et al. 2010)	Fire regime based on charcoal	Past 200,000 years BP to present
GLSDB (Kohfeld and Harrison, 2000)	Lake-level changes	Past 30,000 years BP to present
DIRTMAP (Kohfeld and Harrison, 2001)	Mineral dust deposition rates	Past 150,000 years BP to present
MARGO (Kucera, 2005; MARGO Project Members, 2009)	Sea surface temperature (SST) from multiproxy	21 ka
GHOST (Kim and Schnider, 2004; Leduc et al., 2010)	Alkenone-derived SST	Holocene
Bioclimatic variables (Bartlein et al., 2011)	Terrestrial bioclimatic variables based on pollen and macrofossil	6ka and 21ka

3. Paleo data-model comparison

There are two basic approaches for comparing paleodata and paleoclimate simulations: inverse-modeling approaches and forward-modeling approaches (Fig. 1.2). Moreover, two of the approaches can be combined as "Inverse modeling through iterative forward modeling". The three approaches that are described below can be summarized in a schematic fashion as:

Inverse modeling:
Paleodata → statistical model → climate reconstructions ↔ climate-model output

Forward modeling:
Climate-model output → process model → simulated paleodata ↔ observed paleodata

Inverse modeling through iterative forward modeling:
Climate data → process model → simulated paleodata ↔ observed paleodata
↖ choose new climate values and iterate until agreement ↙

where the double-headed arrow (↔) indicates data-model comparison.

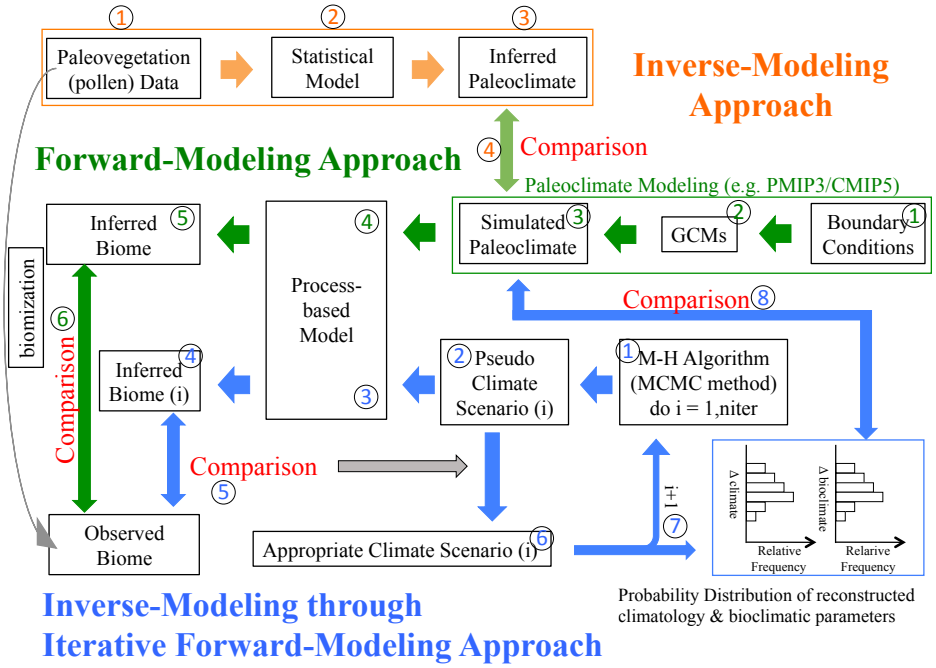

Figure 1.2. Schematic diagram of paleo data-model comparison for using pollen data. Inverse-modeling approach (orange text) and forward-modeling approach (green text) are general methods of the comparisons. The term "inverse" is used because the flow of cause and effect (i.e. climatic variations/changes cause responses in paleoclimate indicator) is conceptually inverted in order to infer from the responses of the nature of the causes. Inverse-Modeling through Iterative Forward-Modeling Approach (blue text) has recently been developed for paleoclimate reconstruction from pollen data (e.g., Guiot et al. 2000; Wu et al. 2007). Each approach starts at (1). More information about each process is described in the text.

3.1. Inverse-modeling approach

The inverse-modeling approach, or simply the inverse approach (a bottom-up approach) has been the classical approach in paleoclimate analysis. Paleoclimate data, in the form of geological or paleoecological records, derive from Earth processes that are controlled by climate, and thus the evidence left by these processes acts as a 'proxy' for actual measurements of past conditions (Bradley, 2014). Paleoenvironmental data include records of such phenomena as changes in terrestrial vegetation composition, lake level, lake status, and dust deposition, which have been closely shaped by climate.

Paleoenvironmental data thus represent past conditions in different ways depending on the climatic factors that control the formation of each type of data (Sloan and Barron, 1992). Paleodata are quantitatively interpreted in climatic terms such as temperature or moisture by various methods. It is called an "inverse" approach because the flow of cause and effect (i.e., climatic variations cause responses in paleoclimatic indicators) is conceptually inverted in order to infer from the responses the nature of the causes. These reconstructions can be eventually used by themselves to make inferences about the proximate controls of the climatic variations recorded by the data. Furthermore, the reconstructions can be compared with paleoclimates simulated by a model as the "observations" of paleoclimate (Bartlein et al., 2011).

The quantitative translation of proxy data is traditionally done with multivariate statistical methods, such as the modern analogue technique (a multivariate-distance based approach; e.g., Overpeck et al., 1995; Jackson and Williams, 2004) and the response-surface method (a regression-based approach; e.g., Bartlein et al. 1986; Gonzales et al. 2009). These techniques enable researchers to reconstruct paleoenvironmental conditions based on ecological equations or information that relate data to the present (or modern) conditions, and then applying the equations to paleodata. However, there are several statistical and ecological assumptions that must be satisfied when making climatic inferences from paleoenvironmental data (Guiot et al., 2009). These assumptions are that (1) climate is the ultimate cause of changes in paleoenvironmental data, (2) the ecological properties of the species considered has not changed between the period analyzed and the present time, and the relationship between the species and the climate is uniform through time, and (3) the modern data contain all the necessary information to interpret the paleodata. Furthermore, it should be noted that there is a possibility that indeterminacy of the paleoclimate data exists, even if the technical assumptions are satisfied: the specific controls of a particular paleoclimate record cannot always be uniquely and clearly determined from the data alone (Bartlein et al. 1991; Sloan and Barron 1992). Thus, even

if the paleoclimate conditions are correct, they alone cannot bring out the controls of the past climates. Indeterminacy of proxy data generally arises from two sources; one is intrinsic to the data itself because multiple climatic variables potentially influence a particular biological or geological record, and the other is related to the nature of the climate system. For example, a similar regional paleoclimatic anomaly pattern from present can result from two different sets of ultimate controls, and the reconstructed pattern alone cannot discriminate between two.

One of the significant disadvantages of the inverse-modeling approach is the assumption that the dependence of vegetation on climate is not mediated by changing CO_2 levels or soil development. Because polar ice core records indicates that the atmospheric CO_2 level varies through time and some plant physiological studies (e.g. Farquhar 1997; Jolly and Haxeltine 1997; StreetPerrott et al. 1997) have showed differing responses of vegetation to atmospheric CO_2 levels, the assumption may lead to considerable bias (Cowling and Sykes 1999; Prentice and Harrison 2009). Cowling and Sykes (1999) suggested that pollen-based reconstructions could underestimate temperature decrease and overestimate the dryness under the LGM climate. However, Williams et al. (2000b) disputed Cowling and Sykes' assertion about the temperature responses, and they consider that the assumption would not be violated over the Holocene when CO_2 levels are similar to modern ones.

3.2. Forward-modeling approach

Bartlein (1997) stated that climate variations occur within a hierarchy of controls and responses, which begin at the highest level with the external controls of climate (boundary conditions), through global-to-regional scales, and end with the variations of individual environmental systems (e.g. microclimate) at specific sites (local scales) at the lowest level. Responses at any one level of the hierarchy become the controls of the components at lower level. In this context, the forward-modeling approach is a top-down

approach, and the concept itself can be applied as a workflow. In practice, the approach begins with assumptions regarding the state of the large-scale controls of climate (boundary conditions) and applies the boundary condition to a climate model. The climate model makes simulations/projections of a potential response to this particular configuration of the controls. Then, the simulations/projections from the climate model can be input to subsystem models, such as equilibrium biogeography models and dynamic vegetation models (DGVMs). The subsystem model output (known as simulated paleoclimatic indicators) is then compared with the available paleoclimatic indicators such as pollen data converted into plant functional types (PFTs) or biomes.

The subsystem process-based models, which are based on theoretical understanding of relevant environmental processes, can also provide a practical opportunity for understanding specific responses to changes in environmental conditions. For example, these process-based models can be used to predict the response of paleoenvironmental indicators (e.g. vegetation, hydrology, and dust deposition) to the really different climates from the present a situation in which statistical models might make inappropriate extrapolations.

In forward-modeling approaches, we can state systematic hypotheses about the large-scale controls of climate, and then simulate the responses of different paleoenvironmental indicators (Schmidt, 2010). Furthermore, this approach can be used to discriminate among different climate models, or among different sets of boundary conditions for those models (Otto-Bliesner et al., 2009). In such an application, the sets of paleoenvironmental responses produced by the approach would be compared to syntheses of paleoclimatic data in order to identify which GCM simulation was most consistent with the data (Kohfeld and Harrison, 2000). The forward-modeling approach can also be iteratively applied in order to resolve apparent inconsistencies among different sources of paleoclimatic data (Fig. 1.2).

When using terrestrial biosphere models such as BIOME4 (Kaplan et al., 2003, we can simulate the distribution of major vegetation types (biomes) as a function of climate (temperature, precipitation, and cloudiness, absolute minimum temperature), soil physical properties (water holding capacity and percolation rate), latitude, insolation, and atmospheric CO_2 concentration. The simulated biome distribution can be directly compared with biomes reconstructed from pollen data (e.g. BIOME6000). This forward-modeling approach enables us to simulate various climatic and environmental indicators that depend on the process-based model used. Using dynamic global vegetation models (DGVMs) such as LPJ (Sitch et al., 2003) and LPX (Prentice et al., 2011a, 2011b), we can simulate the regional-to-global scale hydrological cycle (e.g. Gerten et al., 2004; Murray et al 2011), fire regime (e.g. Thonicke et al., 2010; Prentice et al., 2011a), and carbon cycle (Prentice et al., 2011a and 2011b), examine the interaction between vegetation and biogeochemical cycles, and then directly compare the results with data sets such as BIOME6000 and Global Charcoal Database (GCD).

3.3. Inverse modeling through iterative forward modeling

As mentioned above, inverse- and forward-modeling approaches each have both advantages and disadvantages. The advantage of the inverse-modeling approach is that it is based on “observed ” data, as opposed to simulated data. The inverse approaches can be usefully applied in those regions where proxy data are abundant and the assumptions that underlie the approaches used are not violated. In these regions, this approach can provide quantitative reconstructions of past climates with relatively low uncertainties. However, the inverse approach suffers from indeterminacy, constraints of technical assumptions, and problems of applicability in regions of sparse coverage of paleoenvironmental data. In contrast, forward-modeling approaches have the advantages of reducing the indeterminacy problems because of the use of process-based models, and allowing paleoclimatic hypotheses to be tested even in regions of little coverage of

paleoclimatic data. This approach can also be applied over the entire domain of interest (regional to global scale) and generally provides a very high-resolution spatial pattern of paleoenvironmental responses. However, the results strongly depend on the subsystem model used. For these reasons, inverse- and forward-modeling approaches provide complementary approaches for data-model comparisons.

In order to overcome the aforementioned problem with the inverse-modeling approach (the assumption, likely violated, that the response of vegetation to climate is not mediated by atmospheric CO_2 level), Guiot et al. (2000) and Wu et al. (2007) proposed the "inverse vegetation modeling" approach for climate and vegetation reconstruction. Because this approach (i) eliminates the potential CO_2-induced bias from pollen-based climate reconstructions using a process-based 'equilibrium' vegetation model that includes a photosynthesis scheme, (ii) solves no-analog and wrong analog problems, and (iii) provides realistic error bars based on the full range of possible climates that target vegetation exists, the approach provides better spatial and quantitative climate estimates from pollen. The principle of the method is to estimate the input of the vegetation model (i.e. the monthly climate) for which the model output fits as much as possible a set of observations (fossil pollen). In other words, the method attempts to find the particular climate that might have given rise to a particular fossil-pollen spectrum, and does this by iteratively trying a variety of different climate-variable values.

In theory, one could solve the problem of finding the "correct" climate values that gave rise to a particular fossil-pollen spectrum by trying a vast number of different values, but the problem can also be solved with appropriate algorithms in a Bayesian framework. Moreover, the Metropolis-Hasting algorithm in Monte Carlo Markov Chain (MCMC) methods can be used to accelerate the search for the appropriate values of the climate variables being reconstructed. This approach accepts the concept of multi-equilibrium status between environmental conditions (e.g. climate, atmospheric CO_2, and soil) and the vegetation, and provides more directly comparable and robust opportunities

to evaluate climate models than do proxy data-based reconstructions. However, this approach is dependent on the selection of a particular process model and still requires a great deal of computation time.

4. Paleoclimate diagnostics

Apparent disagreement in paleo data-model comparison can arise from the following three sources: (1) misinterpretation of the data that result from inadequate data coverage and insufficient understanding of the climatic significance of the data, (2) inadequacy of the climate model itself, and (3) shortcoming in the experimental design (e.g. incorrect specification of the climate forcing). Attempts to deal with the above problems have led to (1) the improvement of the data sets for data-model comparisons (i.e. data syntheses and benchmarking data sets), the development of objective techniques for reconstructing climate variables from the data (e.g., iterative forward-modeling approach), and the increasing use of models in order to simulate the response of environmental sensors to climate change, (2) the improvement of the climate model, and (3) elaboration of experimental designs (Braconnot et al., 2012). Data-model comparison is an iterative cycle/processes (i.e., from the observation of a mismatch between simulations and observations, we start to improve the data and models, and then compare new data and new models), and has led to an increase in our scientific understanding about the Earth system. We can refer to a series of paleo data-model comparisons as *paleoclimate diagnostics* because data syntheses and model simulations can be viewed as complementary tools that can be used to understand past climatic variations/changes, in the same way that (modern) "climate diagnostics" use combinations of observations and experiments using climate models to understand the generation of present-day interannual and decadal climate variations.

Beyond the understanding of past climate changes/variations, paleoclimate diagnostics make an attempt to explore a connection to future climate projections because

(ideally) model configurations will be exactly the same in the paleo and future simulations in CMIP5. In practice, we search for the properties/correlations and robust patterns in climate simulations that we expect to be features of all climate states, and use the paleoenvironmental data to provide some independent evidence for that relationship. Izumi et al. (2013, see Chapter II) investigated (a) enhanced land-ocean contrast, (b) the stronger response at higher latitudes than in the tropics, and (c) differential responses in warm- and cool-season climates in *lgm*, *midHolocene*, *historical*, *1pctCO$_2$*, and *abrupt4×CO$_2$* CMIP5 simulations, and found broadly consistent relationships across the climate states. Similarly, Li et al. (2013) investigated precipitation scaling with temperature in *lgm*, *historical*, *1pctCO$_2$*, and *abrupt4×CO$_2$* CMIP5 simulations, and found consistent patterns in the nature of the scaling of large-scale precipitation changes with temperature in warm and cold climates. Similar patterns also appear in both historical observations paleoclimatic reconstructions, implying that such responses are characteristic features of the climate system.

We also need to understand the physical processes that explain such connections between past and future climate states in order to support our interpretation of the relationships involved. Schmidt et al. (2014) also showed that the skill measures might be used to validate the robust patterns of climate changes between different climate states. Izumi et al. (2014, see Chapter III) examined the possibility that a small set of common mechanisms controls the large-scale responses described Izumi et al (2013) using a simple energy-balance model to decompose the temperature changes shown in multiple *lgm* and *abrupt4×CO$_2$* CMIP5 simulations. Izumi et al. (2014) thus demonstrate the way in which paleoclimate simulations are useful adjuncts to analyses of modern-day climates in understanding the fundamental mechanisms of climate changes. Izumi et al. (in prep) investigate further large-scale temperature responses in terms of atmospheric circulation and the hydrological cycle, because a key control of the robust responses is clear-sky

longwave downward radiation that is closely related to near-surface air temperature and water vapor in the lower atmosphere.

5. Research questions and dissertation organization

The coordinated PMIP3/CMIP5 paleoclimate modeling experiments, which are performed with the same models as the projections of future climate change, enable us to quantify the link between past and future climate changes. This dissertation explores the consistent climate changes between past and future and their mechanisms. The dissertation also shows the example of North American paleoclimate reconstruction with an inverse-modeling through iterative forward-modeling approach.

The research presented here was guided by the following questions:

1) How does paleo data-model comparison contribute to the projections of future climate?
2) Do paleoclimate simulations have a connection to future projections?
3) Are the consistent climate responses (between models and between data and model in both warm and cold climates) simple model artifacts or real climate features?
4) What are the key controls of the consistent climate responses?
5) How does new vegetation model influence the reconstructed paleoclimates by forward-modeling approach?

This thesis has two parts that each involve the development and application of approaches for paleo data-model comparison: In part 1, I compare modern and paleoenvironmental data syntheses with simulations performed as part of CMIP5, and discuss the consistent simulation of large-scale temperature responses (paper 1, Chapter II), as well as the specific climatic mechanisms behind those responses in both warm and cold climates (paper 2, Chapter III). In part 2, I apply a new equilibrium terrestrial biosphere model, BIOME5 (developed from/based on BIOME4), for reconstructing

North American paleoclimatic variations at the Last Glacial Maximum and mid Holocene using iterative forward-modeling (i.e., Inverse vegetation modeling) approach (paper 3, Chapter IV).

Chapter II: Consistent Large-scale Temperature Responses in Warm and Cold Climate

This chapter was published in *Geophysical Research Letters* (Izumi et al., 2013) as a co-authored article with P.J. Bartlein and S.P. Harrison. The data analysis was performed either by me or by P.J. Bartlein under my direction, and I wrote the initial draft. P.J. Bartlein and S.P. Harrison were involved in discussion of the results, and in the editing of the final paper.

Chapter III: Energy-balance Mechanisms Underlying Consistent Large-scale Temperature Responses in Warm and Cold Climates

This chapter was published in *Climate Dynamics* (Izumi et al., 2014) as a co-authored article with P.J. Bartlein and S.P. Harrison. I conceived of the overall analysis and wrote the initial draft of the paper. P.J. Bartlein and S.P. Harrison were involved in discussions of the results, and in the editing of the final paper.

Chapter IV: The iterative forward-modeling approach for paleoclimatic reconstruction: Climate changes over North America at the mid-Holocene and Last Glacial Maximum

This chapter is in preparation for submission to *Climate of the Past* as a co-authored article with P.J. Bartlein. I conceived of the overall experiments and analyses with Fortran and R, and wrote the initial draft of the paper. P.J. Bartlein made the modern climate data used in the analysis and a Fortran program for making gridded data, and was involved in discussion of the results, and in design and drafting of the final paper.

CHAPTER II

CONSISTENT LARGE-SCALE TEMPERATURE RESPONSES IN WARM AND COLD CLIMATE

This chapter has been published as a co-authored manuscript in the journal *Geophysical Research Letters* (Izumi et al. 2013.)

1. Introduction

Climate-model simulations typically show large-scale patterns or gradients in temperature anomalies (differences between a past or future experiment and a control experiment) rather than spatially uniform patterns of change. In particular, simulations show stronger temperature responses over land than over the oceans (Sutton et al. 2007; Joshi et al. 2008; Boer 2011), stronger responses in higher latitudes than in lower latitudes (Masson-Delmotte et al. 2006; Hargreaves et al. 2007; Serreze and Barry 2011; Dowsett et al. 2012b), and differences in the response between winter and summer that result in changes in the seasonal temperature contrast (Stine et al. 2009; Dwyer et al. 2012b). A variety of mechanisms have been invoked to explain these responses, but no comprehensive explanation has yet emerged. The consistency of these simulated anomaly patterns across a range of climate states and individual climate models invites the question of whether their source is the common underlying structure of climate models or whether they arise from mechanisms that also operate in the real climate system: a question which can be addressed by comparing the simulated changes with observations (for the historical period) or paleoclimate reconstructions (for paleoclimates).

The ratios of land to ocean, high to low latitude, or summer to winter warming or cooling (changing seasonality) in an individual simulation provide some simple indices

that describe these emergent properties of the climate system. Such ratios have been calculated using multiple-model realizations of the same climate change (e.g. (Holland and Bitz 2003; Sutton et al. 2007; Dwyer et al. 2012b)), or with a single model for different climate states (Hargreaves et al. 2007) but it is difficult to calculate a robust measure of the proportionality of the response based on a limited range of climate states or models. Here we exploit the fact that six modeling groups have simulated both warm and cold climates with the same model as part of the Coupled Modelling Intercomparison Project (CMIP5; (Taylor et al. 2012)). These simulations allow us to examine the large-scale anomaly patterns of temperature, and the associated ratios or proportionalities in the magnitude of the responses in a systematic fashion across a range of climate states. Comparison with the large-scale temperature changes shown by historical observations and by paleoclimate reconstructions allows us to determine the realism of these responses.

2. Data and methods

We have examined temperature responses in five CMIP5 experiments: *lgm*, *midHolocene*, *historical*, *1pctCO$_2$*, and *abrupt4xCO$_2$*, expressed as anomalies relative to a pre-industrial control simulation (*piControl*) (for details see (Taylor et al. 2012); (Braconnot et al. 2012)). The *lgm* and *midHolocene* experiments represent iconic periods in the paleorecord, well-documented by paleoenvironmental evidence (Braconnot et al. 2012). The *lgm* experiment (Last Glacial Maximum, ca 21,000 years ago) shows the response to large Northern Hemisphere (NH) ice sheets and low greenhouse gas (GHG) concentrations. The *midHolocene* experiment shows the response to changes in the seasonal and latitudinal distribution in insolation 6000 years ago (with GHG concentrations at pre-industrial levels). The *historical* simulation (1850 to 2005 CE) is forced by time-varying changes in solar, volcanic, and GHG forcing. The *1pctCO$_2$* experiment shows the response to a gradual increase in CO_2 concentration, while the

abrupt4xCO₂ experiment examines the response to an abrupt increase in CO_2 to 1120 ppm. The *abrupt4xCO₂* experiment is opposite (but of comparable magnitude) to the *lgm* in terms of absolute difference in GHG forcing. Details of the forcings used for each experiment are given in (Taylor et al. 2012) and (Braconnot et al. 2012). The trends in temperature across the five experiments (Figure 2.1) are broadly consistent with the GHG forcing, and as expected the *abrupt4xCO₂* and *lgm* temperature changes are of similar magnitude.

Six models (IPSL-CM5A-LR, MPI-ESM-P, MIROC-ESM, CCSM4, MRI-CGCM3, GISS-E2-R) had archived outputs from these six simulations as of 15th August 2012. We use *tas* over the land (where land area fraction, *sftlf* is more than 40%). We use *tos* over the ocean, except where *sic* ≥ 40% where we use *tas*. We used the last 100 yrs of the *lgm*, *mid-Holocene*, and *piControl* simulations, the last 60 yrs of the *abrupt4xCO₂* simulation, and the interval from 1979 to 2005CE in the *historical* simulation. For the *1pctCO₂* simulation, we used a 30 yr interval (model years 86-115), which has an average concentration of CO_2 of 750 ppm (i.e. midway between early 20th century and 4x pre-industrial values) to represent an intermediate CO_2-induced climate change.

For mapping and the calculation of ensemble averages (Figure 2.1), the model output was interpolated to a regular 2.0° grid using bilinear interpolation for atmosphere-model output and nearest-neighbor interpolation for ocean-model output; otherwise the averages are calculated on the native grid of each model. All averages (Figure 2.2) were areally weighted (by the area of the model or ensemble grid cells). Relationships between the climate variables across the different simulations and models were explored using reduced major axis (RMA) regression (McArdle 1988), testing the null hypothesis that the RMA slope is equal to 1.0.

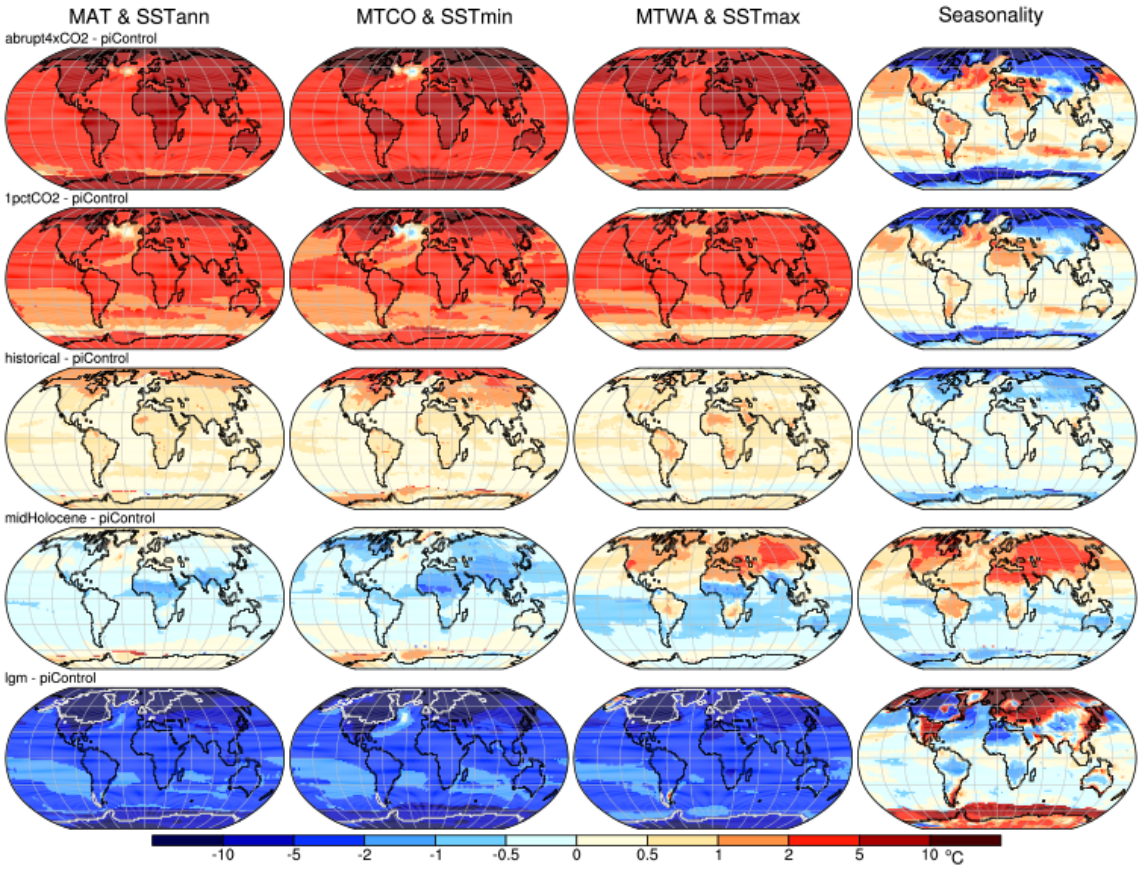

Figure 2.1. Simulated temperature changes in past, present and projected climates. The values shown are ensemble averages of the outputs from the six CMIP5 models. The plots show the anomalies (experiment minus *piControl*) of mean annual temperature (MAT), mean temperature of the coldest month (MTCO), mean temperature of the warmest month (MTWA), and the change in temperature seasonality (ΔMTWA-ΔMTCO).

We used instrumental data and paleoclimatic reconstructions to represent "observed" climates. For comparison with the *historical* simulation anomalies we used the HadCRUT3v combined land and ocean temperature data set (Brohan et al. 2006). There is a tradeoff between spatial and temporal coverage in this gridded data set; we

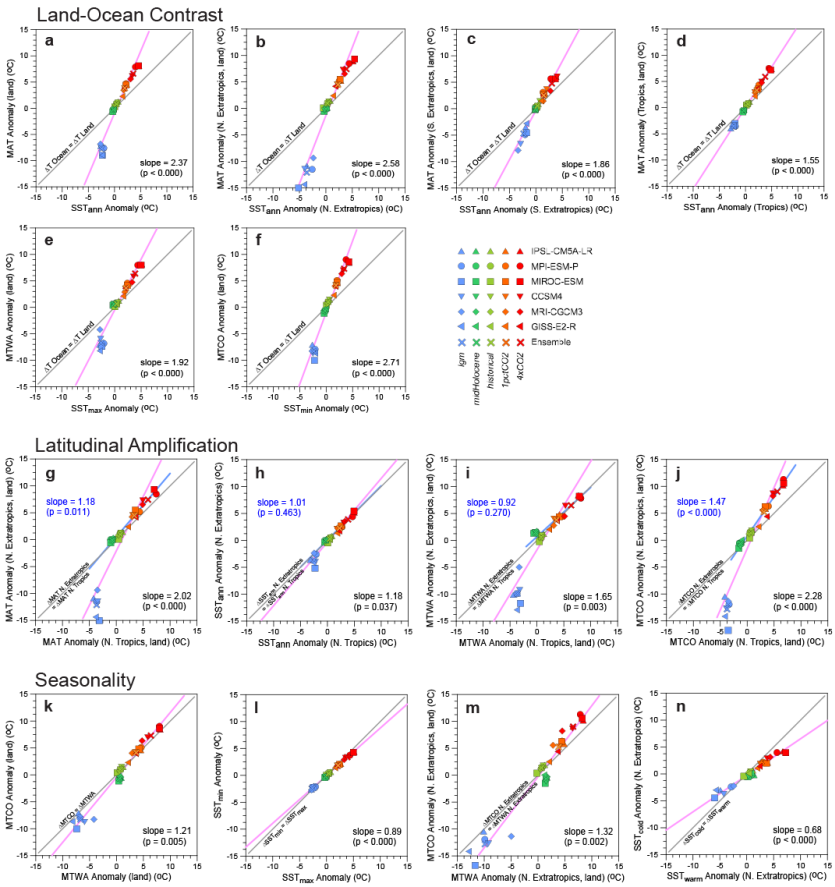

Figure 2.2. Scatter plots showing simulated area-averaged temperature changes in past, present and projected climates. The values shown are the simulated change in temperature (experiment minus *piControl*) for each of the six models. Differences in the relative warming over land and ocean (land-ocean contrast) are shown for (a) the globe, (b) the northern extratropics (30-85°N), (c) the southern extratropics (65-30°S) and (d) the tropics (30°S-30°N). Differences in the relative warming over land and ocean are also shown for the globe for (e) the warm season and (f) the cold season. Differences in the relative warming in the northern extratropics and northern tropics (latitudinal amplification) are shown for (g) land areas and (h) ocean areas separately, and for (i) the warm season and (j) the cool season. Changes in seasonality are shown for (k) land areas and (l) ocean areas separately, and for (m) the land and (n) the ocean for the northern extratropics. The diagonal gray lines are 1:1 lines, while the magenta lines are the RMA regression lines, and the p-values shown are those for a test of the null hypothesis that the slopes of the RMA regression lines are equal to 1.0. On panels (g) to (j), an additional RMA regression line fit without using data from the *lgm* simulation, and the appropriate statistics, are shown in blue.

adopted the difference between the 1941-1970 and 1979-2005 long-term means to represent recent observed climate change. The data set provides temperatures for 600 non-ice-covered 5-degree land and 1461 ocean grid cells, representing 87% of the total surface of the globe (see Figure S2.5). For the mid-Holocene and LGM, we used a synthesis of data from existing compilations (MARGO Project Members 2009; Leduc et al. 2010; Bartlein et al. 2011; Schmittner et al. 2011). For the LGM ocean (MARGO Project Members 2009), the reconstructions of seasonal SSTs are expressed variously in terms of summer, winter, warm and cold season, and we refer to these generically as SSTwarm and SSTcold. The mid-Holocene and LGM reconstructions were all expressed as anomalies. There are 704 non-ice-covered land and 64 ocean data points for the MH, and 153 land and 577 ocean data points for the LGM, representing 5 and 6% of the total surface of the globe respectively (see Figure S2.5). We compared the simulations and observations by comparing map patterns (Figure S2.5) and examining scatter plots of large-scale averages model output at the locations of the observations (Figure 2.3).

There are several sources of uncertainty in the paleoclimate data sets. Some types of uncertainty, such as those associated with age modeling, context and taphonomy, and the reliability of different reconstruction methods and/or calibrations, are particular to the paleo-reconstructions. Such uncertainties could be taken into account using expert assessment (see e.g. (Dowsett et al. 2012b)). An alternative approach, used here, involves pre-screening the data set to exclude sites with poor chronologies and to remove records from atypical environments (Bartlein et al. 2011). We propagate the uncertainties associated with the reconstructions (i.e. prediction error variances) and from the use of different methodologies (structural uncertainties) into the area averages using a Monte Carlo approach (see below, and Supplemental Information).

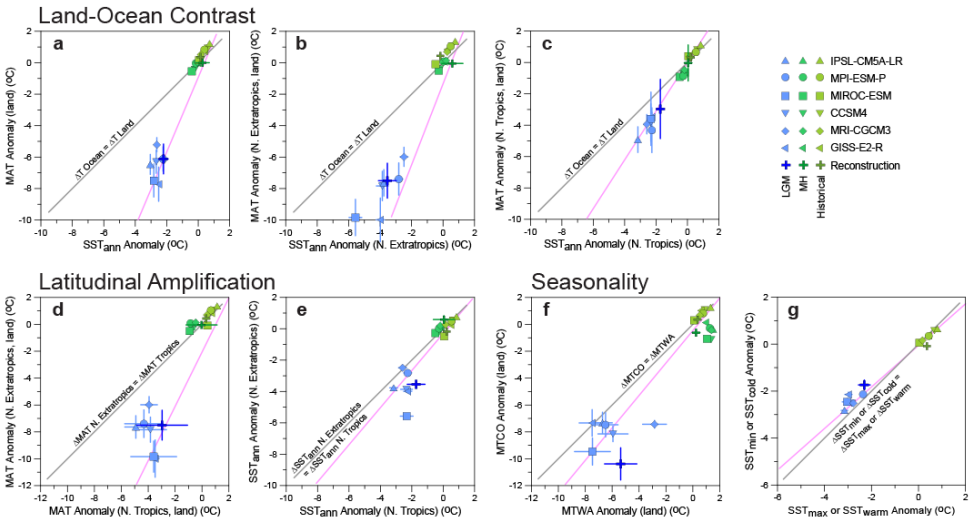

Figure 2.3. Comparison of simulated and observed area-averaged temperature changes for the 20th century (historical), mid-Holocene (MH) and Last Glacial Maximum (LGM), where the model output has been sampled only at the locations of the 20th century observations or palaeoclimate reconstructions. Area-weighted averages of 20th century observations and area-weighted averages of paleoclimate reconstructions are shown by bold crosses, and uncertainties associated with the reconstructions are shown by the finer lines. Differences in the relative warming over land and ocean (land-ocean contrast) are shown for (a) the globe, (b) the northern extratropics, and (c) the northern tropics. Differences in the relative warming in the northern extratropics and northern tropics (latitudinal amplification) are shown for (d) land areas and (e) ocean areas separately. Changes in seasonality as shown for (f) land areas and (g) ocean areas separately. The diagonal gray lines are 1:1 lines; the magenta lines are the RMA regression lines for the simulations from Figure 2.2 (i.e. derived using all appropriate model grid cells, as opposed to only those locations with paleoclimate reconstructions). Deviations between the RMA line and the observed/simulated changes as shown by the symbols provide a measure of the degree to which the comparison at the location of the observations might provide a biased representation of simulated changes.

The error bars for each model point on Figure 2.3 are bootstrap estimates (1000 replications) of the standard error of the spatial means of model output at the locations of the paleodata. For each replication the model values are sampled with replacement, and the area-weighted mean is calculated. The variability among these 1000 values is thus related to the particular sample of points selected at each iteration. The plotted error bars

are 2x the standard deviation of the 1000 bootstrap replicates of the weighted means and provide a measure of the uncertainty of the model output related to the particular distribution of the observations.

For the observations/reconstructions, the error bars include both reconstruction uncertainties and bootstrap estimates of the standard error of the spatial means. The reconstruction uncertainties are calculated as follows: for any one weighted mean (either the overall one, or one of the bootstrap iterations), the reconstruction uncertainties are included by generating a random number from the (standard) normal distribution for each reconstructed value, and then rescaling that value using the standard error of the reconstruction. We use this procedure to generate 1000 replicate estimates of each reconstructed value. The bootstrap standard error of the data thus includes the overall spatial variability, the variability due to the particular sample of points included in the mean, and the reconstruction uncertainty of those points.

3. Results

3.1. Simulated temperature responses

All of the experiments show a differential response of the land and ocean to the changes in forcing (Figure 2.1, Figures S2.1-2.3). The land response is larger than the ocean response for year-round warming in the two future experiments and the summer (MTWA) in the *midHolocene* and for year-round cooling in the *lgm* experiment and the winter (MTCO) in the *midHolocene* experiment. We estimate the land-ocean warming ratio using reduced major axis (RMA) regression, where the slope coefficient provides an estimate of this ratio across all models and all climates, and whether this is significantly different from a 1 to 1 relationship. The RMA regression estimate of the relationship between annual temperature (MAT) anomalies over land and the annual SST anomalies across the suite of simulations and models (Figure 2.2a, Table S2.1) is 2.37 (Table S2.2). The contrast between the land and ocean warming or cooling is greater in the extratropics

(2.58 in NH, Figure 2.2b; 1.86 in the southern hemisphere (SH), Figure 2.2c) than in the tropics (1.55, Figure 2.2c), and more pronounced in winter (2.71, Figure 2.2f) than summer (1.92, Figure 2.2e). Estimates calculated for individual experiments and models (Table S2.3) show that the ratio for future simulations is close to 2 (1.53-2.16 in the *1pctCO$_2$*, and 1.73-2.06 in the *abrupt4xCO$_2$*), similar to the results found in CMIP3 elevated-CO_2 experiments (Meehl et al. 2007; Sutton et al. 2007). The land-sea temperature ratio in the CMIP5 *lgm* experiments is larger (2.54 to 3.88) than in the future simulations; this contradicts the finding (based on results from a single model) that LGM and modern ratios are the same (Laine et al. 2009). However, in common with previous analyses (Sutton et al. 2007; Boer 2011), the ratio varies with latitude and is smaller in the tropics.

The experiments also show a stronger temperature response at higher than at lower latitudes (Figure 2.1, Figures S2.1-2.3). In globally warmer climates (including MH summer), the high latitudes warm more than the tropics while in globally colder climates (including MH winter) they cool more than the tropics. We focus on the relationship between extratropical and tropical temperatures because "polar" or "Arctic" amplification (i.e. the ratio of warming/cooling in polar regions, generally poleward of ca 75° N/S, relative to the hemispheric or global average), is difficult to evaluate because there are few observations from the highest latitudes (Miller et al. 2010) and ice-core estimates of temperature changes have potentially large biases associated with the changes in ice-sheet elevation and temperature changes in the oceanic moisture-source areas (Masson-Delmotte et al. 2006; Braconnot et al. 2012). The enhancement of the temperature response between the NH extra-tropics and tropics is seen in all temperature variables (Figures 2.2g-j, Table S2.2), but it is smaller over the oceans (1.18, Figure 2.2h) than over the land (2.02, Figure 2.2g) and more pronounced in winter (2.28, Figure 2.2j) than in summer (1.65, Figure 2.2i). Stronger temperature responses in the Arctic are characteristic of future-climate simulations (Holland and Bitz 2003; Lu and Cai 2009;

Winton 2006). There is less consistency in model predictions of enhanced future warming in the Antarctic (Meehl et al. 2007), although Antarctic amplification is a feature of paleoclimate simulations (Masson-Delmotte et al. 2006; Braconnot et al. 2012). (Holland and Bitz 2003) estimated an Arctic/global warming ratio between 1.5 and 4.5 from the CMIP2 simulations and (Holland and Bitz 2003; Lu and Cai 2009; Winton 2006) found an average of 1.9 in the CMIP3 simulations at the time of carbon dioxide doubling. The greater sensitivity of NH high latitudes in winter has been previously noted as a feature of CMIP3 simulations (Lu and Cai 2009). The *lgm* simulations show the greatest departure from a linear response of latitudinal amplification across the different climates (Figure 2.3g-j), related to the presence of large ice sheets in the simulations. The overall sign of the relationship between NH high- and low-latitude responses remains unaltered if the RMA regressions are refit without the *lgm* simulations.

All of the experiments also show changes in temperature seasonality (Figure 2.1, Figure S2.4). In the *midHolocene* experiment, this response is ultimately a consequence of the insolation forcing, although reinforced by ocean and land-surface feedbacks (Braconnot et al. 2007). However, seasonality changes in experiments with uniform year-round forcing reflects differential sensitivities of warm and cold season climates to changes in the forcing. As might be expected, given the larger temperature responses over land than over the ocean, the change in seasonality is most marked over the continents (Figure 2.2k). Over land, seasonality is enhanced in year-round cold climates and reduced in year-round warm climates. The reverse is true over the ocean, where seasonality is reduced in cold climates (except in MPI-ESM-P: Table S2.3) and enhanced in warm climates. These changes are only characteristic of the extratropical regions because most of the tropics are dominated by non-seasonal climates. The changes in seasonality are most pronounced in the NH extratropics (Figure 2.2m), reflecting the predominance of ocean in the SH. Enhanced seasonality in land temperatures was a

feature of the CMIP3 future-climate simulations (Dwyer et al. 2012b) and is shown here to be a generic response to year-round changes in forcing.

Overall, the individual responses are proportional and close to linear across the differing climate states (Figure 2.2). The greatest deviation from a general linear response exists for NH land areas in the *lgm* experiment, where the ice sheets amplify the general cooling.

3.2. Data-model comparison

Comparison of the differences in long-term means for the intervals 1941 to 1970 and 1979 to 2005 shows that the basic features of the *historical*, *abrupt4xCO2* and *1pctCO2* simulations are apparent in the observational record (Figure S2.5). Temperature differences are small but positive over most land areas and are larger at high northern latitudes than in the tropics. The anomalies are consistent with increasing contrast between land and ocean, and with greater warming over mid-to-high northern latitudes. Over the northern continents MTCO has increased more than MTWA, and also has increased more than over the oceans. The anomaly pattern of MTWA-MTCO likewise shows reduced seasonality over the northern continents and enhanced seasonality over the ocean, as in the simulations.

MH and LGM reconstructions (Braconnot et al. 2012) also support the realism of the simulated regional climates (Figure S2.5). Temperature changes at the LGM and in the MH are large, compared to the uncertainty in the reconstructions, and thus both periods provide extremely good targets for model evaluation. At the LGM, the reconstructed annual cooling is about three times larger over land than ocean. Land-ocean contrast is stronger in high latitudes than in the tropics, and extratropical cooling is stronger in winter than summer. Seasonal contrast is enhanced over land, but reduced over the oceans. Amplification of land-ocean contrast and high-latitude temperatures is also apparent during the MH, but this is partly a predictable consequence of the changes

in insolation forcing (Braconnot et al. 2007). Seasonal contrast is reduced over the continents in summer and enhanced in winter. The global data set does not contain ocean data that can discriminate MH seasonality changes over the ocean.

The similarity of the simulated and observed climate can be further assessed using scatter plots of area-averaged temperature changes at the locations where there are 20th century observations or paleoclimate reconstructions (Figure 2.3). The coverage of observations is uneven, but the averages (for both data points and models-at-data points) generally fall on the global regression line estimated using all points in the simulations (see Figure 2.2) showing they provide a reasonable sampling of each climate state. The simulated land-ocean warming ratio (Figure 2.3a-c) is consistent with observations, as is the simulated latitudinal amplification over land (Figure 2.3d) and ocean (Figure 2.3e). The largest discrepancies occur at the LGM where simulated tropical temperatures are slightly colder than reconstructed (Figure 2.3c) particularly over the oceans (Figure 2.3e). The simulated changes in seasonal contrast are qualitatively consistent with observed changes (Figure 2.3f, 2.3g), although the models tend to produce a more uniform change in seasonal temperatures at the LGM and more seasonal contrast during the MH and 20th century. The spread of model estimates of all of the ratios for each time period is generally larger than the differences between any one model and the observations. Models show consistent behaviour in this respect: for example, MIROC-ESM and GISS-E2-R show larger changes in temperature while MRI-CGCM shows smaller temperature changes than observed. The fact that differences between the models are larger than the differences between any individual model and the observations is consistent with the idea that the mean model is usually closer to observations than most individual climate models [see e.g. Gleckler et al., 2008], and provides support for the continued use of multi-model ensembles for paleoclimate analyses and future projections.

4. Conclusion

The consistency among simulated and observed large-scale temperature responses in the past shows that these are features of the real climate system that are simulated successfully by models rather than artifacts arising from similarities in model construction. The causes of this spatial differentiation are inherent in the energetics and dynamics of the climate system, but several different feedbacks are also potentially involved (Joshi et al. 2008; Fasullo 2010; Solomon 2006; Serreze and Barry 2011; Screen and Simmonds 2010b; Dwyer et al. 2012b), and their mechanisms are still matters of debate. However, the consistency in the simulated patterns of past and future temperature changes implies that a small set of common mechanisms governs the response of the climate system across multiple states. The challenge now is to provide a consistent and mechanistic explanation of how these temperature responses arise in both warmer and colder climates. Such explanations will further increase our confidence in the ability of climate models to correctly explain past and project future climatic changes.

5. Chapter II bridge paragraph

In chapter II, I found the large-scale temperature responses (land-ocean contrast, high-latitude amplification, and seasonality changes) in CMIP5 *lgm*, *hidHolocene*, *historical*, *1pctCO$_2$*, and *abrupt4xCO$_2$* experiments, expressed as anomalies relative to the piControl simulation, and these are consistent (with proportional and nearly linear responses) across multiple climates states. In chapter III, we adopted a simple surface energy-balance model in order to examine the possibility that a small set of common mechanisms control these large-scale responses of the climate system across multiple states.

CHAPTER III

ENERGY-BALANCE MECHANISMS UNDERLYING CONSISTENT LARGE-SCALE TEMPERATURE RESPONSES IN WARM AND COLD CLIMATES

This chapter has been published as a co-authored manuscript in the journal *Climate Dynamics* (Izumi et al. 2014.)

1. Introduction

There are a number of common large-scale temperature responses to changes in forcing in simulations of past, historical, and future climates (Izumi et al. 2013), including 1) the differential responses of land and ocean to global warming or cooling, i.e. changes in the land-ocean contrast, 2) the tendency for temperature changes in the higher latitudes to be more extreme than changes in the tropics, i.e. high-latitude amplification, and 3) changes in seasonality in response to year-round changes in forcing. These responses are also shown in historical and paleoclimatic data. The consistency among simulated and observed temperature responses in the past (Izumi et al. 2013) implies that these are features of the climate system that are simulated successfully. The consistency of the simulated patterns of past and future temperature changes implies that a small set of common mechanisms controls the response of the climate system across multiple states. Previous studies have suggested that the consistency of the responses is inherent in the energetics and dynamics of the climate system (e.g. Dwyer et al. 2012a; Fasullo 2010; Joshi et al. 2008; Screen and Simmonds 2010b). However, several different feedbacks are also potentially involved and the specific mechanisms are still matters of debate.

Here we review some of the previous studies that have focused on one or more of these large-scale responses in either warm or cold climates (or a few in both). We then

attempt to diagnose the controls of these responses using an energy-balance approach to decompose the temperature changes shown in multiple simulations from the CMIP5 archive for both cold (*lgm*) and warm (*abrupt4×CO_2*) climates. We use a "bottom-up" approach that focuses first on map patterns of the components of temperature change, followed by an examination of zonal- and large-scale area-averages.

Land-ocean surface-temperature contrast, the generally larger amplitude of changes in land-surface temperature relative to those of the surrounding oceans, has been noted in both CO_2-induced warmer climate simulations (e.g. Sutton et al. 2007; Joshi et al. 2008) and CO_2-induced or decreased SST cooler climate simulations (e.g. Laine et al. 2009; Manabe et al. 1991; Joshi et al. 2008). The response is seen in both transient and equilibrium simulations, and thus the large heat capacity of ocean cannot be the primary reason for generation of the temperature contrast (Sutton et al. 2007). Several alternative mechanisms have been suggested to explain land-ocean contrast. First, Sutton et al. (2007), Laine et al. (2009), and Dong et al. (2009) suggested that the partitioning of the surface energy budget explains the contrast in the CO_2-induced warm or cold climates through changes in latent heat flux, cloud cover, or downward shortwave radiation. An increase in net downward radiation is compensated by an increase in latent heat flux over the oceans, but sensible heat flux increases over the land as the land dries out (Sutton et al. 2007). Drying of the land leads to reduction of cloud cover and increased downward shortwave radiation (Dong et al. 2009). Second, Joshi et al. (2008) and Byrne and O'Gorman (2013a) proposed that the difference between the moist- and dry-adiabatic lapse rates, and greater aridity over the land than ocean, leads to lower-tropospheric and surface-temperature increases over land when global temperatures increase; this hypothesis is based on the observation that temperature anomalies in the mid- and upper troposphere are zonally quite uniform because of efficient atmospheric transport, and is consistent with weak temperature-gradient hypothesis of Sobel and Bretherton (2000). Because the moisture source for the boundary layer over the land originates primarily

from the oceans, an increase in boundary-layer moisture is constrained by the increase in specific humidity over the ocean, and by the Clausius-Clapeyron relation, and will thus fail to keep pace with saturation specific humidity over the land (Joshi et al. 2008). Land evaporation initially increases to compensate, but the land surface quickly begins to dry out, leading to further land warming. Third, Compo and Sardeshmukh (2009) showed that land warming is a response to ocean warming via "hydrodynamic-radiative teleconections" such that moister and warmer air over the land results in increased longwave downward radiation at the surface.

Polar amplification is generally defined as trends (and variability) in near-surface air temperature that are larger in the Arctic/Antarctic regions than for the northern/southern hemisphere or globe as a whole (Serreze and Barry 2011; Taylor et al. 2013). This response is a near-universal feature of climate-model simulations under greenhouse gas-induced climate changes (e.g. Manabe and Stouffer 1980; Holland and Bitz 2003; Winton 2006), and is also seen in palaeoclimate simulations (e.g. Masson-Delmotte et al. 2006; Brady et al. 2013; Kageyama et al. 2013). Again, several different mechanisms have been proposed. Surface albedo feedback (*SAF*) has been shown to play a significant role in generating the amplification over the Arctic regions, where warming leads to a decrease in surface albedo through reduced ice and snow coverage, which in turn promotes further warming (and the reverse for cooling) (Hall 2004). Longwave (*LW*) radiation feedback from changes in cloud, water vapor, atmospheric CO_2 concentration, and air temperature has also been put forward as a mechanism to explain high-latitude amplification (see e.g. Lu and Cai 2009; Winton 2006; Graversen and Wang 2009; Pithan and Mauritsen 2014). Indeed, some model simulations without *SAF* have been shown to produce amplification through changes in *LW* radiation (Alexeev et al. 2005; Langen and Alexeev 2007; Lu and Cai 2010). Solomon (2006) showed that the increased availability of atmospheric moisture in a warmer climate will also cause enhanced warming of the Arctic regions through promoting stronger cyclones, leading to an increase in poleward

heat transport (see also Graversen et al. 2008). Several authors (Holland et al. 2008; Deser et al. 2010; Jackson et al. 2010; Screen and Simmonds 2010b) have noted that a large part of the fall and winter temperature amplification is linked to sea-ice loss. Warming leads to thinner ice, which is subject to faster melt and increased heat flux through the ice, resulting in less continuous ice cover and a corresponding change of surface albedo and heat release from the ocean. Heat accumulated by the ocean as a result of the ice-albedo feedback mechanism is partially expended in making ice thinner, thus leading to an increase of surface temperatures in fall and winter. Serreze et al. (2009) and Screen and Simmonds (2010a) showed that the Arctic warming is strongest at the surface during most of the year and is primarily consistent with reductions in sea-ice cover. Finally, in some climate model analyses, a positive wintertime feedback between convective clouds and sea-ice loss result in further warming and further sea-ice loss in CO_2-induced climate changes (Abbot et al. 2009; Leibowicz et al. 2012).

Seasonality, or the amplitude of the seasonal cycle of near-surface air temperature over the land has decreased in the last 50 years (e.g. Thomson 1995; Wallace and Osborn 2002; Stine et al. 2009; Stine and Huybers 2012). Climate models project a reduction in the amplitude of the seasonal cycle of near-surface air temperature over high-latitude regions due to late fall and early winter warming under greenhouse gas-induced warmer climates (e.g. Manabe and Stouffer 1980; Mann and Park 1996; Biasutti and Sobel 2009; Dwyer et al. 2012a), and an increase in the amplitude of the seasonal cycle at the LGM (Izumi et al. 2013). Again several mechanisms have been put forward to explain these changes. First, sea-ice loss results in an increase of near-surface air temperature in late fall and winter over high-latitude regions due to an increase in heat release from the ocean (Manabe and Stouffer 1980; Manabe et al. 1992; Mann and Park 1996; Dwyer et al. 2012). Second, the changes over the tropics and mid-latitudes are controlled by changes in surface heat fluxes (Dwyer et al. 2012a), and the easterly trade winds may influence the low-latitude changes in fluxes (Sobel and Camargo 2011). Third, Stine and

Huybers (2012) show a strong relationship between interannual variations in the seasonal cycle and atmospheric circulation, in particular the winter circulation. Finally, it has been suggested that changes in shortwave optical properties can reduce the summertime maximum temperature due to a direct aerosol cooling effect (Wallace and Osborn 2002; Stine et al. 2009).

Thus previous studies have proposed number of different mechanisms for each large-scale temperature pattern in warm or cold climate, but not provided a comprehensive explanation for changes across both warm and climates or among the three large-scale responses. We exploit the fact that many of the models in the Coupled Modelling Intercomparison Project Phase 5 (CMIP5; Taylor et al. 2012) have made simulations of both past and future climates, to explore the key common controls of the large-scale temperature responses in both warmer and cooler climates. We first describe the data sources and processing (Section 2) and the energy-balance model we use to examine the generation of the large-scale responses (Section 3). We then decompose the large-scale responses using the energy-balance model and examine the global spatial patterns and zonal averages of surface temperature and its components (Section 4). We then summarize those large-scale patterns by describing large-scale area averages in warmer and cooler climates (Section 5). Finally, we discuss and summarize our findings (Section 6).

2. Data and analysis

We use global monthly mean surface temperature, surface radiative fluxes for both clear- and total-sky conditions, and surface latent- and sensible-heat fluxes from several Coupled Model Intercomparison Project Phase 5 (CMIP5) experiments, focusing on the *lgm,* and *abrupt4×CO_2*, experiments, expressed as anomalies relative to a pre-industrial control simulation (*piControl*). Details of the experimental design are given by (Taylor et al. 2012; Braconnot et al. 2012). The *lgm* experiment is an equilibrium

simulation of the Last Glacial Maximum (LGM, ca 21,000 years ago) and was designed to examine the climate response to the presence of large ice sheets and lower greenhouse gas (GHG) concentration. The *abrupt4×CO_2* experiment was designed to examine the response to an instantaneous quadrupling of atmospheric CO_2 concentration (relative to *piControl*, i.e., 1120 ppm). Owing to the logarithmic relationship of global average temperature to CO_2 levels, the two simulations are comparable in terms of the difference in CO_2 forcing relative to that for pre-industrial conditions.

We examined anomalies of each of the temperature and energy-balance variables from six models (Table 3.1). These are the six models that have all necessary data (surface temperature, surface and TOA raditative fluxes in both all-sky and clear-sky condition, surface non-radiative flux, sea ice fraction, land ice fraction, and land-ocean mask) for basic analyses. We used the last 100 years of *lgm* and *piControl* simulations and the last 60 years of the *abrupt×CO_2* simulation. The sign, magnitude and spatial patterns of the anomalies are broadly consistent from model to model across multiple climate states (see Fig. S3.1). We therefore calculated the ensemble-mean anomalies of each variable across the six models (Table 3.1) because the ensemble mean results are generally closer to observations than individual model results under the current climate (Gleckler et al. 2008). IPSL-CM5A-LR has not archived latent heat for the *lgm* simulation, so we constructed the ensemble anomaly using latent-heat values from the other five models. For mapping and the calculation of ensemble averages, the output from each model was interpolated to a regular 2° latitude-by-longitude grid using bilinear interpolation.

In comparing land and ocean temperatures we defined the land as all grid points where land-area fraction (*sftlf*: variable names are those used in the CMIP5 NetCDF data sets) is more than 40% or sea-ice-area fraction (*sic*) is more than 40%. High-latitude amplification is defined as the ratio of surface temperature (*ts*) changes over the Northern Hemisphere extratropics (NHEXT, 30°N-85°N) to those over the Northern Hemisphere

Table 3.1. Models with *piControl*. *lgm*, and *abrupt4×CO_2* simulations from CMIP5 archive

Model name	Resolution (# of gridcells: lat, lon)		
	Atmopshere	Ocean	Sea Ice
Community Climate System Model version 4 (CCSM4)	192, 288	320, 384	320, 384
GISS ModelE version 2, Russell ocean model (GISS-E2-R)	90, 144	90, 144	90, 144
L'Institut Pierre-Simon Laplace Coupled Model version 5A low resolution (IPSL-CM5A-LR)	96, 96	149, 182	149, 182
Model for Interdisciplinary Research on Climate, earth system model (MIROC-ESM)	64, 128	192, 256	192, 256
MPI Earth System Model running in low resolution grid and paleo mode, (MPI-ESM-P)	96, 192	220, 256	220, 256
Meteorological Research Institute Coupled General Circulation Model version 3 (MRI-CGCM3)	160, 320	360, 368	360, 368

tropics (NHT, 0°-30°N) or over the Southern Hemisphere extratropics (SHEXT, 30°S-85°S) to those over the Southern Hemisphere tropics (SHT, 0°-30°S). Seasonality change is defined as the difference between summer (June-July-August, JJA, in the northern hemisphere and December-January-February, DJF, in the southern hemisphere) and winter (DJF in the northern hemisphere and JJA in the southern hemisphere) mean surface temperature. All averages were area-weighted (by the area of the 2°×2° grid cells).

We compare the spatial patterns of surface temperature changes and their partial-temperature-change (PTC) components in the *lgm* and *abrupt4×CO_2* experiments. We measure the similarity of any two map patterns (e.g. those of the multi-model mean surface-temperature changes or the PTC of each component in the energy balance model) using the weighted uncentered anomaly correlation (AC_U) which measures the similarity of two patterns without removal of the global mean, thereby assessing agreement in magnitude as well as pattern (Wilks 2011 p. 364). The AC_U correlation coefficient is bounded by ± 1.0; +1.0 indicates a perfect match in spatial pattern between reference and simulation, and -1.0 indicates a completely opposite spatial pattern between reference and simulation.

3. Methods: decomposition of temperature anomaly patterns using the surface energy balance

An energy balance model can be used to quantify the roles of specific forcings and feedbacks in the generation of temperature anomaly patterns (e.g. Winton 2006; Laine et al. 2009; Lu and Cai 2009). For equilibrium climate states represented by the CMIP5 simulations, outgoing longwave radiation approximately balances the incoming absorbed solar radiation (i.e. the TOA net radiation values are close to zero; SI Table 1). For an ideal surface, the radiation that is absorbed by the surface must be balanced by the total of the energy radiated back to atmosphere, gained or lost by latent and sensible heat, and the change in heat storage. Thus, the surface energy balance can be written as:

$$\left(1-\alpha_{surf}\right)SW\downarrow_{surf}^{all} + LW\downarrow_{surf}^{all} = LW\uparrow_{surf}^{all} + Q_H + Q_E + Q_G, \quad (1)$$

where α_{surf} is the surface albedo, which is the ratio of all-sky upward to downward shortwave radiation flux at the surface (i.e., $SW\uparrow_{surf}^{all} / SW\downarrow_{surf}^{all}$), and $LW\downarrow_{surf}^{all}$ and $LW\uparrow_{surf}^{all}$ are the all-sky downward and upward longwave radiation fluxes at the surface, Q_H and Q_E are the (nonradiative) surface sensible and latent heat fluxes, and Q_G is the flow of heat into or out of storage for land and or ocean (for oceans, this term includes the release of transported heat). Q_G is estimated as the residual term in the surface energy balance equation (1). For the radiative fluxes, positive values are defined to represent energy moving towards the surface, leading to surface warming, while negative values represent energy moving away from the surface, leading to surface cooling (Oke 1987). For the non-radiative fluxes, positive values represent flux away from the surface, leading to cooling, and negative toward surface, leading to surface warming. This sign convention thus associates radiative and non-radiative fluxes that either warm (positive) or cool (negative) the surface (Oke 1987).

The longwave radiation emitted by the surface can be represented by the Stefan-Boltzmann law for black bodies $LW\uparrow_{surf}^{all} = \varepsilon_{surf}\sigma T_{surf}^4$ where ε_{surf} is the emissivity of the surface, σ is Stefan's constant (5.67×10^{-8} W m^{-2} K^{-4}), and T_{surf} is the surface temperature (K). In practice, ε_{surf} is close to, but not exactly equal to 1.0 in the models (Jin and Liang 2006), and so following (Oke 1987)

$$LW\uparrow_{surf}^{all} = \varepsilon_{surf}\sigma T_{surf}^4 + \left(1-\varepsilon_{surf}\right)LW\downarrow_{surf}^{all}. \quad (2)$$

However, if we assume that the emissivity of the surface (ε_{surf}) is close to 1.0 at all wavelengths, then the outgoing longwave radiation can be approximately represented as $LW\uparrow_{surf}^{all} \approx \sigma T_{surf}^4$. The surface energy budget can then be written:

$$\sigma T_{surf}^4 \approx \left(1-\alpha_{surf}\right)SW\downarrow_{surf}^{all} + LW\downarrow_{surf}^{all} - Q_H - Q_E - Q_G. \quad (3)$$

Anomalies (relative to control) for the surface upward longwave radiation can be expressed as $\Delta LW\uparrow_{surf}^{all} \approx 4\sigma T_{surf}^3 \Delta T_{surf}$, where Δ is an anomaly operator that represents the experiment minus the *piControl* difference. Then, (2) can be rewritten as:

$$4\sigma T_{surf}^3 \Delta T_{surf} \approx \Delta\left[\left(1-\alpha_{surf}\right)SW\downarrow_{surf}^{all}\right] + \Delta LW\downarrow_{surf}^{all} - \Delta Q_H - \Delta Q_E - \Delta Q_G. \quad (4)$$

Following Lu and Cai (2009), the two radiative flux terms on the right-hand side of equation (3) can be decomposed into five radiative components: the surface albedo effect, surface shortwave cloud forcing, surface longwave cloud forcing, the change in surface clear-sky shortwave radiation, and the surface clear-sky longwave downward radiation. In the CMIP5 models, the surface albedo (α_{surf}) is generally > 0.6 for continental ice, snow and sea ice, < 0.1 for open ocean, and about 0.2 for vegetated ground. These differences mean that ice- and snow-covered areas play a strong role in the surface albedo effect (*SAE*) that warms or cools the climate in proportion to the size of ice- and snow-covered areas. The *SAE* can be quantified as follows:

$$SAE = -\Delta\alpha_{surf}\left(\overline{SW}\downarrow_{surf}^{all} + \Delta SW\downarrow_{surf}^{all}\right). \quad (5)$$

where the overbar denotes the *piControl* condition. The albedo effect is only active in a direct sense when shortwave radiation is received at the surface and thus is not important over polar regions in winter.

Surface cloud radiative forcing (CRF_{surf}) is defined as the difference between all-sky and clear-sky radiation at the surface:

$$\Delta SWCRF_{surf} = \Delta SW\downarrow_{surf}^{all} - \Delta SW\downarrow_{surf}^{clr}, \text{ and} \quad (6)$$

$$\Delta LWCRF_{surf} = \Delta LW\downarrow_{surf}^{all} - \Delta LW\downarrow_{surf}^{clr}, \quad (7)$$

where *clr* represents clear-sky conditions. $LWCRF_{surf}$ is a function of cloud temperature, height, and emissivity, and $SWCRF_{surf}$ is a function of cloud transmittance, surface albedo, and the solar zenith angle (Shupe and Intrieri 2004). Since a part of the SAE is included in the change of $SWCRF_{surf}$ (Soden et al. 2004), the surface albedo (α_{surf}) can be removed from the term as follows:

$$\Delta SWCRF_{surf} = \left(1-\overline{\alpha}_{surf}\right)\Delta\left(SW\downarrow_{surf}^{all} - SW\downarrow_{surf}^{clr}\right). \quad (8)$$

It follows that the α_{surf} is removed from the change in surface clear-sky shortwave radiation, and the surface clear-sky shortwave radiation can be quantified as

$$\left(1-\overline{\alpha}_{surf}\right)\Delta SW\downarrow_{surf}^{clr}, \quad (9)$$

where the overbar denotes the *piControl* condition. This term represents the change in GHG (in particular atmospheric CO_2 and water vapor) effects on clear-sky shortwave radiation. As the concentration of atmospheric GHGs increases, they absorb more incoming solar radiation in the atmosphere, leading to surface cooling, and the reverse is true.

The change in surface clear-sky longwave downward radiation, $\Delta LW{\downarrow}_{surf}^{clr}$, represents the sum of downward longwave radiation changes at the surface due to changes in atmospheric water vapor, the moist static energy transport by atmospheric motion, and CO_2 concentration. The increase in water vapor at lower-levels in the atmosphere in a warmer climate results in increased emission of longwave radiation to the surface (Santer et al. 2007), and the reverse is true in a cooler climate.

If we divide equation 4 by $4\sigma\overline{T}_{surf}^{3}$, we can write

$$\underset{[a]}{\Delta T_{surf}} \approx \underset{[b]}{\Sigma_{EBC}} / 4\sigma\overline{T}_{surf}^{3}, \quad \text{where} \tag{10}$$

S_{EBC} = (11)

$$(\underset{[c]}{SAE} + \underset{[d]}{\Delta SWCRF_{surf}} + \underset{[e]}{\Delta LWCRF_{surf}} + \underset{[f]}{\left(1-\overline{\alpha}_{surf}\right)\Delta SW{\downarrow}_{surf}^{clr}} + \underset{[g]}{\Delta LW{\downarrow}_{surf}^{clr}} - \underset{[h]}{\Delta Q_H} - \underset{[i]}{\Delta Q_E} - \underset{[j]}{\Delta Q_G}),$$

(and the characters in square brackets correspond to the labels in Figures 1-4). Each these terms shows the partial temperature change (PCT) contribution due to individual components of the energy balance to the total temperature anomaly (Lu and Cai 2009), and the sum of these contributions [b] will be approximately equal to the total surface temperature change. The surface temperature difference between [a] and [b] results from the linearization of surface upward longwave radiation adopted in the equation $\Delta LW{\uparrow}_{surf}^{all} \approx 4\sigma T_{surf}^{3}\Delta T_{surf}$ (Lu and Cai 2009), and a possible cause of this difference is variations of surface emissivity. If all the CMIP5 models had adopted the simple constant $\varepsilon_{surf} = 1.0$ in all climate states, [b] would be equal to [a]. However, almost all of the models adopt broadband surface emissivity ε_{surf} values slightly <1.0 (Jin and Liang 2006), and ε_{surf} depends on the surface types. Thus, there are changes in emissivity between different climate simulations because of the specification of different surface type. As a result, there is a residual term:

$$\Sigma_{EBC} / 4\sigma \overline{T}^{3}_{surf} - \Delta T_{surf} \quad (12)$$

which is labeled [k] in the figures.

4. Responses of the global surface flux change

Figures 3.1 and 3.2 show the ensemble-average annual surface temperature differences and partial temperature changes (PTC) of each component under the *abrupt4×CO₂* and *lgm* simulations. Depending on latitude and surface type (i.e. vegetated area/barren/ocean/sea ice/land ice), several components can be seen to be involved in the different responses. The responses of some components are robust, meaning that all models have the same responses (Fig. S3.2 and S3.3). In order to elucidate the first-order pattern and amplitude for both surface temperature change and PTC of each component, we separately describe the global-average values and spatial correlations over the land, ocean and land and ocean all grids (Fig. 3.3). To summarize the map patterns and examine spatial variability that may be hidden in large-scale averages, we also show the zonal-mean annual surface temperature differences and PTC of components in both warm and cold climates (Fig. 3.4). (Other maps and zonal-mean figures for seasonal mean temperature changes appear in the in SI.)

Annual-mean surface temperature for the *abrupt4×CO₂* simulations increases over all grid points (4.94 K, relative to the *piControl* simulation, Fig. 3.1[a], 3.3[a], and 3.4[a]). The differences are largest over land areas (6.82 K) and high-latitude ocean regions (Fig. 3.4[a]). The changes in winter (5.34 K for all grid points, 7.86 K for land, Fig. S3.4[a]) are larger than in summer (4.63K for all grid points, 6.61 K for land, Fig. S3.5[a]). The models show similar responses over most regions (Fig. S3.2[a] and S3.10[a]-S3.15[a]) except that two models (CCSM4 and GISS-E2-R) show changes of the opposite sign over the Labrador Sea and northern North Atlantic Ocean. In contrast, annual-mean surface-temperature for the *lgm* simulation has a robust response (Fig.

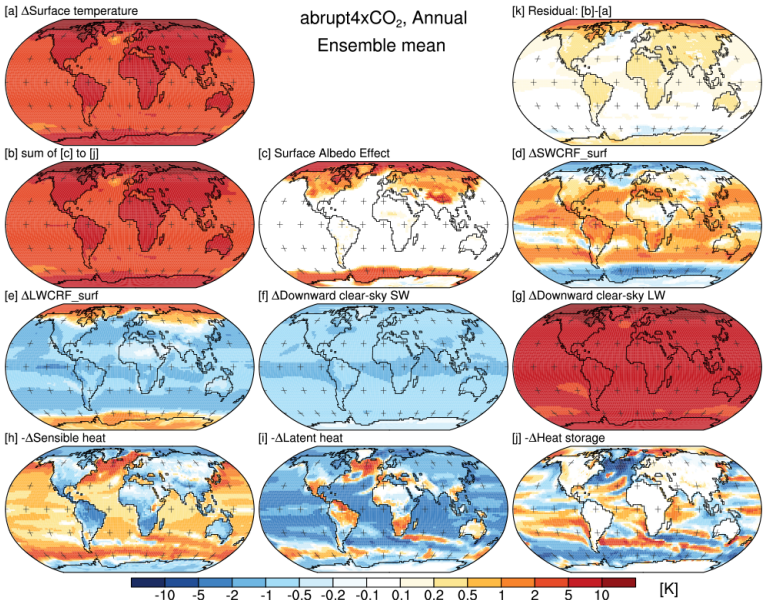

Figure 3.1. Maps of ensemble-average annual temperature differences between the *abrupt4×CO₂* and *piControl* simulations [a], and for the partial temperature change (PTC) of each component [b though j in equation 11], and the residuals [k] (equation 12)

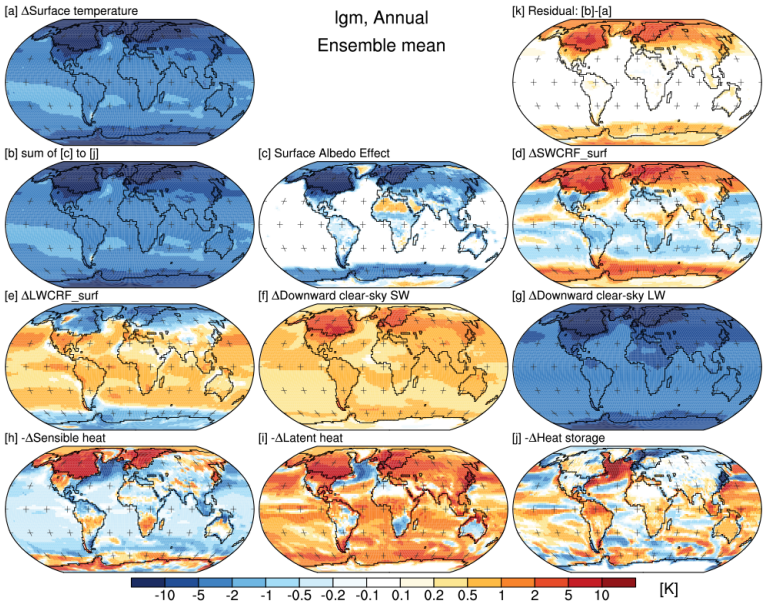

Figure 3.2. Maps of ensemble-average annual temperature differences between the *lgm* and *piControl* simulations [a], and for the partial temperature change (PTC) of each component [b though j in equation 11], and the residuals [k] (equation 12).

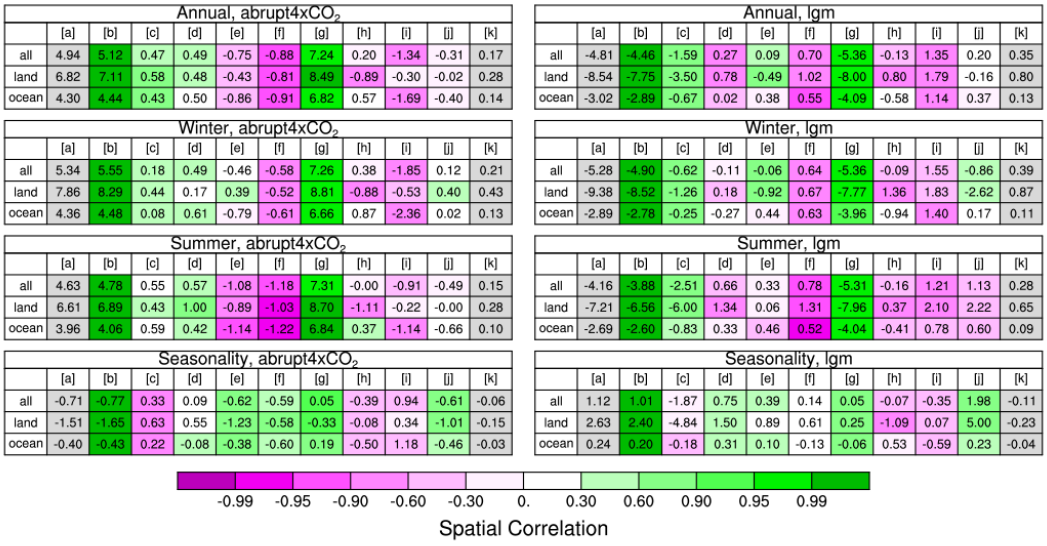

Figure 3.3. Multimodel mean, area-weighted global (85°S-85°N) average surface temperature anomalies ([a] and [b], K) and partial temperature changes (PTC) of each component ([c] to [k], K) (numbers), and weighted uncentered anomaly correlations (shading) between the CMIP5 surface temperature differences [a] and the estimated surface temperature changes [b] and the PTC of each component ([c] to [j]) for the abrupt4×CO2 simulations (left) and the lgm simulations (right). Summer means are for JJA in the Northern hemisphere and DJF in the southern hemisphere, winter means DJF in the northern hemisphere and JJA in the southern hemisphere, and seasonality means the difference between summer and winter.

S3.3[a] and S3.16[a]-21[a]) and decreases over all regions (-4.81 K, Fig. 3.2[a], 3.3[a], and 3.4[a]), in particular over continental ice sheets, high latitude land, and sea-ice covered areas of the Arctic Ocean. Again, the amplitude of temperature change in winter (-5.28 K for all grid points, -9.38 K for land, Fig. S3.7[a]) is larger than in summer (-4.16 K for all grid points, -7.21 K for land, Fig. S3.8[a]).

The annual surface temperature changes estimated using the energy-balance model (term [b]) show almost the same amplitude (5.12 K for all grid points, Fig. 3.1[b], 3.3[b], and 3.4[b]) and spatial pattern ($AC_U > 0.99$) in the *abrupt4×CO₂* simulations as the amplitude of ΔT_{surf} calculated directly from the CMIP5 multi-model mean (i.e. [a];

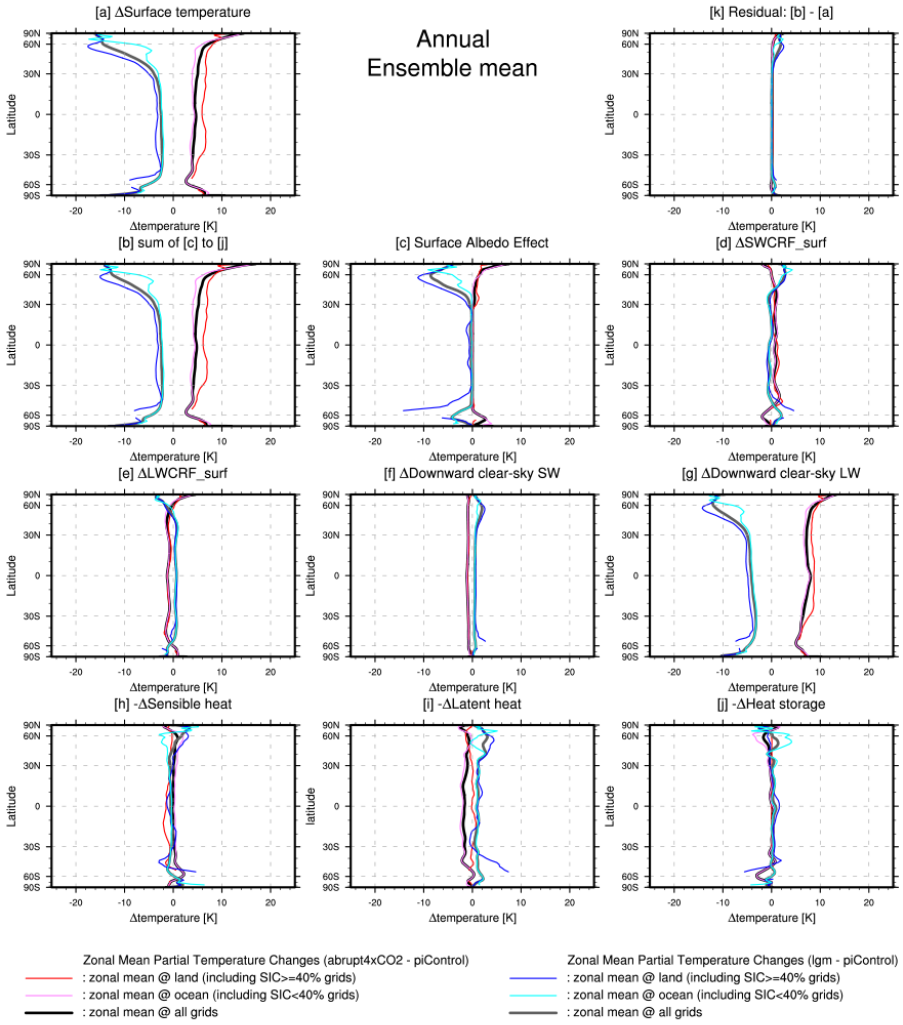

Figure 3.4. The ensemble-average zonal-mean annual surface temperature differences between the *abrupt4*×CO_2 and *lgm* and *piControl* simulations [a], and for the partial temperature change (PTC) of each component [b though j in equation 11], and the residuals [k] (equation 12); bold black (land + ocean), red (land only), and pink (ocean only) for *abrupt4*×CO_2; bold gray (land + ocean), blue (land only), and light blue (ocean only) for *lgm*.

4.94 K). Thus, the energy-balance estimates of surface temperature changes adequately reproduce the simulated temperature changes. All models show similar patterns (Fig. S3[b]). Surface temperature is slightly higher over the land and over the Arctic Ocean

compared to the temperatures calculated directly from the model output, and lower over the Labrador Sea and parts of the Southern Ocean (Fig. 3.1[b]). The average residual in the annual mean globally is 0.28 K over land areas, and 0.14 K over ocean areas. In contrast, the amplitude of the estimated surface-temperature changes in the *lgm* simulations are similar (-4.46 K for all grid points, Fig. 3.2[b], 3.3[b], and 3.4[b]) to the values obtained directly from the CMIP5 model output (-4.81 K, Fig. 3.2[a], 3.3[a], and 3.3[a]), and have very high AC_U values (> 0.99). The energy-balance estimates are lower over land-ice or sea-ice covered areas (Fig. 3.2[b]); this results in a residual of annual-mean surface temperature over land of 0.8 K. In both cold and warm climates, the residuals result from surface emissivity (ε_{surf}) values that are not unity and from combinations of changes in ε_{surf} , surface temperature, and surface downward longwave radiation.

The PTC components show four basic spatial patterns (Figs. 3.1, 3.2, and 3.3): (1) broad-scale patterns that are uniform in sign with very high (positive/negative) spatial correlation, such as those for downward clear-sky longwave radiation ($\Delta LW{\downarrow}_{surf}^{clr}$ [g]) and downward clear-sky shortwave radiation ($(1-\overline{\alpha}_{surf})\Delta SW{\downarrow}_{surf}^{clr}$ [f]);

(2) patterns that express surface-albedo contrasts with relatively high positive spatial correlation, such as (obviously) the surface albedo effect (SAE, [c]), but also surface shortwave cloud radiative forcing ($\Delta SWCRF_{surf}$ [d]) in the *lgm* simulations;

(3) patterns that show distinct land-ocean contrasts with relatively high negative spatial correlation, such as sensible heating ($-\Delta Q_H$ [h]) in the *abrupt4×CO₂* simulations;

and (4) patterns that show distinct high-low latitude contrasts, such as surface longwave cloud radiative forcing ($\Delta LWCRF_{surf}$ [e]) in the *lgm* simulations.

Sea-ice and snow-covered areas decrease for the *abrupt4xCO₂* simulation and increase for the *lgm* simulation. The surface albedo effect (*SAE*) contributes to the surface

temperature increases over the polar and higher altitude areas in the *abrupt4×CO₂* annual (Fig. 3.1[c] and 3.4[c]) and summer (Fig. S3.5[c] and S3.11[c]) climate. The *SAE* also reinforces the winter surface-temperature increases over the Northern Hemisphere mid-latitudes (Fig. S3.4[c] and S3.10[c]). However, over most of the mid-latitudes and in the tropics the *SAE* is small and not robust. In the *lgm* simulations, SAE reinforces surface-temperature decreases over the Arctic and Antarctic Oceans and mid- and high latitude land areas (particularly over the continental ice sheets), for annual (Fig. 3.2[c] and 3.4[c]) and summer mean climates (Fig. S3.8[c] and S3.11[c]) and to the decreases in surface temperature over the middle-latitude land regions in winter (Fig. S3.7[c] and S3.10[c]). The annual-mean PTC attributable to *SAE* over land is -3.50 K and -6.0 K in summer with relatively high spatial correlation (Fig. 3.3[c]).

In the *abrupt4×CO₂* experiments, surface shortwave cloud radiative forcing ($\Delta SWCRF_{surf}$, [d]) tends to reinforce surface temperature increases over the low- and middle-latitudes but to reduce positive temperature anomalies over the high latitudes regions (in particular the North Atlantic and the Arctic Oceans) annually (Fig. 3.1[d] and 3.4[d]) and during the summer (Fig. S3.5[d] and S3.11[d]). In the *lgm* simulations, in contrast, $\Delta SWCRF_{surf}$ reinforces the negative surface temperature anomalies in low latitudes and reduces the negative anomalies in in high latitudes (Fig. 3.2[d] and 3.4[d]), and has an effect opposite to SAE over high latitude regions. The large-scale spatial patterns are similar in both winter and summer (Fig. S3.7[d] and S3.8[d]), but the amplitude of PTC (in particular, on the continental ice-sheets) is much larger in summer (Fig. S3.11[d]) than in winter (Fig. S3.10[d]).

In the *abrupt4×CO₂* experiments, surface longwave cloud radiative forcing ($\Delta LWCRF_{surf}$ [e]) reinforces increases in surface temperature over high latitude regions (in particular, the Arctic Ocean) but acts to reduce the temperature increase over the low and middle latitude regions in annually (Fig. 3.1[e] and 3.4[e]) and winter (Fig. S3.4[e] and

S3.10[e]). However, $\Delta LWCRF_{surf}$ has a cooling effect over most of the world (except land-ice-covered regions such as Greenland and Antarctica) in summer conditions (Fig. S3.5[e] and S3.11[e]). In the *lgm* simulations, $\Delta LWCRF_{surf}$ reduces the negative temperature anomaly over the low latitudes and the mid-latitude oceans, but reinforces negative temperature anomalies over high latitude regions (in particular, over the ice sheets and sea-ice covered areas). The changes in cloud radiative forcing (ΔCRF_{surf}) are consistent with total cloud cover changes, and the large-scale spatial patterns of $\Delta LWCRF_{surf}$ and surface shortwave cloud radiative forcing ($\Delta SWCRF_{surf}$) are opposite (AC_U is -0.76 for annual *abrupt4×CO₂* and -0.78 annual *lgm* climate).

Downward clear-sky shortwave radiation ($(1-\bar{\alpha}_{surf})\Delta SW\downarrow_{surf}^{clr}$) always reduces the positive surface temperature anomalies (Fig. 3.1[f] and 3.4[f]) in the *abrupt4×CO₂* simulations, most markedly over the Arctic Ocean and inter-tropical convergence zone (ITCZ). The amplitude of this PTC component is larger in summer (-1.18 K) than in winter (-0.58 K). In contrast, $(1-\bar{\alpha}_{surf})\Delta SW\downarrow_{surf}^{clr}$ always increases the negative surface temperature anomalies in the *lgm* simulations, most markedly over the continental ice sheets (Fig. 3.2[f] and 3.4[f]). The magnitude of the PTC over the land varies seasonally (0.67 K in summer and 1.31 K in winter). There is a very high negative correlation (AC_U < -0.9) between surface temperature change and $(1-\bar{\alpha}_{surf})\Delta SW\downarrow_{surf}^{clr}$ in winter, summer and annually in both climates. The spatial pattern and amplitude in both warm and cold climates is likely associated with changes in water vapor distribution, because water vapor absorbs some shortwave radiation leading to less surface warming.

The downward clear-sky longwave radiation ($\Delta LW\downarrow_{surf}^{clr}$ [g]) always reinforces the positive surface temperature anomalies in the *abrupt4×CO₂* simulations (Fig. 3.1[g] and 3.4[g]). The amplitude of the annual PTC over land (8.49 K) is larger than over the ocean

(6.82 K), and the amplitude over the Arctic region is much larger than for other areas (Fig. 3.1[g] and 3.4[g]). In the *lgm* simulation, this term reinforces the negative surface-temperature anomalies everywhere and in all seasons (Fig. 3.2 and Fig 3.4[g]), and again all models show the same response (Fig. S3.3[g], S3.7[g], and S3.8[g]). As in the *abrupt4×CO₂* simulations, the amplitude of the annual PTC over land (-8.00 K) is larger than the over ocean (-4.09 K). There is high positive correlation ($AC_U > 0.9$) between changes in surface temperature (ΔT_{surf}) and downward clear-sky longwave radiation ($\Delta LW{\downarrow}_{surf}^{clr}$) in all seasons in both warm and cold climates, and indeed this term displays the greatest similarly to the ΔT_{surf} of all of the energy-balance components (Fig. 3.1[g], 3.2[g], and 3.3[g]).

In the *abrupt4×CO₂* simulations, sensible heating ($-\Delta Q_H$ [h]) reduces the positive surface temperature anomalies over most land areas (-0.89 K), and increases it over the ocean (0.57 K) except the Southern and Arctic Oceans (Fig. 3.1[h] and 3.4[h]). In the *lgm* simulations, $-\Delta Q_H$ (Fig 3.2[h] and 3.4[h]) reduces the negative temperature anomaly over the continental ice sheets and some land regions (western North America, central South America, East Asia, and southern Africa). It increases the negative surface temperature anomaly over almost all ocean regions (-0.58 K), except for the Arctic and Antarctic Oceans where sensible heating reduces the negative temperature anomalies because of increased sea-ice cover. There is relatively high negative correlation ($AC_U \approx$ -0.6) between surface temperature change and the PTC of this term over land throughout the year in both climates.

Latent heating ($-\Delta Q_E$ [i]) reduces the positive surface-temperature anomalies over most of the globe (-1.34 K; Fig. 3.1[i] and 3.4[i]) in the *abrupt4×CO₂* simulation, except in regions where the simulated reduction in precipitation is large (e.g. northern Atlantic Ocean, southern North America, Amazon, southern Africa). The magnitude of the PTC over all grid points in winter (-1.85 K, Fig. S3.4[i] and S3.10[i]) is much larger

than in summer (-0.91 K, S3.5[i] and S3.11[i]). In contrast, in the *lgm* simulations, $-\Delta Q_E$ results in increase in annual surface temperature (Fig. 3.2 and 3.4[i]) over the most of the globe (1.35 K) and especially over the land (1.79 K). There is a relatively high negative AC_U (≈ -0.7) over the ocean between surface temperature change (ΔT_{surf}) and the latent heating ($-\Delta Q_E$) through the year in both climates.

Changes in heat storage ($-\Delta Q_G$ [j]) show much larger responses over the oceans than over the land (Fig. 3.1[j], 3.3[j], and 3.4[j]). In the *abrupt4×CO₂* simulations, heat storage reduces the positive surface-temperature anomaly over the Arctic Ocean in summer (Fig. S3.5[j] and S3.11[j]) and increases it in winter (Fig. S3.4[j] and S3.10[j]) resulting in a reduction of the positive surface temperature anomalies over the North Atlantic Ocean throughout the year. The opposite is seen in the *lgm* simulations (Fig. 3.2[j], 3.3[j], and 3.4[j]): heat storage enhances the decrease in the surface-temperature in summer (Fig. S3.8[j] and S3.11[j]) and reduces it in winter (Fig. S3.7[j] and S3.10[j]) over both the Arctic and Antarctic Oceans because of changes in sea-ice cover, and helps to reduce the overall cooling in the North Atlantic. Changes in heat storage ($-\Delta Q_G$) over tropical land areas are much larger in the *lgm* simulations than the *abrupt4×CO₂* simulations, and help to limit the surface-temperature cooling in these regions. However, globally, the impact of $-\Delta Q_G$ is small and the signs of the anomalies differ from model to model.

5. Key components of the large-scale temperature responses

We explore the key components responsible for generating land-ocean contrast, high-latitude amplification, and seasonality changes for different spatial and temporal targets for the ensemble of warm (*abrupt4×CO₂*) and cold (*lgm*) climate simulations. Fig. 3.5 shows the amplitude of surface temperature change and PTC of each component, while Fig. 3.6 shows the association (spatial pattern-correlations) between CMIP5 surface

temperatures and both estimated surface temperature and PTC of components. Here, we simply regard the key components of the temperature responses as those components with larger amplitudes (Fig. 3.5) and higher spatial correlations (Fig. 3.6).

5.1. Land-ocean contrast

Globally, land-ocean contrast (Fig. 3.5) is smaller in the annual mean *abrupt4×CO₂* simulations (1.73) than in the annual mean *lgm* simulations (3.07), although the values for the tropics are similar (1.63 versus 1.57). Over the Southern Hemisphere (SH, 0°-60°S), the contrast in annual mean *abrupt4×CO₂* simulations (1.70) is larger than one in the annual mean *lgm* (1.52). The contrast over the NHEXT is larger in winter (1.80 in the *abrupt4×CO₂* simulation, 2.99 in the *lgm*) than in summer (1.44 in *abrupt4×CO₂*, simulation, 2.32 in *lgm*). The land-sea contrast calculated using the energy-balance approach is slightly larger in the annual mean *abrupt4×CO₂* simulations (1.77 compared to 1.73 calculated directly) but somewhat smaller in the annual mean *lgm* simulations (2.86 versus 3.07) because of the larger positive residuals over land.

Downward clear-sky longwave radiation ($\Delta LW{\downarrow}_{surf}^{clr}$ [g]) is the single most important component that intensifies land-ocean contrast in the *abrupt4×CO₂* simulations, in all regions and seasons (Fig. 3.5 and 3.6). Latent heat flux ($-\Delta Q_E$ [i]) also plays an important role in intensifying land-sea contrast in annual mean climate, in particular over the tropics. Surface longwave cloud radiative forcing ($\Delta LWCRF_{surf}$ [e]) contributes to amplifying the contrast in winter and heat storage ($-\Delta Q_G$ [j]) contributes in summer over the NHEXT. Surface albedo feedback (*SAE* [c]) and downward clear-sky shortwave radiation ($(1-\bar{\alpha}_{surf})\Delta SW{\downarrow}_{surf}^{clr}$ [f]) slightly act to amplify the contrast. Conversely, sensible heat flux ($-\Delta Q_H$ [h]) strongly reduces the contrast in all regions and seasons.

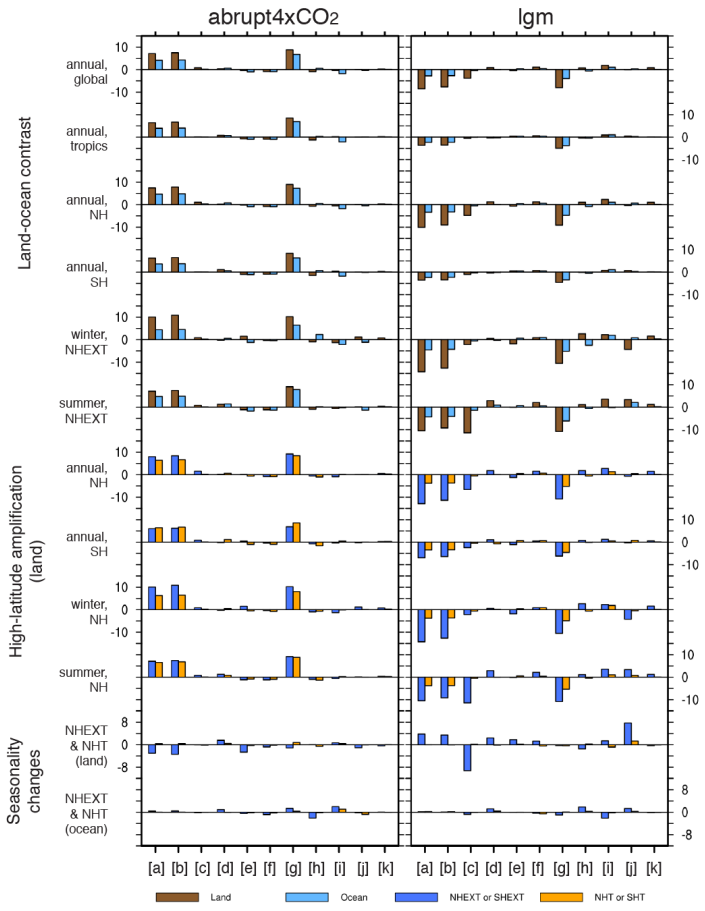

Figure 3.5. Multi-model mean area-weighted averages of the anomalies in surface temperature [a] and in the partial temperature change (PTC) of each component [c through j in equation 11] from the energy-balance model) for the *abrupt4×CO₂* simulation (left) and the *lgm* simulations (right) in K. Column [k] gives the change in the residual term (equation 12). The individual rows represent different aspects of the large-scale surface temperature response and its PTC: land-ocean contrast (rows 1 to 6) addressed as differences in annual temperature for the globe (60°S-85°N), tropics (30°S-30°N), northern hemisphere (NH: 0-85°N), and southern hemisphere (SH: 60°S-0), and for the northern hemisphere extratropics (NHEXT: 30-85°N) in winter (DJF mean) and summer (JJA mean); high-latitude amplification (rows 7 to 10) addressed as annual, winter and summer surface temperature differences for the Northern/Southern Hemisphere extratropics (30°N-85°N/ 85°S-30°S; dark blue) and Northern Hemisphere tropics (0-30°N/ 30°S-0; orange) respectively; seasonality (rows 11 to 12) addressed as the difference between winter and summer temperatures for the Northern Hemisphere extratropics (dark blue) and Northern Hemisphere tropics (orange) (over the land and ocean) respectively

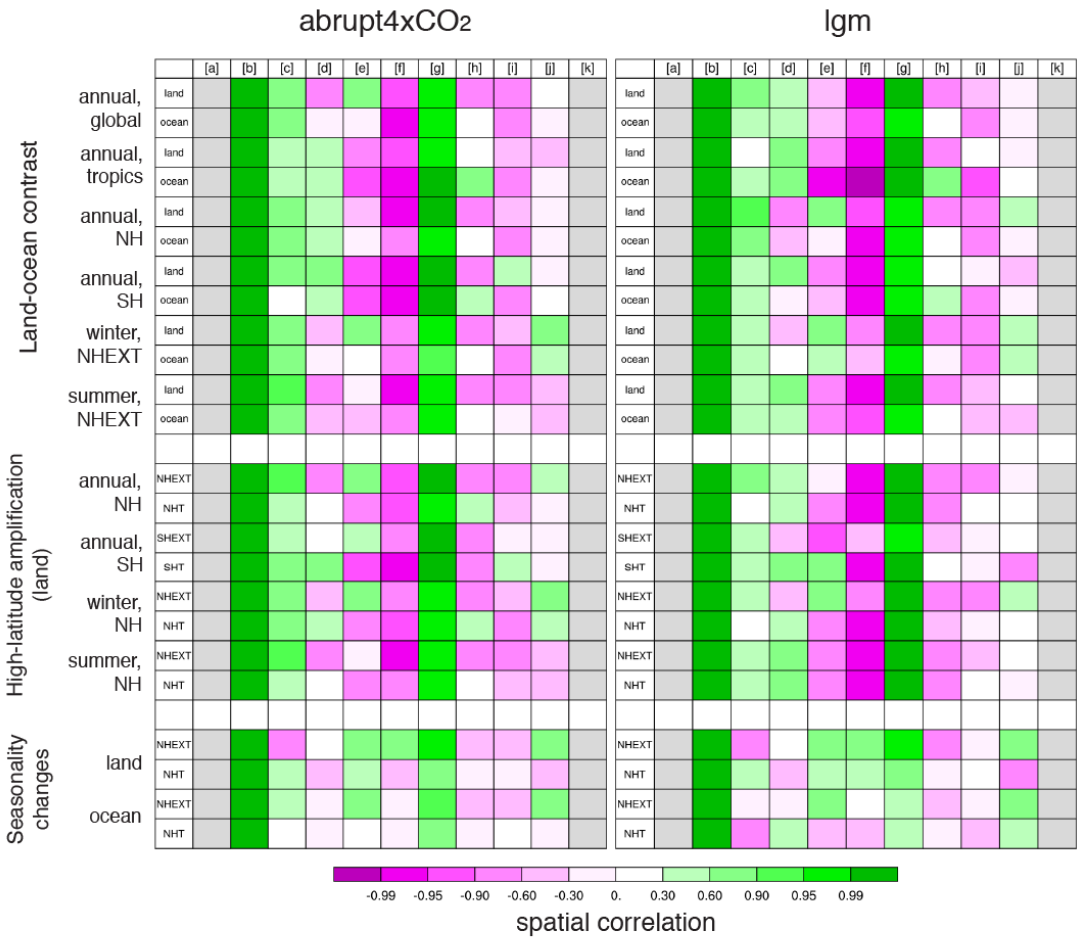

Figure 3.6. Area-weighted uncentered pattern correlations between the CMIP5 surface temperature and both estimated surface temperature and its partial temperature changes (PTC) under the *abrupt4×CO₂* simulation (left) and the *lgm* simulations (right). The individual rows of tables show each spatial and temporal target of large-scale surface temperature response and its PTC of each component. The column characters [a] to [k] correspond to the terms in the energy balance model (equation 10, 11, and 12 The correlation coefficient is bounded by ± 1.0; +1.0 indicates a perfect match between reference and simulation in spatial pattern (plotted in green), and -1.0 indicates the completely opposite spatial pattern (magenta) between reference and simulation. The correlations (and amplitude of differences) show that estimated surface temperature changes adequately reproduce the surface temperature changes and that clear-sky longwave radiation [g] is the key component of large-scale temperature changes, in particular of the land-ocean contrast and high-latitude amplification (as indicated by very high correlation coefficients and large amplitudes of changes).

Downward clear-sky longwave radiation ($\Delta LW\downarrow_{surf}^{clr}$ [g]) is also the most important component amplifying land-ocean contrast in the *lgm* simulations (Fig. 3.5 and 3.6). However, *SAE* [c] is also an important amplifier in the *lgm* simulations, except in winter over the NHEXT where change in heat storage [j] is more important in enhancing this contrast. Sensible heat flux flux ($-\Delta Q_H$ [h]) also contributes to reducing the contrast in winter over the NHEXT, while surface longwave cloud radiative forcing ($\Delta LWCRF_{surf}$ [e]) works to increase the contrast. Surface shortwave cloud radiative forcing ($\Delta SWCRF_{surf}$ [d]), downward clear-sky shortwave radiation ($(1-\bar{\alpha}_{surf})\Delta SW\downarrow_{surf}^{clr}$ [f]), sensible heat flux ($-\Delta Q_H$ [h]), and latent heat flux ($-\Delta Q_E$ [i]) generally reduce land-ocean contrast in all regions and seasons.

5.2. High-latitude amplification

High-latitude amplification over the Northern Hemisphere is smaller year round in the *abrupt4×CO₂* than in the *lgm* simulations, as would be expected given the large ice sheets in the *lgm* simulations (Fig. 3.5). The magnitude of the amplification is larger in winter (1.61 in *abrupt4×CO₂*, 3.77 in *lgm*) than in summer (1.08 versus 2.78). The change estimated from the energy-balance approach ([b]) is underestimated compared to the CMIP5 multi-model mean surface temperature ([a]) in the *lgm* and overestimated in the *abrupt4×CO₂* because of the larger residuals over the NHEXT land. On the Other hand, multi-model mean high-latitude amplification over the Southern Hemisphere does not occur under the annual mean *abrupt4×CO₂* simulations (0.92) even though CCSM4 and MRI-CGCM3 simulate high-latitude amplification there (Fig. S3.1).

The surface albedo effect (*SAE* [c]), surface longwave cloud radiative forcing ($\Delta LWCRF_{surf}$ [e]), and downward clear-sky longwave radiation ($\Delta LW\downarrow_{surf}^{clr}$ [g]) are the key components enhancing high-latitude amplification in the *abrupt4×CO₂* simulations,

although SAE does not influence amplification in winter, and $\Delta LWCRF_{surf}$ and $\Delta LW{\downarrow}_{surf}^{clr}$ have no impact in summer (Fig. 3.5 and 3.6). On the other hand, latent heat flux ($-\Delta Q_E$ [i]) reduces the amplification especially in summer. The other energy-balance components only have a small (and inconsistent) impact on high-latitude amplification in the different seasons.

Surface albedo feedback (*SAE* [c]) and downward clear-sky longwave radiation ($\Delta LW{\downarrow}_{surf}^{clr}$ [g]) are again the key components for enhancing high-latitude amplification under the *lgm* climate, but *SAE* [c] is more important in summer than winter; heat storage ($-\Delta Q_G$ [j]) plays a more important role in the winter amplification (Fig. 3.5 and 3.6). Although surface longwave cloud radiative forcing ($\Delta LWCRF_{surf}$ [e]) and heat storage ($-\Delta Q_G$ [j]) tend to increase the amplification, surface shortwave cloud radiative forcing ($\Delta SWCRF_{surf}$ [d]), and downward clear-sky shortwave radiation ($(1-\overline{\alpha}_{surf})\Delta SW{\downarrow}_{surf}^{clr}$ [f]), sensible heating ($-\Delta Q_H$ [h]), and latent heating ($-\Delta Q_E$ [i]) diminish the amplification.

5.3. Seasonality changes

Most of the ocean areas with regard to seasonality changes are not robust and the amplitude is quite small in both warm and cold climates (Fig. 3.5, S3.6, S3.9, and S3.12). The annual cycle is reduced over high-latitude land regions and the Arctic Ocean in the *abrupt4×CO₂* simulations (Fig. S3.12), but varies both longitudinally and latitudinally over middle- and low-latitude land areas (Fig. S3.6). No single component stands out as the dominant influence of the changes in seasonality in the *abrupt4×CO₂* simulations: surface shortwave cloud radiative forcing ($\Delta SWCRF_{surf}$ [d]) increases seasonality and surface longwave cloud radiative forcing ($\Delta LWCRF_{surf}$ [e]) reduces seasonality in both NHT and NHEXT areas; downward clear-sky longwave radiation ($\Delta LW{\downarrow}_{surf}^{clr}$ [g]) reduces seasonality in higher latitudes and intensifies it in low- and mid-latitudes of North

America and Europe; sensible heating ($-\Delta Q_H$ [h]) reduces and latent heating ($-\Delta Q_E$ [i]) intensifies seasonality in the tropics.

The pattern of seasonality changes in the *lgm* simulations is spatially complex, such that the large-scale averages (NHEXT and NHT) do not provide a coherent picture (Fig. S3.9). Seasonality is reduced over the land-ice regions in North America, but is enhanced over the land-ice regions in Europe (Fig. S3.9). However, the temperature patterns are consistent with the pattern of downward clear-sky longwave radiation ($\Delta LW{\downarrow}_{surf}^{clr}$ [g]). The other components in the energy balance model show similar responses over the NHEXT land areas and sea-ice covered areas of the Arctic Ocean: surface albedo (*SAE* [c]) and sensible heating ($-\Delta Q_H$ [h]) reduce seasonality, but all the other components increase seasonality.

6. Discussion and conclusion

While several energy-balance components are involved in surface temperature changes, only certain components show robust and consistent patterns across multiple models in both warm and cold climates. Changes in surface downward clear-sky longwave radiation ($LW{\downarrow}_{surf}^{clr}$) show a very high positive spatial correlation with changes in surface temperature, robustly accounting for most of the overall change in surface temperature in both warm and cold climates. The surface albedo effect (*SAE*) makes a large contribution to surface-temperature changes in summer over the high latitudes in both warm and cold climates. In contrast, some other components, such as non-radiative fluxes and surface longwave cloud radiative forcing ($LWCRF_{surf}$), have limited influence on the large-scale temperature responses.

Our results identify surface downward clear-sky longwave radiation ($LW{\downarrow}_{surf}^{clr}$) as the most important component in the amplification of land-ocean contrast in both warm

and cold climates in all regions and seasons. Similar results for a warm-climate state were found by Lu and Cai (2009). These results support the idea that ocean-forced changes in atmospheric circulation and water-vapor transport play a significant role in generatiing land-ocean contrast through temperature and humidity changes in the upper troposphere (Santer et al. 2005; Karl et al. 2006), which in turn generate changes in surface downward clear-sky longwave radiation over land (Compo and Sardeshmukh 2009). Differences in tropospheric lapse rates over land and ocean, caused by constraints on moisture availability over land compared to the ocean (see e.g. Li et al. 2013; Byrne and O'Gorman 2013b) also affect land-ocean contrast (Joshi et al. 2008; Byrne and O'Gorman 2013a): while the dry adiabatic lapse rate is independent of saturation specific humidity, the saturated adiabatic lapse rate decreases/increases with increasing/decreasing saturation specific humidity. Different changes in lapse rates over land and ocean imply different changes in surface temperature, with larger changes over the land than over the ocean. To explore in detail the relationship between our result and previous studies, $LW{\downarrow}_{surf}^{clr}$ must be decomposed to show the separate effects of changes in CO_2, water vapor, and direct LW feedback.

In contrast, previous studies (e.g. Sutton et al. 2007; Laine et al. 2009) have suggested that non-radiative fluxes, i.e. latent heat flux (Q_E) and sensible heat flux (Q_H), play a major role in the generation of land-ocean contrast; this is not borne out by our analyses. While Q_E apparently intensifies land-ocean contrast in the annual mean in the *abrupt4×CO₂* simulation, this comes about through changes in seasonal heat storage (Q_G). Furthermore latent heat flux does not contribute to the intensification of land-ocean contrast in the *lgm* climate. Our analyses also indicate that neither surface shortwave cloud radiative forcing ($SWCRF_{surf}$) nor the GHG effects of downward clear-sky shortwave radiation have a strong impact on the intensification of land-ocean temperature

contrast, although some previous studies have argued that both are important (e.g. Joshi and Gregory 2008; Dong et al. 2009).

Our analyses show that surface downward clear-sky longwave radiation ($LW\downarrow_{surf}^{clr}$) is also a key component for intensifying high-latitude amplification in both warm and cold climates (see also Lu and Cai (2009)). These results are consistent with previous work on high-latitude amplification in warm climates (e.g. Graversen and Wang 2009; Winton 2006) showing that changes in atmospheric water vapor lead to increased air temperature and reduced sea-ice cover and thus engender a strong longwave radiation feedback. Solomon (2006) has argued that an increase in the meridional, atmospheric energy transport in the Northern Hemisphere is to be expected in a warmer climate, because more latent heat energy release will occur over the oceans leading to increased baroclinicity. Moreover, an increase in atmospheric water vapor will increase the greenhouse effect in the Arctic more than in lower latitudes, linked in part to stable stratified conditions over the Arctic which inhibits mixing (Alexeev et al. 2005; Langen and Alexeev 2007; Lu and Cai 2010).

The surface albedo effect (*SAE*) is important in both land-ocean contrast and high-latitude amplification. We have shown that *SAE* strongly enhances land-ocean contrast in the *lgm* climate, although it is not important in the warm climate state. *SAE* enhances the *lgm* land-ocean contrast because of the presence of large continental ice sheets and extensive snow cover in the high-latitude regions. The additional contribution of *SAE* in the *lgm* experiment helps to explain the larger amplitude of land-ocean contrast in cold than warm climates (Izumi et al. 2013). The surface albedo effect also plays a significant role in generating the high-latitude amplification in summer (and hence in annual average) in both warmer and cooler climates. However, *SAE* does not contribute to high-latitude amplification in winter, which is primarily the result of changes in heat storage. Amplification of the temperature changes is not confined to strictly polar regions (Brady et al. 2013) – pointing to the contributing role of ice- and snow-albedo feedback in

generating this large-scale temperature response, particularly in winter (e.g. Screen and Simmonds 2010b).

Our results suggest that, while important, the surface albedo effect (*SAE*) is secondary to surface downward clear-sky longwave radiation ($LW{\downarrow}_{surf}^{clr}$) in the intensification of high-latitude amplification. This is consistent with previous studies. For example, high-latitude amplification occurred in a CCSM3 simulation in which albedo was fixed (Graversen and Wang 2009) and in an idealized GCM simulation in which ice-albedo feedback is absent (Lu and Cai 2010), and thus *SAE* could not be involved. Moreover, high-latitude amplification is found in aquaplanet simulations in which ice-albedo feedback was excluded, resulting from the impact of changes in longwave radiation and turbulent fluxes on high-latitude surface temperature (Alexeev et al. 2005; Langen and Alexeev 2007). Thus, we suggest that $LW{\downarrow}_{surf}^{clr}$ is the dominant factor leading to high-latitude amplification (Lu and Cai 2009), and *SAE* contributes to the intensification during summer.

The generation of changes in seasonality in response to year-round changes in forcing is a robust feature in both warm and cold climates, although the nature of the change varies between land and ocean and between high- and low-latitudes (e.g. Mann and Park 1996; Dwyer et al. 2012a; Izumi et al. 2013). In contrast with the other large-scale temperature responses, no single factor stands out as the major mechanism explaining the simulated seasonality changes. In the *abrupt4×CO₂* climate, the seasonality changes at high-latitudes are produced through changes in both surface longwave cloud radiative forcing ($LWCRF_{surf}$) and surface downward clear-sky longwave radiation ($LW{\downarrow}_{surf}^{clr}$). However, neither component is important in the *lgm* climate, where heat storage (Q_G) intensifies high-latitude seasonality and the surface albedo effect (*SAE*) reduces it. Although $LWCRF_{surf}$ contributes to the simulated change in seasonality

in low latitudes in the *abrupt4×CO_2* simulations, it is not important in the *lgm* simulations. Our analyses therefore suggest that simulated changes in seasonality are a consequence of the changes in land-ocean and high-latitude/low-latitude contrasts rather than an independent temperature response to the large-scale forcing.

Changes in land-ocean contrast and high-latitude amplification are robust features of climate-model simulations of the future (e.g. Joshi et al. 2013; Taylor et al. 2013; Byrne and O'Gorman 2013b) and a wide range of different palaeoclimates (e.g. Otto-Bliesner et al. 2006; Dowsett et al. 2012a; Laine et al. 2009). These responses are shown by palaeoclimate data (e.g. Kageyama et al. 2013; Dowsett et al. 2012a; Harrison et al. 2013; Izumi et al. 2013) and thus are features of the real climate rather than simply modeled responses. These responses can be explained through changes in the surface energy balance, but most specifically through a small number of feedbacks impacting surface downward clear-sky longwave radiation ($LW{\downarrow}_{surf}^{clr}$). Although several previous studies have pointed to the importance of $LW{\downarrow}_{surf}^{clr}$ in explaining large-scale temperature responses, they have tended to focus on single experiments and/or regions. Here, we have been able to provide a more comprehensive explanation of these large-scale phenomena through combining analyses of past and future climates. This demonstrates the way in which palaeoclimate simulations are a useful adjunct to analyses of modern-day climates in understanding the fundamental mechanisms of climate change.

7. Chapter III bridge paragraph

In chapter II and III, we explored the consistent climate changes between past and future simulations and their mechanism. These studies were based on the evidence that similar patterns also appear in historical observations and paleoclimate reconstructions. In order to develop paleoclimate diagnostics, we require spatially and temporally expanded quantitative reconstructed data for data-model comparison. Therefore, in

chapter IV, we show one example of the North American paleoclimate reconstruction with iterative forward-modeling approach.

CHAPTER IV

THE ITERATIVE FORWARD-MODELING APPROACH FOR PALEOCLIMATIC RECONSTRUCTION: CLIMATE CHANGES OVER NORTH AMERICA AT THE MID-HOLOCENE AND LAST GLACIAL MAXIMUM

This chapter is in preparation for submission to *Climate of the Past* as a co-authored article with P.J. Bartlein. I conceived of the overall experiments and analyses with Fortran and R, and wrote the initial draft of the paper. P.J. Bartlein made the modern climate data used in the analysis and a Fortran program for making gridded data, and was involved in discussion of the results, and in design and drafting of the final paper.

1. Introduction

By devoting an entire chapter of the fourth and fifth assessment reports (IPCC 2007, 2013) to paleoclimate, the Intergovermental Panel on Climate Change (IPCC) has recognized that studying past climates is important for understanding the climate system, and thus for projecting future climates. Although climate-model simulations of modern climate can be compared with gridded global data sets such as satellite remote sensing and reanalysis data to evaluate the performance of models, the observed data in the instrumental period includes smaller climate variations than those likely to occur in the future. Therefore, in order to project future climate under potentially larger forcings than those observed in the instrumental record, we need to understand the climate responses to past external forcing and internal boundary conditions to evaluate how well climate models work under those different conditions. One common method for evaluating a climate model is by data-model comparisons.

There are two basic approaches for paleo data-model comparison: the inverse (or inverse-modeling) approach and the forward-modeling approach (Kohfeld and Harrison

2000). The inverse approach (bottom-up approach) has been the classical approach in paleoclimate reconstruction (Bradley 2014). Paleoclimate data record the responses of the Earth system to past climate changes, and thus the evidence acts as a "proxy" for actual measurement of those past climate changes (Bradley 2014). However, there are several statistical and ecological assumptions that must be satisfied when making inferences from paleoclimate data (Guiot et al. 2009). These assumptions are that (1) climate is the ultimate cause of changes in paleoenvironmental data, (2) interactions between species and climate remain the same through time, and (3) the modern data contain all the necessary information to interpret the paleodata. Furthermore, there is a possibility that indeterminacy of the paleoclimate data can exist, even if the technical assumptions are satisfied, because different climates could give rise to similar paleoclimatic data. The specific controls of a particular paleoclimatic record thus cannot always be uniquely and clearly determined from the data alone (Sloan and Barron 1992). Consequently, even if the paleoclimate conditions are known without error, they alone cannot bring out the controls or mechanisms involved in the past climates. Moreover, the inverse approach is problematic in areas with little or no modern reference data.

The forward-modeling approach is a top-down approach. As Bartlein (1997) stated, climate variations occur with a hierarchy of controls and responses, which begin at the highest level with the external controls of climate (boundary conditions), through global-to regional scales, and end with the variations of individual environmental systems at specific sites (local scales) at the lowest level. Responses at any one level of the hierarchy become the controls of the components at a lower level. In practice, this top-down approach begins with assumptions regarding the state of the large-scale controls of climate (boundary conditions) and applies the boundary conditions to a climate model. The climate model simulates potential responses to this particular configuration of the controls, and,these simulations can be input to subsystem models such as equilibrium biogeography models. The subsystem process-based models are used to predict the

response of paleoenvironmental indicators (e.g. vegetation) to the simulated climate. The subsystem model output (known as simulated paleoclimatic indicators) is then compared with the available observedpaleoclimatic indicators, such as pollen data converted into plant functional types or biomes.

One of the significant disadvantages of the inverse-modeling approach is the assumption that the dependence of vegetation on climate is not mediated by changing atmospheric CO_2 level or soil development. Polar ice core records, however, indicate that atmospheric CO_2 concentration varies through time and some plant physiological studies (e.g. Farquhar 1997; Jolly and Haxeltine 1997; StreetPerrott et al. 1997) have showed differing response of vegetation to atmospheric CO_2 levels, so the assumption that CO_2 level and soil are not mediating climate effects may lead to considerable bias (Cowling and Sykes 1999; Prentice and Harrison 2009). In order to resolve the issues that result from the inverse-modeling approach, Guiot et al. (2000) and Wu et al. (2007) proposed the inverse vegetation modeling (IVM) approach for climate and vegetation reconstruction over Eurasia and Africa. We refer to the IVM approach as the "inverse modeling through iterative forward-modeling" (IMIFM) approach here because this expression best describes the underlying processes. The IMIFM approach has the potential to provide more accurate quantitative climate estimates (with smaller confidence limits) from pollen records than statistical approaches because it allows the mechanistic effects of non-climatic variables, like the atmospheric CO_2 concentration, to be explicitly considered in the reconstructions.

We adopted the IMIFM approach for paleoclimatic reconstruction since the Last Glacial Maximum (LGM, about 21,000 years ago) over North America in order to produce better (i.e. less dependent on the assumptions) quantitative climate data for paleo data-model comparison. In this study, we focused on the two key periods in the latest Coupled Modelling Intercomparison Project (CMIP5; Taylor et al. 2012) and Paleoclimate Modeling Intercomparison Project (PMIP3), LGM and mid-Holocene (MH,

about 6000 years ago) because the global bioclimatic synthesis data (i.e. Bartlein et al. 2011) does not include data from the IMIFM approach over North America and because it is essential for updating this data synthesis in order to understand the mid-Holocene and LGM environmental conditions.

2. Data

The fossil-pollen data are taken from the Neotoma paleoecology database (www.neotomadb.org), which is a multiproxy relational database that contains fossil data for the Pliocene and Quaternary. The fossil-pollen data in the Neotoma database are available for over 1000 sites (including NEOTOMA pending data) in North America. The data were taxonomically standardized (Williams 2003; Williams et al. 2004), and recently updated to improve temporal uncertainty in eastern North America (Blois et al. 2011). We have taken the closest sample to 6000 ^{14}C years BP (± 500 years) for the MH, and 18000 ^{14}C years BP (± 1000 years) for LGM. This selection process resulted in 777 sites for modern (0ka ± 50 years; the core-top data), 786 sites for the MH, and 79 sites for the LGM, that were included in this study.

For running the equilibrium vegetation models used in this study, monthly mean climate data (near-surface temperature, precipitation, and percent possible sunshine), absolute minimum temperature, soil physical properties (water holding capacity and percolation rate), insolation, and atmospheric CO_2 concentration are required. We used CRU CL 2.0 1961-1990 observed monthly mean climate data that covers the global land surface at a 10-minute spatial resolution (New et al. 2002). We used an elevationally adjusted interpolation procedure to downscale the CRU CL2.0 data to each pollen site. For each pollen site, we extract the monthly climate data and elevation data for the four closest grid-cells and calculate bilinear-interpolated climate values. A local lapse-rate based elevation adjustment is carried out based on the difference between pollen site elevation and the elevation from the four neighboring CRU CL2.0 grid-points. Absolute

minimum temperature (T_{min}) was based on the relationship between T_{min} and mean temperature of the coldest month, estimated using a weather-station data set of absolute minimum temperatures (Müller 1982). Soil properties were derived from the FAO digital soil map of the world (FAO, 1995). Insolation for modern and LGM simulations is the same because of no large differences, and insolation for the MH simulation is considered for the orbitally induced changes in insolation. Atmospheric CO_2 concentration for the past was taken from boundary conditions for CMIP5 paleoclimate simulations; 280 ppmv for the MH and 185 ppmv for the LGM. The modern CO_2 concentration was set to 333 ppmv as the mean value in the period of the baseline climatology (http://data.giss.nasa.gov/). Because some pollen samples do not include elevation information, we interpolated elevations at the pollen site, using the Shuttle Radar Topography Mission elevation data on a horizontal grid spacing 30 arc-seconds (SRTM30) (http://topex.ucsd.edu/WWW_html/srtm30_plus.html).

3. Method

The basic assumption of the IMIFM climate reconstruction approach is that it should be possible to reconstruct the likely climate data that gave rise to a "target" paleovegetation sample by searching for the set of climate values, that when input to the "forward" vegetation model (along with other parameters, like CO_2 concentrations), simulates vegetation that resembles the target paleovegetation sample. In practice, there may exist a range of values of individual climate variables that could generate the same vegetation, i.e. the reconstructed climate values may not be unique, and no single set of values of the climate variables can then be specified as "optimal". Consequently, the approach that has been generally used involves the generation of many thousands of candidate sets of individual climate-variable values that are individually discarded or retained depending on their ability to correctly generate the observed vegetation using a specific forward model. The retained climate-variable values (i.e., those that are

"feasible" in the sense of correctly simulating the target vegetation) are then summarized to provide the reconstructed or estimated values of the climate variables. This analysis (Fig. 4.1) can be implemented with an appropriate algorithm in a Bayesian framework (Gelman et al. 2003), i.e. using the Metropolis-Hasting algorithm (Hastings 1970; Metropolis et al. 1953) that allows a reduction of the calculation time, but the task can also be viewed as a general multi-parameter optimization problem. The following IMIFM approach follows that of Guiot et al. (2000) and Wu et al. (2007), and a series of operations (biomization, and the IMIFM approach, including new approache for implementing the analysis) were implemented with Fortran 90/95 programs.

3.1. Biomization

Paleoecological data are generally expressed in the form of abundances of individual plant taxa. However, plant functional types (PFTs) and biomes are often adopted for representing vegetation in numerical models. PFTs are defined on the basis of traits describing species life form, leaf form, phenology, and bioclimatic tolerances. These features of vegetation reflect their preferable environments that plants maximize productivity while surviving environmental stress. Biomes, which are climatically and geographically broadly distributed physiognomic vegetation types, are defined as assemblages of PFTs. The use of PFTs helps to solve the problem of classifying paleoecological records by reducing the number of entities considered and by providing an ecological basis for treating plants from different regions in a comparable way.

In order to compare observed pollen data with simulated biomes, the observed biome scores (i.e. affinity scores) for a particular fossil-pollen spectrum are calculated by the biomization method (Prentice and Webb 1998). Biomization involves assigning a fossil pollen assemblage to (one or more) biome(s) (Prentice and Webb 1998). There are five steps in the method: (1) assignment of taxa represented in the pollen assemblages to plant functional types (PFTs) (i.e., making a taxa × PFTs matrix), (2) definition of

biomes as combinations of PFTs (making a PFTs × biomes matrix), (3) combination of the above two matrices (making a taxa × biomes matrix by simple matrix multiplication of the matrices made in steps 1 and 2), (4) calculation of affinity scores of pollen assemblages from individual sites for every biome (Appendix C), and (5) selection of a biome with the highest affinity score as the dominant biome. The affinity scores of biomes are a measure of their likely presence at a site given a particular pollen spectrum, such that the lower affinity the score, less likely the biome is to be present. The score is not equivalent to the proportion of the area covered by an individual biome at the site. If more than one biome has the same score, a tie-breaking rule is adopted. There are two approaches for classification of PFTs and biomes: traditional (simple) schemes and global schemes. The global scheme (Harrison et al. 2010; Ni et al. 2010) expands the number of PFTs and biomes relative to previous applications of this approach, and thus makes the comparison of observed biomes with simulated ones more explicit. In this study, the traditional approach using different matrices for different North American regions, was adopted: The matrices were based on Williams et al. (2000a) for the eastern (east of 105°W) USA and Canada, Thompson and Anderson (2000) for western USA, and Edwards et al. (2000) for Beringia (here defined as the area west of 130°W, and from 53°N to 75°N).

3.2. BIOME4 and BIOME5 vegetation model

BIOME4 (Kaplan et al. 2003) is an equilibrium terrestrial biosphere model that simulates the geographic distribution and quantitative properties of vegetation from climate, soil physical properties, and atmospheric CO_2 concentration. BIOME5 (Izumi et al., in prep) was developed and simplified from BIOME4 for paleoclimate reconstructions. For climate input, BIOME5 adopted the updated modern climatology (CRU TS3.21; Harris et al. 2014) and was modified to include snow-moisture accounting and to use a multi-layer soil characteristic data set (IGBP-DIS). The model includes

several new PFTs to improve the representation of certain vegetation types, particularly in arid regions. The parameters of the carbon flux submodel have been modified in line with MODIS (MOD17) GPP and NPP data (Zhao et al. 2005; Zhao and Running 2010). As Guiot et al. (2009) discussed before, because iterative forward-modeling approaches are highly dependent on the quality of the process-based model, we adopt both BIOME5 and BIOME4 in order to compare the results. In this study, we adopted a BIOME5 beta version (Appendix D) that uses the two-layer soil characteristic (FAO) and the same biome assignment scheme as BIOME4 to allow a simple comparison between two models. BIOME5 beta version simulates better present plant productivities (i.e. NPP and GPP) than BIOME4 by virtue of modification of carbon flux submodel (Appendix D).

As part of the simulation of PFTs and biomes, BIOME4 and BIOME5 also calculate a set of bioclimatic variables: growing degree-days 0°C base (GDD0) and 5°C base (GDD5), mean temperature of the coldest month (MTCO), mean temperature of the warmest month (MTWA), mean annual temperature (MAT), mean total annual precipitation (MAP), and plant-available moisture index (α: the ratio of actual to equilibrium evapotranspiration in BIOME4; the ratio of actual to potential evapotranspiration in BIOME5; Appendix D). Annual-average climate moisture index (CMI; Appendix C) was calculated according to Willmott and Feddema (1992), as the ratio of annual precipitation (MAP) to annual potential evapotranspiration (PET).

3.3. Inverse modeling through iterative forward-modeling approach

At each pollen site, the IMIFM algorithm involves the following steps (Fig. 4.1): (1) Six-dimensional vectors of climate (i.e. January and July temperature and January, April, July, and October precipitation) anomalies from the baseline climatology (i.e. differences from the modern climate) are selected using a uniform random number generator within a prescribed range (Table 4.1). In the first iteration, these anomalies are referred to as “actual” parameter values. In the subsequent iterations, these values are

updated via the application of the Metropolis-Hastings algorithm that is an iterative method which browses the domain of the parameters (i.e. the potential "climate space") generating what will be referred to as "candidate" values. (2) The other monthly temperature and precipitation anomalies of the climate scenario are estimated using the empirical equations described below, and the monthly anomalies are applied to the baseline climatology in order to create "actual" (not anomaly) variable values. (3) Monthly cloudiness and absolute minimum temperature are estimated from temperature and precipitation in step 2. (4) BIOME4 or BIOME5 is run with "actual" parameter values from steps 2 and 3. (5) The simulated biomes are converted to biome scores with a transfer matrix. (6) The simulated biome scores are compared with the observed biome scores (i.e. the affinity scores from biomization) using a Euclidian-distance dissimilarity measure, and a likelihood (LH) value based on the Euclidian distance between "target" biome scores and simulated scores is calculated. (7) The current "actual" values are updated using the Metropolis-Hastings algorithm to generate "candidate" six-dimensional vectors of temperature and precipitation anomalies using a multivariate Gaussian distribution. The mean of the distribution is the previous "actual" value and the initial variance-covariance matrix is the identity matrix (a matrix with diagonal terms equal to one and off-diagonal terms equal to zero). The variance-covariance matrix is updated at this step every 100 iterations. (8) The other monthly anomalies of the climate scenario from the "candidate" values are estimated in the same way as in step 2, and the anomalies are applied to the baseline climatology. The other climate data is estimated in the same way as the step 3. (9) The biome model is run using the "candidate" parameter values. (10) The simulated biomes are converted to biome scores with the transfer matrix. (11) As in step 6, the biome scores calculated using the "candidate" climate values are compared with the observed biome scores. (12) The candidate climate vectors are accepted or rejected based on the ratio of the "candidate" LH to the "actual" (i.e. current iteration) LH comparing that ratio to the criterion C (Guiot et al. 2000). If the LH ratio is satisfied using this criterion, the candidate value becomes the "actual" values for the next

iteration; if not, we reject the candidate value and keep the current actual values. In either case, we return to step 7. In each experiment, a prescribed number of iterations (Table 4.1) were run, and we retained one iteration out of every two, because successive iterations are autocorrelated. The candidate climate vectors that are retained can be considered to be a set of "feasible" climate-variable values because they are able to correctly simulate the target vegetation at each sample site.

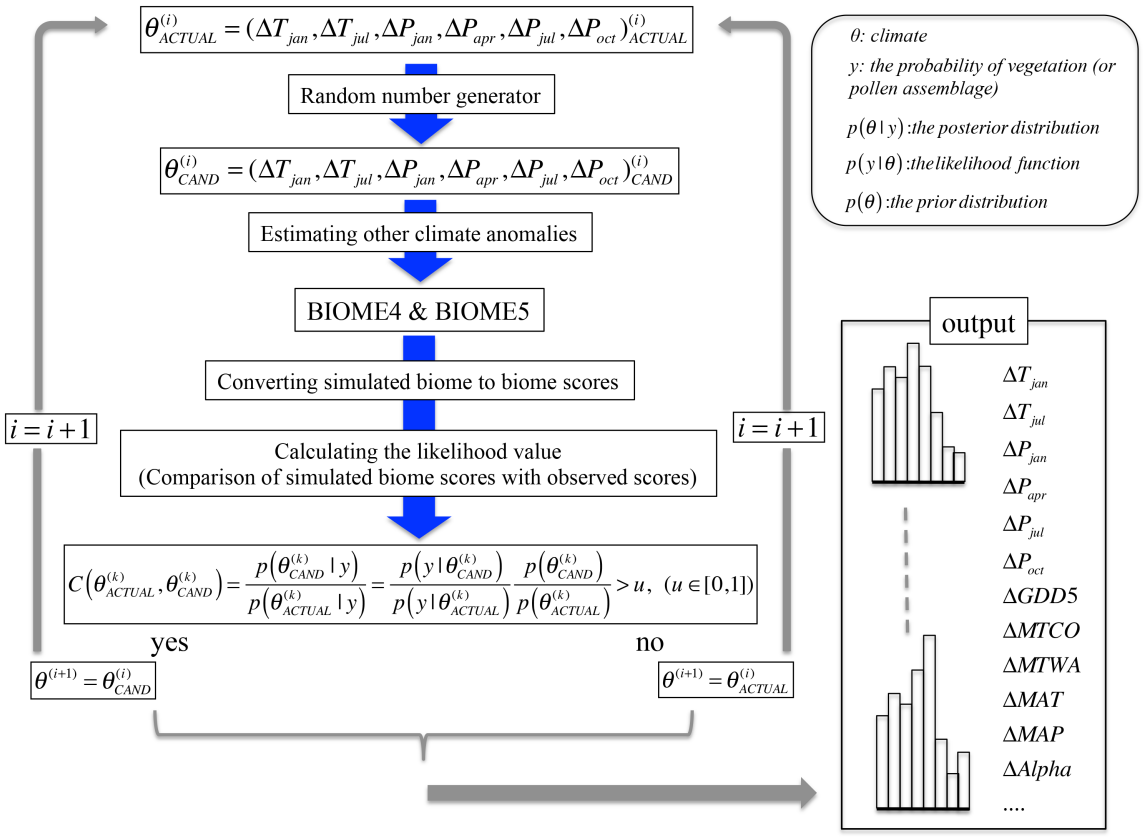

Figure 4.1. Schematic diagram of the inverse-modeling through iterative forward-modeling approach for the paleoclimate reconstruction in this study; The diagram was modified from Fig. 2 in Guiot et al. (2000).

The Metropolis-Hasting (MH) algorithm is not an optimization method for fitting a posterior joint density function, but "a method for browsing the prior definition domain of the parameter vector in order to simulate its posterior distribution" (Guiot et al. 2000).

The MH algorithm was applied with the LH function defined by A32-34 in (Wu et al. 2009) and with a multivariate uniform distribution having the range described in Table 4.1.

Table 4.1. The ranges of input parameters for simulation at modern, mid-Holocene (MH), and Last Glacial Maximum (LGM)

Parameters	Modern	MH	LGM
ΔT_{jan} ΔT_{jul}	[-10, 10] °C	[-10, 10] °C	[-30, 5] °C
ΔP_{jan}, ΔP_{apr}, ΔP_{jul}, and ΔP_{oct}	[-90, 100] %	[-90, 100] %	[-90, 50] %
CO_2	333 ppmv	280 ppmv	185 ppmv
Iterative number *	3000 × 10	4000 × 10	10000 × 10

The ranges are given in anomalies from modern values (deviation for temperature and percentages for precipitation)

* Using 10 different seeds for a uniform random number generator, we run the program with specific iterations.

Histograms of the values of the retained or "feasible" climate-variable values provide an estimate of the posterior probability distribution of the parameters (or the target climate values). In practice, the histograms are constructed using a data file (CSV format) that generally includes more than 200 feasible climate scenarios for a target biome, plus latitude, longitude, maximum LH, and simulated biome number. The latter four values do not change at each site, and we used this latitude, longitude, and simulated biome number for validating simulated biomes (see Fig. 4.2). This data file also provides the reconstructed climates for a target biome, which are obtained by summarizing the distribution described by the histogram. Both 50^{th} percentile (median) and the mode of each climatic and bioclimatic variable were calculated for exploring the optimal way of describing the reconstructed climate at each site (Fig. S4.1), and these values were used for validating modern climate (see Fig. 4.3) and making anomaly maps (see Fig. 4.4, 4.5, 4.7, and 4.8) and latitudinal zonal cross section figures (see Fig. 4.6 and 4.9). Furthermore, the 5^{th}, 25^{th}, 75^{th}, and 95^{th} percentile of each climatic and bioclimatic variable are calculated at each site for examining the feasible climate ranges of the target biome (see Fig. 4.6 and 4.9). More detailed description of the inverse process

(Metropolis-Hastings algorithm and likelihood function) is in Guiot et al. (2000) and Wu et al. (2009).

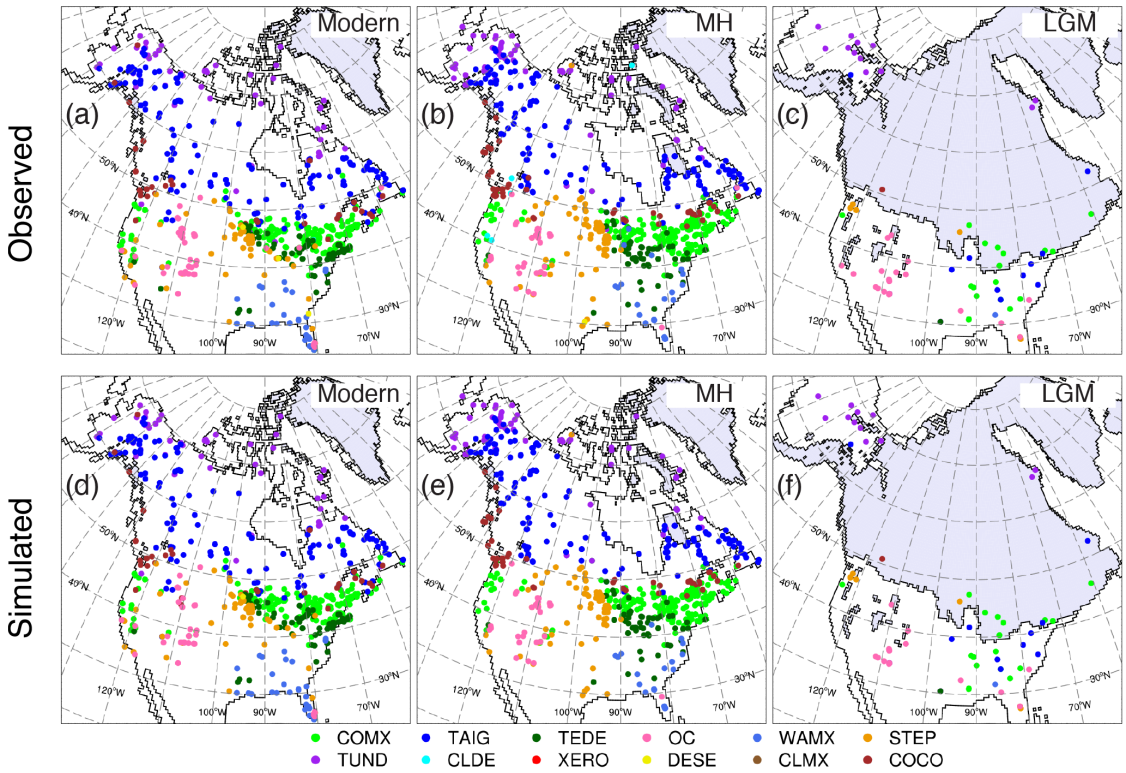

Figure 4.2. Comparison of observed and BIOME5 simulated biomes at site for modern (a and d), mid-Holocene (MH; b and e), and last glacial maximum (LGM; c and f) for North America. COMX, cool mixed forest; TAIG, taiga; TEDE, temperate deciduous forest; OC, open conifer woodland; WAMX, broadleaved evergreen/warm mixed forest; STEP, steppe; TUND, tundra; CLDE, cold deciduous forest; XERO, xerophytic woods/scrub; DESE, desert; CLMX, cold mixed forest; COCO, cool conifer forest

3.3.1. Parameter vector details

The six-dimensional vectors of climate anomalies from the baseline climatology ($\Delta T_{jan}, \Delta T_{jul}, \Delta P_{jan}, \Delta P_{apr}, \Delta P_{jul}$, and ΔP_{oct}) are selected using a uniform random number generator with prescribed ranges (Table 4.1). The parameters of interest in this study are temperature and precipitation. The other monthly temperature anomalies (ΔT) of the

climate scenario are estimated with January and July temperature anomalies using the following sine curve;

$$\Delta T_{month} = \Delta T_{jan} + \left(\Delta T_{jul} - \Delta T_{jan}\right) \times \sin\left[\pi\left(month - 1\right)/12\right]$$
where $month = 1,...,12$

The other monthly precipitation anomalies (ΔP) of the climate scenario are estimated with January, April, July, and October anomalies using following curves;

$$\Delta P_{month} = \Delta P_{jan} + \left(\Delta P_{apr} - \Delta P_{jan}\right) \times \sin\left[2\pi\left(month - 1\right)/12\right]$$
where $month = 1,...,3$

$$\Delta P_{month} = \Delta P_{apr} + \left(\Delta P_{jul} - \Delta P_{apr}\right) \times \sin\left[2\pi\left(month - 1\right)/12\right]$$
where $month = 4,...,6$

$$\Delta P_{month} = \Delta P_{jul} + \left(\Delta P_{oct} - \Delta P_{jul}\right) \times \sin\left[2\pi\left(month - 1\right)/12\right]$$
where $month = 7,...,9$

$$\Delta P_{month} = \Delta P_{oct} + \left(\Delta P_{jan} - \Delta P_{oct}\right) \times \sin\left[2\pi\left(month - 1\right)/12\right]$$
where $month = 10,...,12$

These monthly temperature and precipitation anomalies were applied to the baseline climatology.

Cloudiness was estimated from temperature and precipitation using regression (Table 4.2). Using CRU CL2.0 monthly data over the North America (here defined as the area between 170°W and 50°W, and from 20°N to 80°N), we calculate a linear relationship that predicts percent possible sunshine from temperature and precipitation. The absolute minimum temperature (T_{min}, °C) is estimated from mean monthly temperature of the coldest month (MTCO, °C). The relationship is deduced from CRU CL2.0 data over the North America; $T_{\min} = 0.863 \times MTCO - 26.98$ (R^2=0.76, $p < 0.000$).

3.3.2. Transfer matrix

Wu et al. (2007) adopted a transfer matrix where each simulated biome type is assigned a vector of values (virtually or theoretically simulated biome scores), ranging

Table 4.2**.** Regression coefficients for sunshine (dependent variable) and temperature and precipitation

Month	Intercept	Prep (P)	Temp (T)	P × T	R^2
Jan	57.82	-0.1234	1.1094	0.0005	0.68 (p<0.000)
Feb	60.88	-0.1455	0.6118	0.0071	0.59 (p<0.000)
Mar	60.72	-0.1569	0.2223	0.0110	0.51 (p<0.000)
Apr	61.99	-0.2354	0.1731	0.0133	0.46 (p<0.000)
May	53.72	-0.2081	0.8895	0.0061	0.62 (p<0.000)
Jun	44.72	-0.2287	1.4468	0.0041	0.74 (p<0.000)
Jul	42.52	-0.2497	1.4898	0.0049	0.76 (p<0.000)
Aug	34.67	-0.1427	1.9000	-0.0004	0.82 (p<0.000)
Sep	34.39	-0.1018	1.9124	-0.0021	0.74 (p<0.000)
Oct	41.83	-0.1025	1.5631	0.0001	0.71 (p<0.000)
Nov	47.45	-0.1402	1.0875	0.0057	0.73 (p<0.000)
Dec	52.12	-0.1158	1.3330	-0.0001	0.73 (p<0.000)

[a] Columns 2-5 give the regression coefficient for the corresponding month.

between 0 and 15, because there is no full compatibility between the simulated biome typology and the observed biome typology by biomization method in Eurasia and Africa.Although we also considered this kind of transfer matrix for comparing the simulated with observed biome, we adopted a simpler transfer matrix (Table 4.3). A value of 0 corresponds to an incompatibility between the simulated type and the observed type (i.e. absence of biome). A value of 1 corresponds to a maximum correspondence (i.e. presence of biome). We multiply the coefficient (0 or 1) in the transfer matrix by the observed biome affinity scores from the biomization method. The observed affinity scores are different among biomes and sites. The target observed biomes score is the highest value among the observed biome scores for a given sample site. Although more than two biomes may have the same (highest) affinity score at some sites, our transfer matrix selects only one biome, the target dominant biome. As a result, simulated biomes using the climate-variable values with maximum likelihood (LH) should be completely consistent with the observed biome.

3.4. Summarizing the output data

On the assumption that the reconstructed data will be directly comparable with climate-model output, we produced gridded data sets of the anomalies of each bioclimatic variable. We used a fixed latitude/longitude 2°×2° grid. This grid size was based on Bartlein et al. (2011), and is comparable to the grid size typical of the models used in state-of-the-art paleoclimate simulations; also, this grid size avoids over-smoothing the resulting patterns of regional climate change and limits the number of grid cell values based on a single reconstruction. The grid-cell value of the anomaly was obtained by simple area-average with a 125 km radius search window on each grid. This method enables one sample data point to influence multiple grid cells (in particular at higher latitudes).

Table 4.3. Transfer matrix from BIOME5/BIOME4 typology to the pollen biome score

Simulated	Observed biome											
biome	DESE	XERO	CLDE	TUND	WAMX	STEP	OC	TEDE	TAIG	CLMX	COCO	COMX
4	0	0	0	0	0	0	0	**1**	0	0	0	0
6	0	0	0	0	**1**	0	0	0	0	0	0	0
7	0	0	0	0	0	0	0	0	0	0	0	**1**
8	0	0	0	0	0	0	0	0	0	0	**1**	0
9	0	0	0	0	0	0	0	0	0	**1**	0	0
10	0	0	0	0	0	0	0	0	**1**	0	0	0
11	0	0	**1**	0	0	0	0	0	0	0	0	0
14	0	**1**	0	0	0	0	0	0	0	0	0	0
17	0	0	0	0	0	0	**1**	0	0	0	0	0
20	0	0	0	0	0	**1**	0	0	0	0	0	0
21	**1**	0	0	0	0	0	0	0	0	0	0	0
22	0	0	0	**1**	0	0	0	0	0	0	0	0
23	0	0	0	**1**	0	0	0	0	0	0	0	0
24	0	0	0	**1**	0	0	0	0	0	0	0	0
25	0	0	0	**1**	0	0	0	0	0	0	0	0
26	0	0	0	**1**	0	0	0	0	0	0	0	0

Simulated biome type: 4 Temperate deciduous forest; 6 Warm mixed forest; 7 Cool mixed forest, 8 Cool conifer forest; 9 Cold mixed forest; 10 Evegreen taiga/montane forest; 11 Deciduous taiga/montane forest; 14 Temperate xerophytic shrubland; 17 Open conifer woodland; 20 Temperate grassland; 21 Desert; 22 Steppe tundra; 23 Shrub tundra; 24 Dwarf shrub tundra; 25 Prostrate shrub tundra; 26 Cushion forb lichen moss tundra

Observed biome type: DESE, desert; XERO, xerophytic woods/scrub; CLDE, cold deciduous forest; TUND, tundra; WAMX, broadleaved evergreen/warm mixed forest; STEP, steppe; OC, open conifer woodland; TEDE, temperate deciduous forest; TAIG, taiga; CLMX, cold mixed forest; COCO, cool conifer forest; COMX, cool mixed forest

We compare the spatial patterns of bioclimatic variables from both BIOME4 and BIOME5. We measure the similarity of any two map patterns (e.g. bioclimatic variable from BIOME5 and BIOME4) using the weighted uncentered anomaly correlation (AC_U) which measures the similarity of two patterns without removal of the global mean, therefore assessing agreement in magnitude as well as pattern (Wilks 2011, p. 364). The AC_U correlation coefficient is bounded by ± 1.0; +1.0 indicates a perfect match in spatial pattern and magnitude between variables or between models, and -1.0 indicates a completely opposite spatial pattern between variables or between models.

4. Results

The results of the application of the IMIFM to the North American data are summarized as follows:

1) comparison of the current biomization method with previous work to test that part of the overall approach (section 4.1)
2) evaluation of the reconstruction method using modern data, comparing the reconstructed modern climate (using surface samples) with the observed climate and the simulated modern biomes with the observed biome. (section 4.2)
3) reconstruction of MH climates (4.3)
4) reconstruction of LGM climates (4.4).

4.1. Biomization results

Because we used exactly the same biomization procedure as the previous studies, we assume that the observed biome is correct for these sites. Modern surface samples, the core-top data from Neotoma, provide an opportunity to test the validity of the method used to reconstruct past biomes. Although some samples from forest biomes are misclassified into non-forest biomes, such as steppe (STEP, treeless vegetation dominated by drought-tolerant forbs, grasses, and shrubs) and desert (DESE) in eastern

USA, the biomization method captures the broad complex features in the modern vegetation and the tundra-forest boundary over North America (Fig. 4.2a). In the eastern North America, warm mixed forest (WAMX) in the southeast gives way to temperate deciduous forest (TEDE) further north, which in turn is succeeded by cool mixed forest (COMX), a thin strip of cool conifer forest (COCO), and taiga (TAIG). To the west, the steppe (STEP) of the Midwest replaces the temperate forest biomes, and is replaced further north by TAIG and tundra (TUND). COCO is assigned in the Pacific Northwest, and COMX is assigned over the coastal western USA and Sierra Nevada. Open conifer woodland (OC) is assigned to sites along the Rocky Mountains and at the north-east limit of the STEP.

Our mid-Holocene (MH) biome distribution (Fig. 4.2b) is similar to the modern distribution, but steppe expands in the continental interior. The border between boreal and temperate forests slightly shifts to the north. At the Last Glacial Maximum (LGM), eastern North American forest biomes were displaced southward, open conifer woodland (OC) expanded in southern North America, and steppe was present in much of the regions now covered by forests in the Pacific Northwest (Fig. 4.2c). Most of our results are consistent with previous studies, and the individual papers were consulted for detailed modern and past biome patterns in each region (Edwards et al. 2000; Thompson and Anderson 2000; Williams et al. 2000a). However, there is large difference between our result and the previous study over the coastal western USA; our result is cool mixed forest (COMX), and Thompson and Anderson (2000) was cool conifer forest (COCO). The presence or absence of the plant functional type temperate summergreen (ts) separates biome for COMX from and COCO in the biomization process.

Because the modern- and paleo-biomes from the North American biomization method using Neotoma data are similar to previous studies, our reconstructed biomes appear adequate for this study. However, the biomization with western USA data could probably be improved.

4.2. Validation of the IMIFM method with modern data

To evaluate the accuracy of our IMIFM approach, we compare observed and simulated biomes (based on estimated climate values) for the modern pollen sites (Fig. 4.2a and 4.2d). In contrast to Wu et al. (2007), our simulated biome with the maximum likelihood (LH) should be completely consistent with observed biome because of the way our transfer matrix scheme was applied. There are no systematically regional errors between observed and simulated biomes. In total, biomes at 96% (746/777) of the sites are correctly simulated and more than 200 climate scenarios for each target biome are provided with both BIOME5 and BIOME4 (Fig. S4.2). For the other 4 % of the sites, the climate scenarios for the target vegetation are not sufficient for simulating the observed biomes because the modern climatology is completely out of a favorable condition to the pollen-based biome which could result from the vegetation being overly influenced by human or/and because local climate (at sample sites) is not adequately represented from baseline climatology dataset (i.e. CRU CL 2.0).

We also examined the statistical correlations between observed and estimated climate variables at the sample sites where biomes are correctly simulated (Fig. 4.3) and these residual maps (Fig. 4.4). Although we use both the median and mode of each simulated climatic and bioclimatic variable for the statistical correlations, the median values are more highly correlated with the observed values, in particular for monthly precipitation, because the individual climate variables are not always normally distributed (or at least symmetric), making the mode a less good summarization of a distribution. Therefore, we show the median values as the estimated value for the climate scenarios. Estimated climates (anomalies applied to baseline climatology (or long-term means)) were compared with observed climate (i.e. CRU CL 2.0). If the estimated climate anomalies are zero, simulated climates are completely consistent with observed climate (i.e. an intercept of 0 and slope of 1). The slope is slightly biased for monthly mean

precipitation (January, April, and July), mean temperature of the coldest month (MTCO), and plant-available moisture index (α). The bias on the intercepts shows a tendency to slightly overestimate growing degree-days above 0°C and 5°C (GDD0 and GDD5), mean annual temperature (MAT), mean annual precipitation (MAP), α, and climate moisture index (CMI) and October precipitation and to slightly underestimate the other variables. The correlations between the observed and estimated climate are very high (0.82 to 0.97), and are comparable with those for other reconstruction approaches (Bartlein et al., 2011). The intercept and slope regression coefficients between observed and simulated values are similar for both BIOME5 and BIOME4 (Fig. S4.3). Moreover, maps of the z-scores of residuals show no major patterns among temperature, precipitation, and moisture residuals (Fig. 4.4).

4.3. Climate changes at the mid-Holocene

For the mid-Holocene (MH; 6 ka), the biomes at 97% (766/786 in BIOME5; 765/786 in BIOME4) of the sites are correctly simulated by the reconstructed climate variables using either BIOME5 (Fig. 4.2e) or BIOME4 (Fig. S4.2). The reconstructions are presented as maps of optimal (median) climatic anomalies from modern climatology on the regular 2°×2° latitude/longitude grid (Fig. 4.5 and 4.6), and zonal-mean latitudinal cross section (Fig. 4.7). In order to remove the bias from our IMIFM approach, we did bias correction;

$$\underset{\substack{[\text{bias corrected}\\ \text{reconstructed}]}}{\text{MH clim}} = \left(\underset{[\text{reconstructed}]}{\text{MH clim}} - \text{baseline clim}\right) - \left(\underset{[\text{reconstructed}]}{\text{Modern clim}} - \text{baseline clim}\right)$$
$$= \underset{[\text{reconstructed}]}{\text{MH clim}} - \underset{[\text{reconstructed}]}{\text{Modern clim}}$$

The 6 ka growing degree-days base 0°C and 5°C (GDD0 and GDD5) reconstructions (Fig. 4.5a, b) show large and spatially coherent differences from present, and the area-average anomalies over North America are about +40 degree-days with BIOME5 (and +3 degree-days with BIOME4). The anomalies for western North America

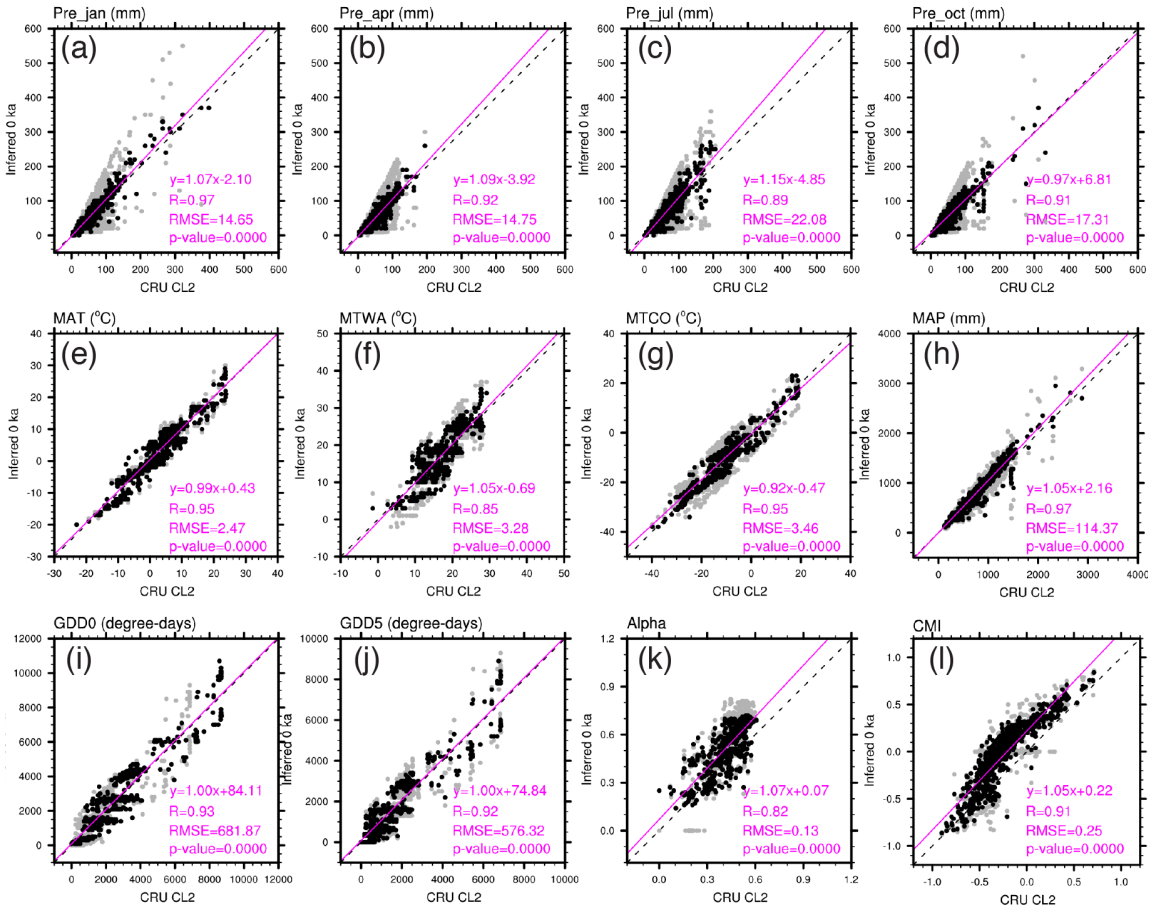

Figure 4.3. Correlation for each North American sample site between modern observed climates and IMIFM simulated climate values using BIOME5: a) January precipitation b) April precipitation, c) July precipitation, d) October precipitation, e) mean annual temperature (MAT), f) mean temperature warmest month (MTWA), g) mean temperature coldest month (MTCO), h) mean annual precipitation (MAP), i) growing degree-days base 0°C (GDD0), j) growing degree-days base 5°C (GDD5), k) plant-available moisture index (Alpha), and l) climatic moisture index (CMI). The gray dots are the mode and the black dots are the median values for each sample site. The dashed line is the 1:1 line, and the solid magenta line is the least-squares regression. R is correlation coefficient, and RMSE is the root mean square error of the residuals.

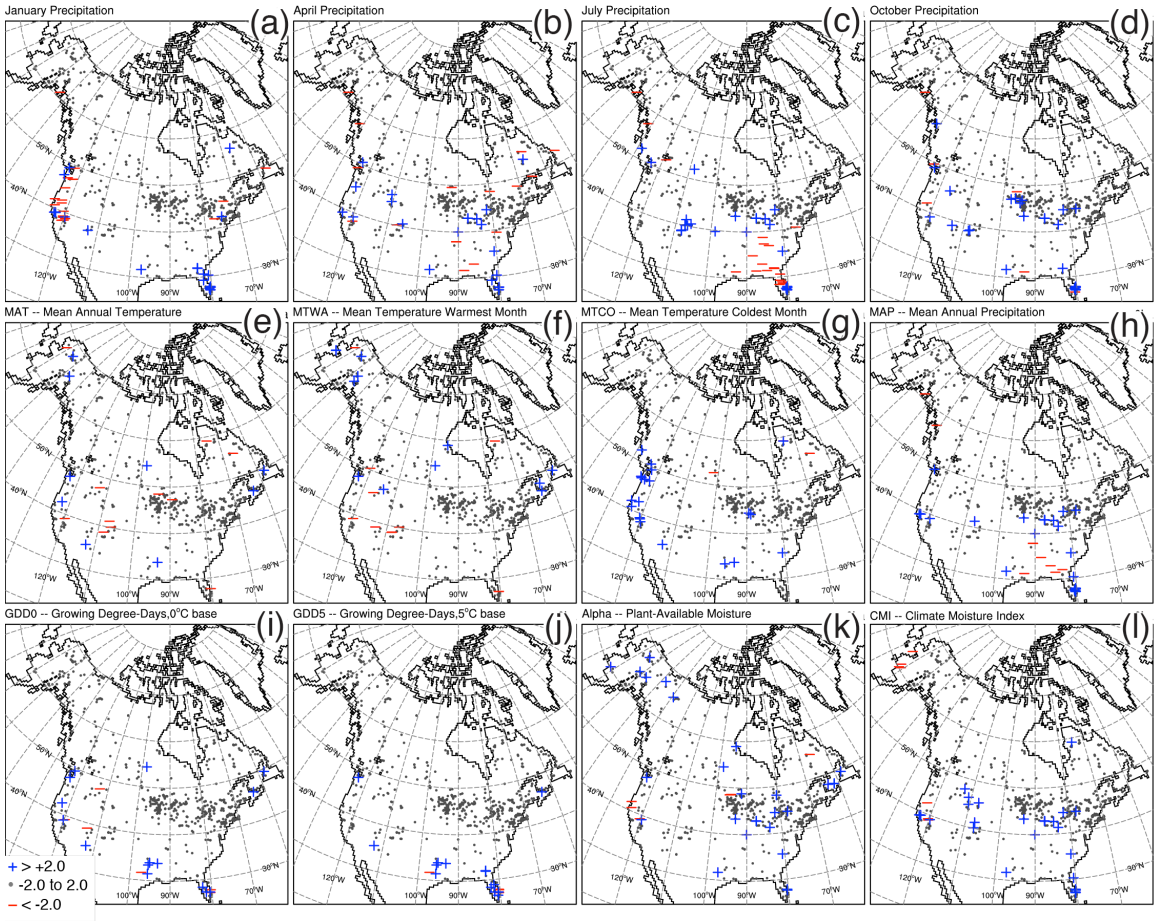

Figure 4.4. Maps of the z-scores of residuals for each North American sample site (i.e. standardized differences between modern observed climates and IMIFM simulated climate values using BIOME5); a) January precipitation b) April precipitation, c) July precipitation, d) October precipitation, e) mean annual temperature (MAT), f) mean temperature warmest month (MTWA), g) mean temperature coldest month (MTCO), h) mean annual precipitation (MAP), i) growing degree-days base 0°C (GDD0), j) growing degree-days base 5°C (GDD5), k) plant-available moisture index (Alpha), and l) climatic moisture index (CMI).

(west of 105°W) are larger than those for eastern North America. There is very high positive spatial correlation (> 0.98) between GDD0 and GDD5 in BIOME5 and BIOME4. The north central and eastern parts of North America (in particular the zone between 45°- 55°N) is characterized by positive anomalies in GDD0 and GDD5, as is the

case for coastal western USA, and northeastern Canada (the zone between 60°- 70°N). In contrast, southeastern North America (the zone between 30°- 45°N), the northern Pacific Northwest, and Alaska are characterized by a reduction in GDD0 and GDD5 compared to present (Fig. 4.7i, j). The range of zonal mean average GDDs at lower latitudes is wider than the range at higher latitudes (Fig. 4.7i, j).

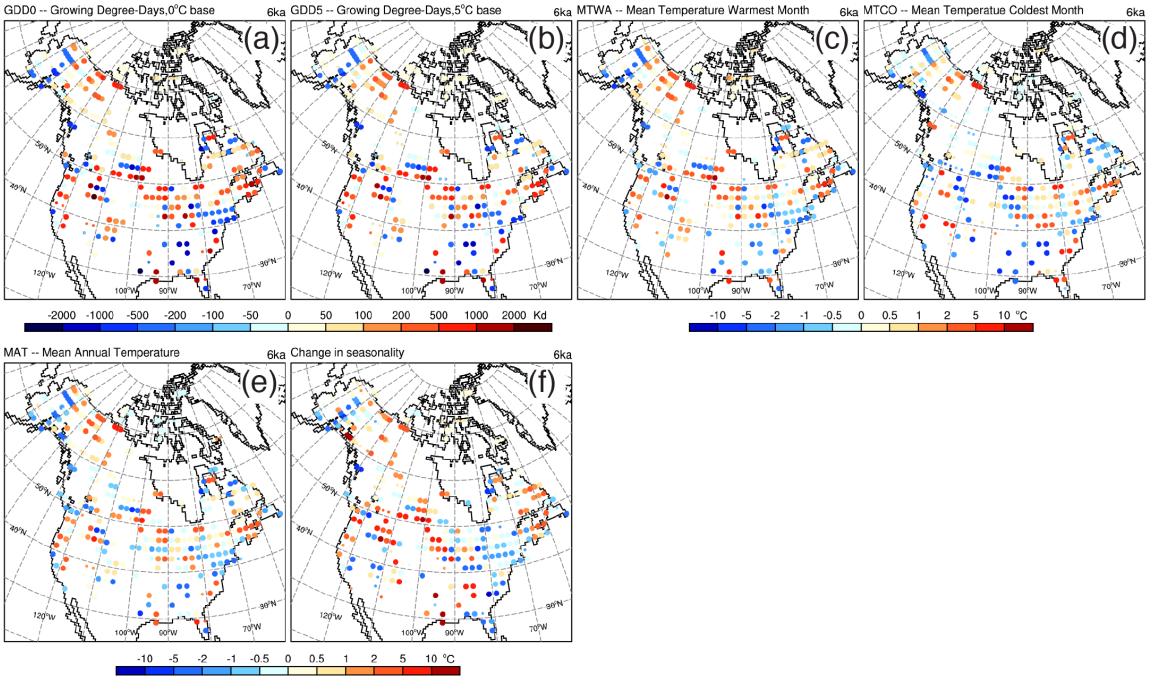

Figure 4.5. Reconstruction of temperature anomalies by BIOME5 at mid-Holocene from present: a) growing degree-days above 0°C (GDD0), b) growing degree-days above 5°C (GDD5), c) mean temperature warmest month (MTWA), d) mean temperature coldest month (MTCO), e) mean annual temperature (MAT), and f) the change in temperature seasonality (ΔMTWA - ΔMTCO). Large dots are used to indicate grid points with consistent responses between BIOME4 and BIOME5 while small dots are used to indicate anomalies that are not consistent responses between BIOME4 and BIOME5.

Growing degree-days (i.e. GDD0 and GDD5) are partially determined by changes in summer temperatures and by changes in the length of the growing season. Thus, the 6 ka mean temperature of the warmest month (MTWA) reconstruction (Fig. 4.5c; Fig. 4.7f)

shows a similar anomaly pattern as both GDDs (the spatial correlation between MTWA and GDDs is 0.87 with BIOME5). The feasible range of MTWA zonal mean in both low- and high-latitudes is wider than in the middle latitudes (Fig. 4.7f). The 6 ka mean temperature of the coldest month (MTCO; Fig. 4.5g) in North America shows positive anomalies in the northeastern and southwestern part of the continent and negative anomalies in the northwestern and south central regions (Fig. 4.5d). In contrast to the general regional pattern, however, some sites around Newfoundland and Labrador show a reduction in MTCO compared to present climate (Fig. 4.5d). There is low spatial correlation between MTCO and GDDs (> 0.5), and North American area-average MTCO is -0.2°C with BIOME5 (0.1°C with BIOME4). The potential range of MTCO is very large at all of the latitudes (Fig. 4.7g).

The change in growing season conditions (i.e. GDD0 and GDD5) is the strongest influence on reconstructed changes in mean annual temperature (MAT, Fig. 4.5e; spatial correlation is 0.93 between MAT and GDD0; 0.89 between MAT and GDD5). North American area-average MAT is 0.1°C with BIOME5 (0°C with BIOME4). The potential range of MAT zonal mean in both low- and high-latitudes is wider than one in middle latitude (Fig. 4.7e). While the largest changes in MAT occur where the changes in summer and winter temperatures are in the same direction, the largest changes in seasonality occur where changes in summer and winter temperature are in the opposite directions (Fig. 4.5f). There are high spatial correlations among GDD0, GDD5, MAT, and MTWA, but not MTCO.

There is no coherent large-scale pattern for seasonal precipitation (Fig. 4.6a-d), and the range of potential precipitation changes depends on the baseline climatology (Fig. 4.7a-d; Fig. S4.4). In other words, the locations that have high monthly precipitation also have more variable reconstructed precipitation values (e.g. Pacific Northwest during the fall and winter). There are not high spatial correlations among the monthly mean precipitation values (-0.1 ~ 0.46), but there is high spatial correlation (0.84 with

BIOME5; 0.90 with BIOME4) between mean annual precipitation (MAP) and July precipitation. There is no coherent large-scale pattern for MAP (Fig. 4.6e), and area-average anomalies of North American MAP are +9 mm with BIOME5 (+17 mm with BIOME4). There is relatively high positive spatial correlation, 0.78 between MAP and alpha, and 0.8 between MAP and CMI, but there is not high spatial correlation (0.5) between alpha and CMI. There are relatively high negative spatial correlation (-0.64 ~ -0.61) between CMI and some thermal bioclimatic variables such as MTWA, GDD0, and GDD5.

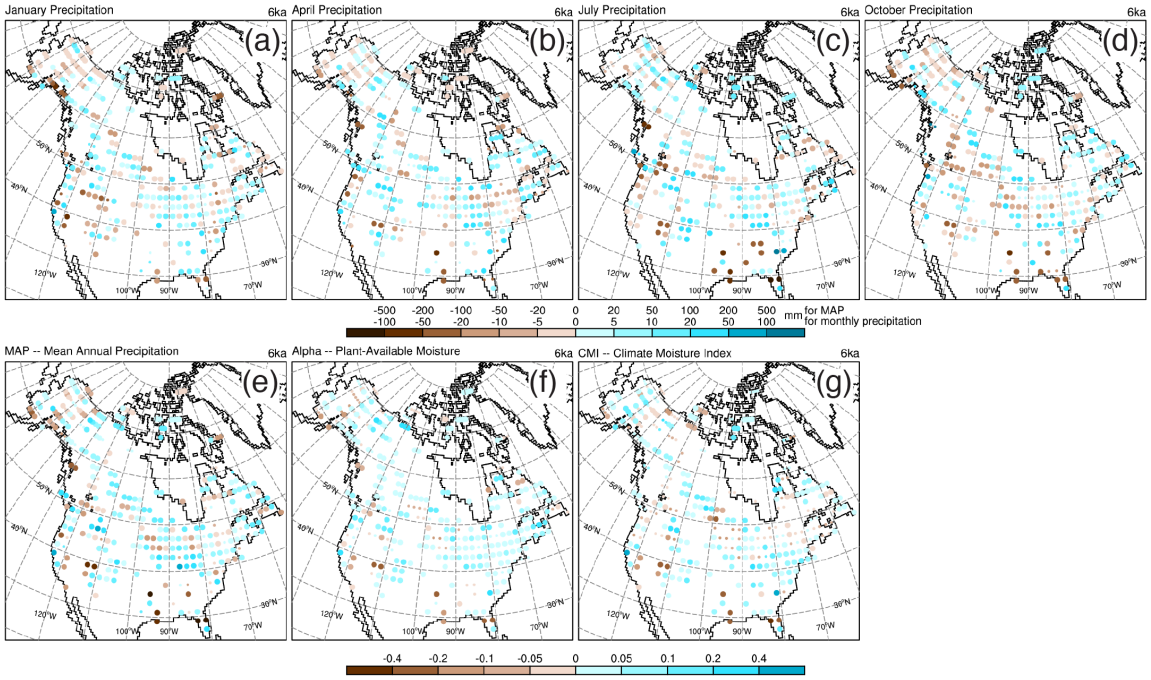

Figure 4.6. Reconstruction of hydrological anomalies by BIOME5 at mid-Holocene from present: a) January precipitation, b) April precipitation, c) July precipitation, d) October precipitation, e) mean annual precipitation (MAP), f) plant-available moisture index (α), and g) climate moisture index (CMI). Large dots are used to indicate grid points with consistent responses between BIOME4 and BIOME5 while small dots are used to indicate anomalies that are not consistent responses between BIOME4 and BIOME5.

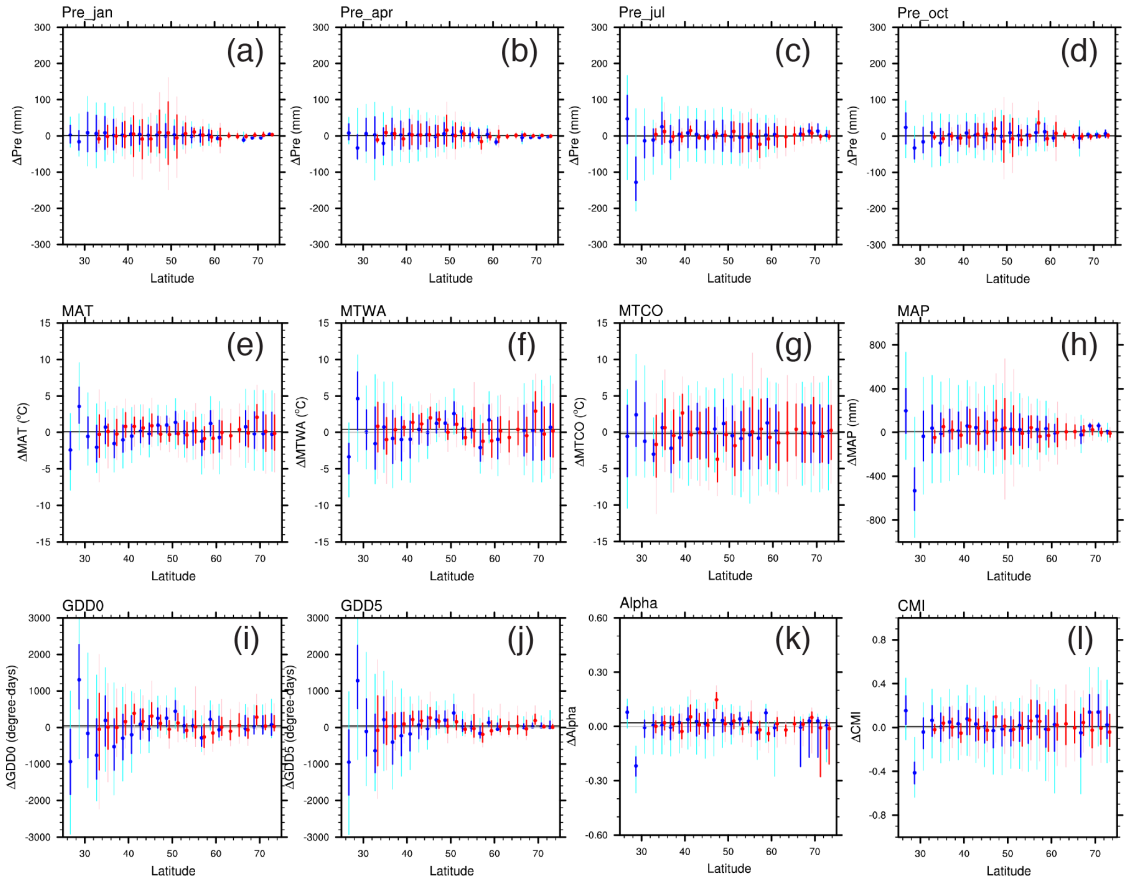

Figure 4.7. Latitudinal cross section of IMIFM simulated MH climate values using BIOME5: a) January precipitation, b) April precipitation, c) July precipitation, d) October precipitation, e) mean annual temperature, f) mean temperature warmest month, g) mean temperature coldest month, h) mean annual precipitation, i) growing degree-days 0°C base, j) growing degree-days 5°C base, k) alpha (the ratio of actual to potential evapotranspiration), and l) climate moisture index (the ratio annual precipitation to annual potential evapotranspiration).Blue represents sites of North America east of 105°W, and red for west of 105°W. The thin line extends to the 5th and 95th percentiles of reconstructed values, the bold line extends to the 25th and 75th percentiles interquartile intervals, and the dot indicates the median value. The black line shows the North American area-average value.

4.4. Climate changes at the last glacial maximum

For the last glacial maximum (LGM; 21 ka), biomes at 92% (73/79) of sites are correctly simulated and the sufficient climate scenarios for target biome are provided

with BIOME5 (Fig. 4.2f) and 94% (74/79) with BIOME4 (Fig. S4.2). The reconstructions are presented as maps of optimal (median) climatic anomalies from the modern climatology (Fig. 4.8 and 4.9) and zonal-mean latitudinal cross section (Fig. 4.10) with the same bias correction as for the MH on the regular latitude/longitude grid of 2° by 2°;

$$\underset{\substack{[\text{bias corrected}\\ \text{reconstructed}]}}{\text{LGM clim}} = \left(\underset{[\text{reconstructed}]}{\text{LGM clim}} - \text{baseline clim}\right) - \left(\underset{[\text{reconstructed}]}{\text{modern clim}} - \text{baseline clim}\right)$$

$$= \underset{[\text{reconstructed}]}{\text{LGM clim}} - \underset{[\text{reconstructed}]}{\text{modern clim}}$$

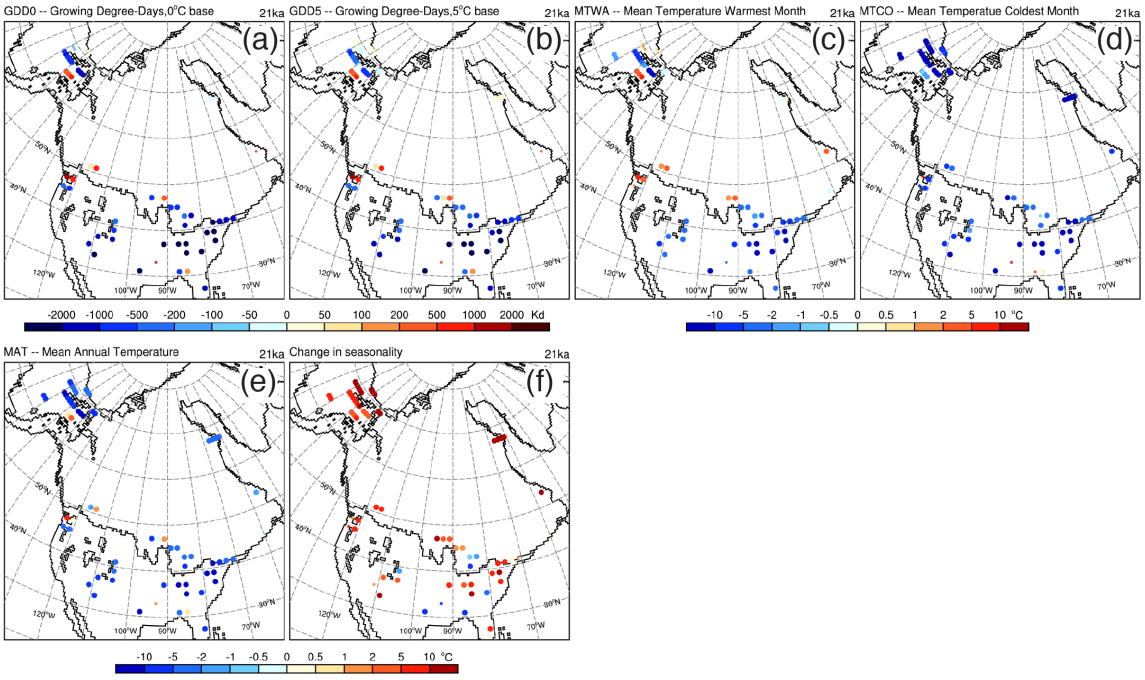

Figure 4.8. Reconstruction of temperature anomalies by BIOME5 at LGM from present: a) growing degree-days base 0°C (GDD0), b) growing degree-days base 5°C (GDD5), c) mean temperature of the warmest month (MTWA), d) mean temperature of the coldest month (MTCO), e) mean annual temperature (MAT), and f) the change in temperature seasonality (ΔMTWA - ΔMTCO). Large dots are used to indicate grid points with consistent responses between BIOME4 and BIOME5 while small dots are used to indicate anomalies that are not consistent responses between BIOME4 and BIOME5.

The MTWA reconstruction has high positive spatial correlation with both GDD0 and GDD5 (> 0.9), and MTWA values over the Pacific Northwest and Alaska are between 2 and 6°C warmer than today (Fig. 4.8c). The area-average for North American MTWA anomaly is -3.8°C with BIOME5 (-4.8°C with BIOME4), and the area-average for eastern North America MTWA anomaly is -5.2°C with BIOME5 (-6.1 with BIOME4). The range of MTWA zonal means in both low- and high-latitudes is wider than in the middle latitude (Fig. 4.10f). MTCO reconstructions (Fig. 4.8d) have relatively high positive spatial correlation with both GDD0 and GDD5 (> 0.73), and the area-average anomaly for North America MTCO is -8.8°C with BIOME5 (-8.0°C with BIOME4). In a word, temperature decreases in winter were larger than summer ones. As a result, seasonality was greater than present over most of the North America but less than present in the southeastern USA (Fig. 4.8f). MAT reconstructions have similar patterns and also have high positive spatial pattern correlation between the other temperature-related variables (> 0.9). The area-average North American MAT anomaly is -5.6°C with BIOME5 (-6.1°C with BIOME4).

During the LGM, the weakened hydrological cycle in cooler climates (Li et al. 2013) led to reduced precipitation relative to present. The seasonal precipitation and MAP reconstructions (Fig. 4.9) show a significant decrease in precipitation over the Pacific Northwest and eastern North America, but a small increase over the south-western/central USA, especially during the summer season. There is relatively high positive spatial correlation (≈ 0.8) among the precipitation and moisture reconstructions. The North American area-average MAP anomaly is -195 mm with BIOME5 (-191 mm with BIOME4). The reduction in precipitation should be translated into reduction in plant-available moisture (α; Fig. 4.9f) and climate moisture index values (CMI; Fig. 4.9g), but the spatial pattern correlations between MAP and α (0.66) and CMI (0.59) are not that high. There is no consistent pattern for α between BIOME5 and BIOME4. BIOME5 shows that α decreases over the Pacific Northwest, Alaska, and eastern North

America, and increases over the south-western/-central USA (Fig. 4.9f; Fig. 4.10k). The climate moisture index (CMI; Fig. 4.8g) shows wetter-than-present conditions over eastern North America and drier-than-present over the southeastern USA, and in particular over the Pacific Northwest. Overall, the two moisture indices show large differences in their responses because the CMI I used here is not appropriate to show the anomalies (Appendix C).

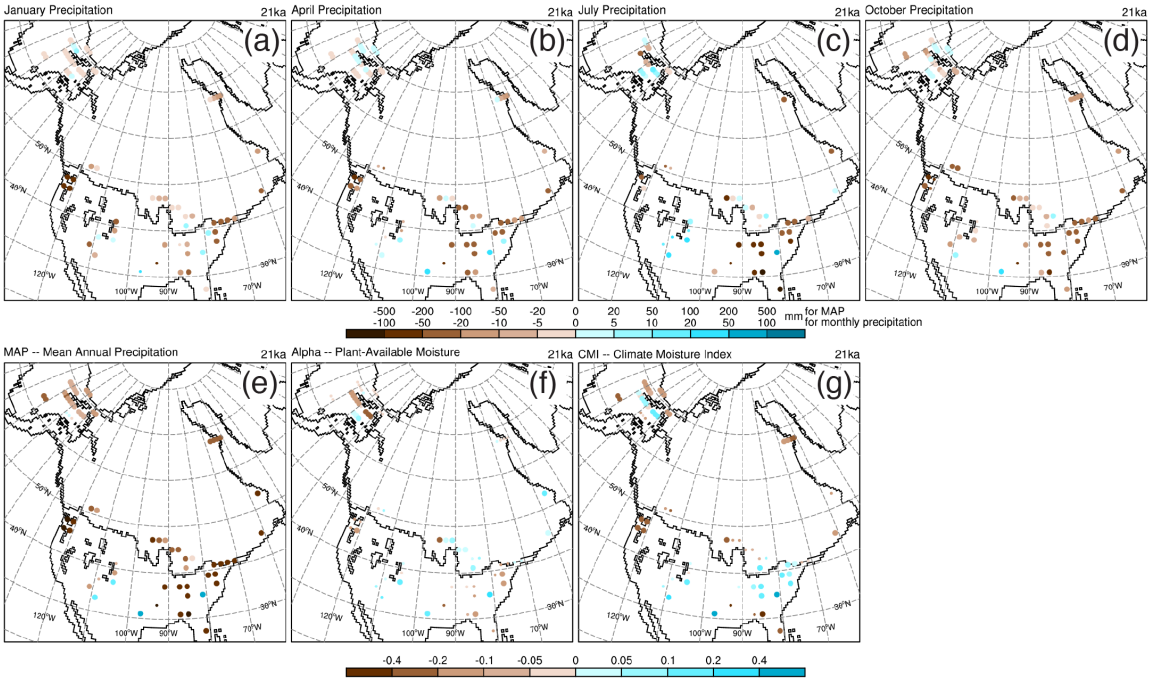

Figure 4.9. Reconstruction of hydrological anomalies by BIOME5 at LGM from present: a) January precipitation, b) April precipitation, c) July precipitation, d) October precipitation, e) mean annual precipitation (MAP), f) plant-available moisture index (α), and g) climate moisture index (CMI). Large dots are used to indicate grid points with consistent responses between BIOME4 and BIOME5 while small dots are used to indicate anomalies that are not consistent responses between BIOME4 and BIOME5.

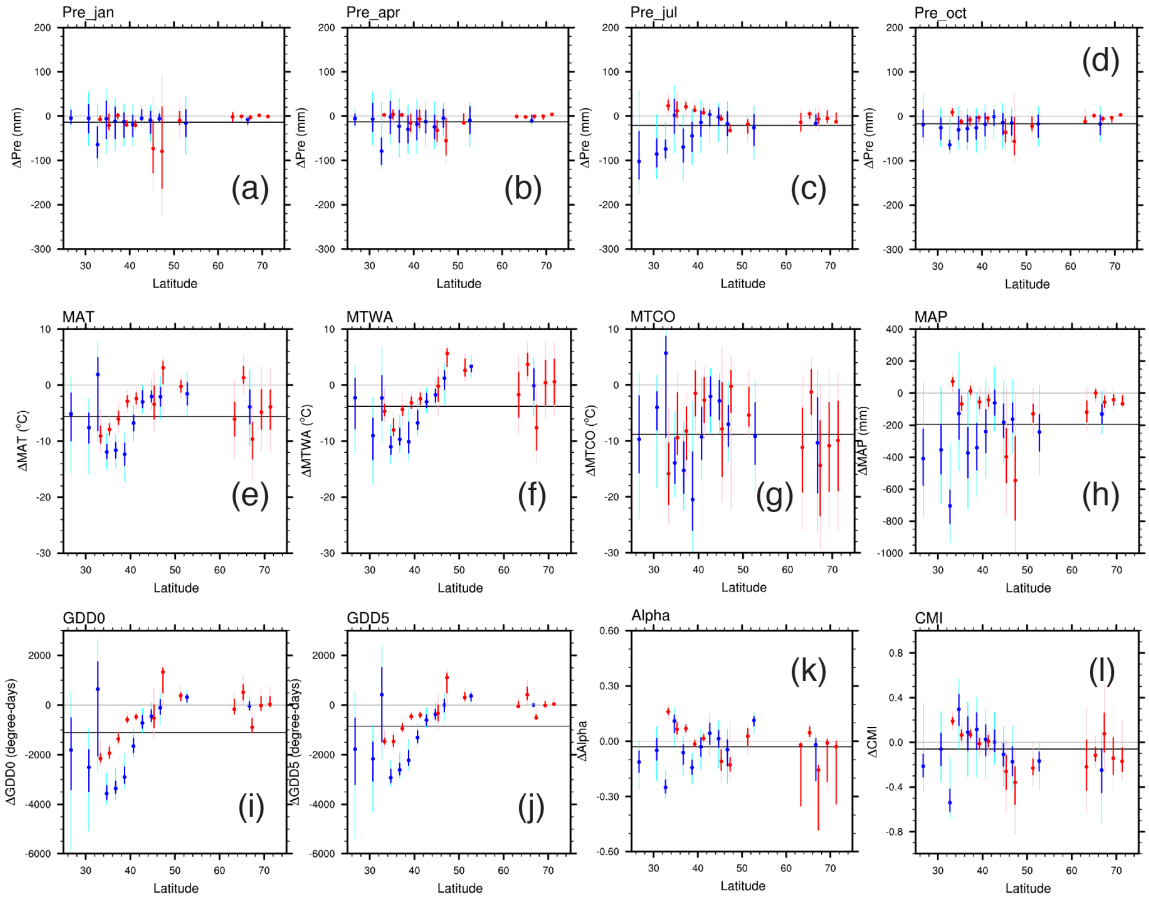

Figure 4.10. Latitudinal cross section of IMIFM simulated LGM climate values using BIOME5: a) January precipitation, b) April precipitation, c) July precipitation, d) October precipitation, e) mean annual temperature, f) mean temperature warmest month, g) mean temperature coldest month, h) mean annual precipitation, i) growing degree-days 0°C base, j) growing degree-days 5°C base, k) alpha (the ratio of actual to potential evapotranspiration), and l) climate moisture index (the ratio annual precipitation to annual potential evapotranspiration). Blue represents sites in North America east of 105°W, and red represents sites in west of 105°W. The thin line extends to the 5th and 95th percentiles of reconstructed values, the bold line extends to the 25th and 75th percentiles interquartile intervals, and the dot indicates the median value. The black line shows the North American area-average value.

5. Discussion and conclusion

Multiple studies have reconstructed North American paleoclimates using modern analogue and response surface methods, and furthermore the data synthesis of these pollen-based North American climate reconstructions (Bartlein et al. 2011) already exists. Although these two methods are conceptually simple, the application requires some assumptions and decisions that affect the paleoclimate reconstruction. The threshold value of the squared chord distance that distinguishes a good analog from a no-analog in a fossil pollen sample, the number of pollen taxa used to calculate the squared chord distance, and the number of analogues averaged to compute the fossil paleoclimate estimate tend to be subjectively decided (e.g. Jackson and Williams 2004; Viau et al. 2006). Furthermore, these approaches have the potential to cause a "wrong analog" problem (Jackson and Williams 2004), and these techniques are likely to have biased results for CO_2 concentrations unlike modern condition (e.g. Bartlein et al. 2011; Guiot et al. 2009). Therefore, we reconstructed North American paleoclimate by IMIFM approach. By adopting a process-based model in the approach, we expect to avoid both no-analog and wrong analog problems and bias (potentially) resulting from varying atmospheric CO_2 concentrations. Because the results from IMIFM approach strongly depend on the process-based model used, we employed two different models (BIOME4 and BIOME5 (beta)) in this study.

The directions of changes in our climate reconstruction at the MH are generally in good agreement with a previous synthesis of existing reconstructions (Bartlein et al. 2011). The large-scale (North America (NA), western NA, and eastern NA) bioclimatic variables area-average from Bartlein et al. (2011) is in the interquartile range of our MH reconstructions. The changes in individual variables are mutually consistent with one another, and generally spatially coherent, particularly temperature-related variables. Also, the reconstructed changes are physically plausible and can be explained in terms of current understanding of the hierarchy of controls on regional climates. Steppe (STEP)

expands in the continental interior because of increases in the growing degree-days and summer temperature and decreases in winter temperature at the mid-Holocene (MH). In a word, change in temperature seasonality results in the expansion of STEP in this region. Although some previous studies (Bartlein et al. 2011; Williams et al. 2000a) suggested that drier-than-present conditions support the expansion of STEP, our results do not show such patterns. Williams et al. (2000a) suggest that the border between boreal and temperate forest slightly shifts to north at the MH. Our result shows that temperature at the border increases through the year, and is consistent with Bartlein et al. (2011). The dominant cause of changes in regional temperature/climate at the MH is the changes in latitudinal and seasonal distribution of insolation; insolation was higher in summer and lower in winter over the northern hemisphere. In the case that the influences of insolation are inconsistent with the response of temperature, we can deduce other factors, such as changes in atmospheric circulation, must have an impact on the regional climate.

The direction of changes in our climate reconstruction at the LGM is similar to previous data synthesis (Bartlein et al. 2011), but the amplitude of climate changes are a little different in particular for eastern North America; while our reconstruction of temperature related bioclimatic variables (-6.2°C in MAT, -5.2°C in MTWA, -8.5°C in MTCO, and -1275 degree-days in GDD5 from BIOME5) is warmer than the data synthesis (-11.1°C in MAT, -10.3°C in MTWA, -15.5°C in MTCO, and -2290 degree-days in GDD5), and these data synthesis values are not in the interquartile range of our reconstructions. On the other hand, our moisture-related variables (i.e MAP and α with BIOME5) capture similar large-scale spatial pattern (drier in the Pacific Northwest and eastern North America and wetter in central North America) and their amplitude is similar as well. Our result with BIOME4 does not show the α trend. There is not a consistent spatial pattern between MAP and CMI over eastern North America (the more MAP the less CMI; Fig. 4.9e, g,).

The data presented here are a resource for paleo data-model comparison, in particular for PMIP3/CMIP5 paleoclimate simulations. Therefore, comparisons should focus on the large-scale spatial patterns that are significant, robust, and climatologically interpretable. In contrast, the experiments/investigations for the impact of CO_2 on the reconstruction should be done at each sample site because each biome/plant has the potential of different responses to changes in atmospheric CO_2 level (i.e. stomatal conductance usually changes as atmospheric CO_2 concentration varies). Thus, CO_2 effect might be more important for moisture (e.g. water use efficiency) than temperature.

The biomization approach is one of the key processes in the IMIFM approach because climate reconstructions are based on the pollen-based biome. The wrong/false biome reconstruction naturally leads to a wrong/false climate reconstruction. Moreover, the number of biomes to use potentially produces the following issues: too few biomes reduces the resolution in reconstructed climate, but too many biomes increase uncertainties. The affinity score is the dominant method of biomization, but the pollen threshold for calculating affinity scores is opaque, and must be tuned. While it increases the amount of subjectively, it becomes the key filter of noise for the biomization method (Williams et al. 1998; Williams et al. 2000a).

The biomization method has two approaches for classification of PFTs and biomes: traditional (simple schemes) and global schemes. The global scheme (Harrison et al. 2010; Ni et al. 2010) expands the number of PFTs and biomes relative to previous application of this approach (based on BIOME; Prentice et al. 1992), and thus makes the comparison of observed biomes with simulated ones more explicit. The expanded (global scheme) biome types are more consistent with BIOME4 and BIOME5 (beta) biomes (e.g. five different tundra types). Most of the biomes in BIOME4 and BIOME5 (beta) potentially allow for direct comparison with tropical forest to tundra biomes in China (Ni et al. 2010). Therefore, in adopting a forward-modeling approach using BIOME4 and BIOME5 (beta) for data-model comparison, we probably should use the global scheme

biomization method. However, we adopted the traditional approach of biomization in North America because the global scheme biomization using North American pollen data is not established yet.

Biomization in Western North America (Thompson and Anderson 2000) was treated separately from biomization in Canada and the eastern United States (Williams et al. 2000a) because of (1) strong geographical and elevational gradients in both temperature and precipitation and (2) an endemic flora. Moreover, while the standard biomization method uses a fixed (0.5%) pollen threshold (Edwards et al. 2000; Thompson and Anderson 2000) for consistency among regions and to reduce the amount of subjectivity in the method, (Williams et al. 2000a) selectively raised pollen thresholds for Canada and the eastern United States because of the improved biome reconstructions. The ideal reconstruction to use for paleo data-model comparison is the continental or global scale paleoclimate reconstructions based on a uniform method (i.e. global scheme of biomization). We need a standardized framework for the global scheme to reduce the impact of subjectivity in biomization studies in different regions, but there are several unanswered questions currently: how many species, PFTs, and biomes should we consider for matrices? What pollen threshold do we use for calculating affinity scores?

CHAPTER V

SUMMARY

Paleo data-model comparison enables us 1) to understand both the paleoclimate mechanisms and the responses of the Earth systems to climate and 2) to evaluate how state-of-the-art climate models work. With a focus on the first of these points this dissertation described the development and application of approaches for paleo data-model comparison. This study increases the scientific understanding of paleoclimatic changes/variations, and furthermore contributes to future climate projects. The main objectives of the dissertation and the key findings from each chapter are summarized below.

- Compare modern and paleoenvironmental data syntheses with simulations performed in CMIP5 and discuss the consistent simulation of large-scale temperature responses cross the climate states (chapter II).
- Examine the common mechanisms that control the large-scale temperature responses in warm and cold climates using a simple energy-balance model (chapter III)
- Estimate climates changes over North America at the last glacial maximum and mid-Holocene using the inverse-modeling through iterative forward-modeling (IMIFM) approach (chapter IV)

Chapter II: Consistent Large-scale Temperature Responses in Warm and Cold Climate

This chapter focused on paleo-data model comparison for understanding large-scale temperature responses (i.e. land-ocean contrast, high-latitude amplification, and seasonality changes) in both warm and cold climates. CMIP5 climate models simulated the proportional, generally linear temperature responses across the climate states

(including modern and past simulations); these robust patterns appear in all models and all times, and stronger contrast and amplification happen in winter season and then they reflect temperature seasonality. Moreover, the large-scale temperature patterns appear in historical observations and paleoclimate reconstructions. Therefore, althrough the paleo data-model comparison, these simulated temperature responses are characteristic features of real climate system, and not simple model artifact. With regard to the large-scale temperature responses, our results increase the confidence in the ability of climate model to correctly simulate different climates

Chapter III: Energy-balance Mechanisms Underlying Consistent Large-scale Temperature Responses in Warm and Cold Climates

This chapter focused on the investigation of the key controls of the consistent large-scale temperature responses in both warm and cold, and it was a continuous study with chapter II. We adopted a simple energy-balance model (5 radiative components and 3 non-radiative components) to examine the possibility that a small set of common mechanisms controls the large-scale temperature responses in CMIP5 *lgm* and *abrupt4×CO_2* simulations. According to latitudes and surface types, several components are involved in the different and some components show the robust patterns across the models. The clear-sky longwave downward radiation is the key control for both land-ocean contrast and high-latitude amplification in both warm and cold climates. The clear-sky longwave downward radiation includes the effect of changes in CO_2, water vapor, and atmospheric energy transport. The land-ocean contrast and high-latitude amplification result in the seasonality changes rather than an independent temperature response.

Chapter IV: The iterative forward-modeling approach for paleoclimatic reconstruction: Climate changes over North America at the mid-Holocene and Last Glacial Maximum

One approach for reconstructing past climate variations is "inverse modeling through iterative forward-modeling" (IMIFM) in which a forward model (e.g. an equilibrium vegetation model) is applied to large number of climate-variable values to determine those that likely gave rise to a particular paleoenvironmental sample. This approach allows the mechanistic effects of non-climatic variables, like the atmospheric CO_2 concentration to be explicitly considered in the reconstructions. Here we apply this approach to fossil-pollen data from North America at the Last Glacial Maximum (LGM) and mid-Holocene (MH), using two vegetation models, BIOME4 and BIOME5, to reconstruct growing-season temperature accumulation, winter and summer temperature, and variables that describe effective moisture. Reconstructed climate anomalies show coherent patterns, and are consistent among variables, and between biome models. As compared to previous reconstructed terrestrial bioclimatic variable data syntheses, our climate estimate at the LGM is warmer our climate. When biomization reconstructs biomes well, IMIFM approach arguably provides better quantitative climate estimates for paleo data-model comparison.

The recent IPCC reports (IPCC 2007,2013) clearly shows that the state-of-the-art climate models simulate more reliable modern climates and project more consistent future climates than previous assessments because of a better scientific understanding of the mechanism of climate changes. The higher-accuracy evaluation of those models performance should be implemented as usual through data-model comparison using global remote sensing data and reanalysis data. However, a large uncertainty remains about the magnitude and rate of projected future warming and in the role of feedbacks given their highly non-linear feature. Although the potential importance of physical and biogeochemical feedbacks has been recognized, we need to understand the response of the climate systems to larger external forcing and to different internal boundary conditions. Paleo data-model comparison can provide an opportunity to understand a better scientific understanding climate/environmental changes and reduce their various

uncertainties. For example, the multi-model ensemble has been used to obtain a best estimate of future climate and some measure of the range of uncertainties in the estimate. Paleo data-model comparisons (e.g. Harrison et al., 2013) suggest that we might adopt unequal weighting of models (the better paleo-simulations, the more weighting) for the multimodel ensemble for future climate simulations. This will require more observations to produce better documented and global-scale data syntheses.

1. Future research in regard to paleoclimate diagnostics

My future research plans include first the further investigation of the large-scale temperature responses in terms of atmospheric circulation and the hydrological cycle, because a key control of the robust responses is clear-sky longwave downward radiation that is closely related to near-surface air temperature and water vapor in the lower atmosphere. Furthermore, I will develop the research on large-scale climate responses, in particular focusing on precipitation and water-balance variables, under different climate conditions. Because precipitation patterns over the globe mostly depend on the large-scale atmospheric circulation, I will explore the main factors that control large-scale/regional precipitation pattern and their strength through changes in large-scale/regional atmospheric circulation under different external forcing (i.e., *lgm*, mid-Holocene (*MH*), and *historical* simulations in CMIP5 first) with paleo data-model comparison. This study will also help to assess the ability of climate models to predict large-scale precipitation patterns and atmospheric circulation under future climate change. Last of all, using the simple energy balance model, I plan to examine the large-scale temperature responses at the mid-Holocene in order to compare the response from orbitally induced changes in insolation with the responses induced by changes in atmospheric CO_2 concentration.

2. Future research in regard to the IMIFM approach

Because both inverse-modeling and forward-modeling approaches have advantages and disadvantages, these two approaches provide complementary approaches for data-model comparison. My future research plan is to 1) reconstruct temporal and spatial climate variations since the LGM using IMIFM approach for the Northern Hemisphere, South America, and Africa where existing syntheses of paleoecological data are available, 2) develop gridded time series data from those reconstructions, and 3) use these gridded data to perform data-model comparisons and paleoclimate diagnostics using transient climate simulations (e.g. TraCE-21000 and PMIP3 transient simulations). The first and second themes represent logical extensions of my dissertation (chapter IV) while the third will involve developing metrics to compare the transient reconstructions with transient simulations in order to evaluate the climate model's performance. Such research is relevant to the development of climate models in general. Moreover, the Bartlein et al. (2011) climate reconstruction data set could be updated using the IMIFM results, and the updated data could be used to reduce uncertainties in a prediction of climate sensitivity.

APPENDIX A

SUPPLEMENTARY INFORMATION TO CHAPTER II

Izumi, K., Department of Geography, University of Oregon, Eugene, Oregon 97403, USA
Bartlein, P.J., Department of Geography, University of Oregon, Eugene, Oregon 97403, USA
Harrison, S.P., School of Biological Sciences, Macquarie University, North Ryde, NSW 2109, Australia; Geography and Environmental Sciences, School of Human and Environmental Sciences, Reading University, Whiteknights, Reading, UK

Introduction

This auxiliary material contains (a) maps showing the simulated changes in past, historic and future climates for each of six models that have run the five CMIP5 experiments used in this study, expressed as experiment minus control anomalies, (b) a table summarizing the area-averaged climate changes obtained for each model used to construct Figure 2 (Table S1), (c) a table summarizing the reduced major axis (RMA) regressions (Table S2), and (d) a table summarizing the ratios for each model and each time period (Table S3).

Data sets used in the construction of the figures

All data used in the construction of the figures are available online in various repositories. Their provision here for the reproduction of the figures should not be used as a substitute for downloading and *citing* the original sources;

CMIP5/PMIP3 model output (Figs. 2.1-2.3, S2.1-S2.4)

http://cmip-pcmdi.llnl.gov/cmip5/

LGM and MH terrestrial climate reconstructions (Figs. 2.3, S2.5) (Bartlein et al., 2011)

http://www.ncdc.noaa.gov/paleo/pubs/bartlein2010/bartlein2010.html

LGM SST reconstructions (Fig. 2.3) (Margo Project Members, 2009)

http://www.ncdc.noaa.gov/paleo/pubs/margo2009/margo2009.html
http://www.nature.com/ngeo/journal/v2/n2/abs/ngeo411.html

MH SST reconstructions (Fig. 2.3) (Leduc et al., 2010)

http://doi.pangaea.de/10.1594/PANGAEA.737370

Other LGM reconstructions (Figs. 2.3, S2.5) (Schmittner et al., 2011)

http://www.ncdc.noaa.gov/paleo/pubs/schmittner2011/schmittner2011.html
http://www.sciencemag.org/content/334/6061/1385.short

"Historical" climate observations (Figs. 2.3, S2.5) (Brohan et al., 2006)

http://www.cru.uea.ac.uk/cru/data/temperature/

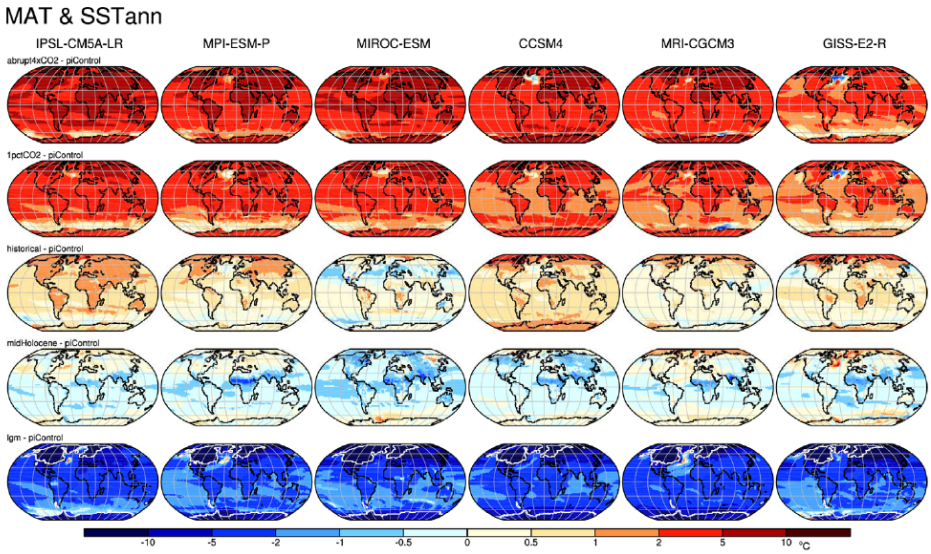

Figure S2.1. Simulated changes in mean annual temperature in the past, present and raised CO_2 experiments as shown by the IPSL-CM5A-LR, MPI-ESM-P, MIROC-ESM, CCSM4, MRI-CGCM3 and GISS-E2-R models respectively. The plots show the anomalies (experiment minus *piControl*) of mean annual temperature (MAT).

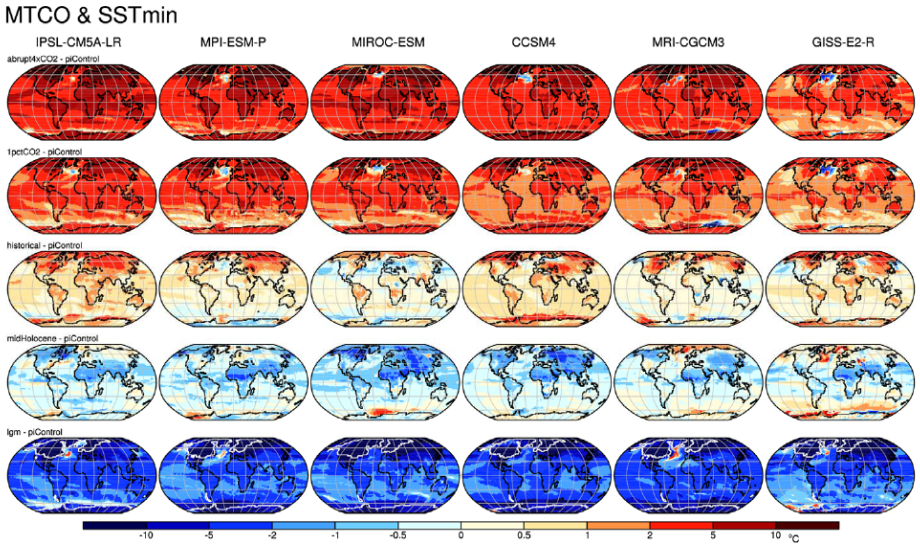

Figure S2.2. Simulated changes in mean temperature of the coldest month in the past, present and raised CO_2 experiments as shown by the IPSL-CM5A-LR, MPI-ESM-P, MIROC-ESM, CCSM4, MRI-CGCM3 and GISS-E2-R models respectively. The plots show the anomalies (experiment minus *piControl*) of mean temperature of the coldest month (MTCO).

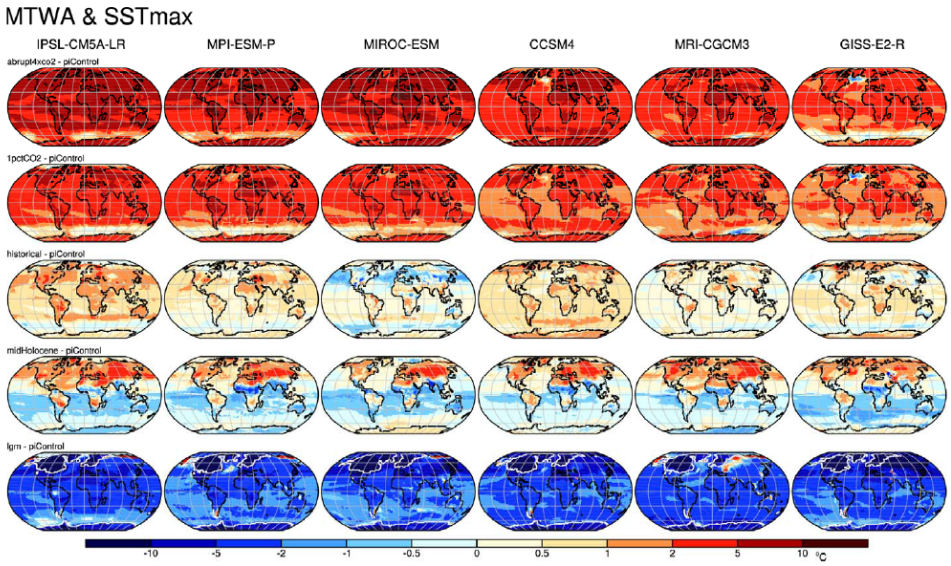

Figure. S2.3**.** Simulated changes in mean temperature of the warmest month in the past, present and raised CO2 experiments as shown by the IPSL-CM5A-LR, MPI-ESM-P, MIROC-ESM, CCSM4, MRI-CGCM3 and GISS-E2-R models respectively. The plots show the anomalies (experiment minus piControl) of mean temperature of the warmest month (MTWA).

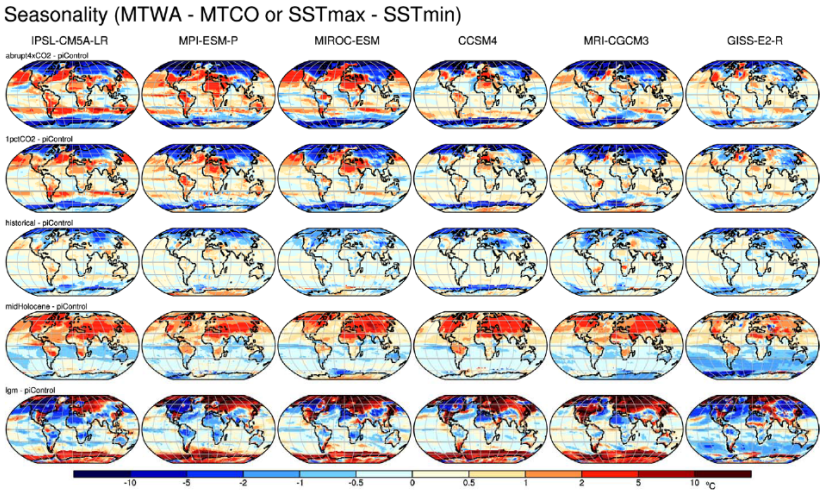

Figure. S2.4. Simulated changes in temperature seasonality in the past, present and raised CO_2 experiments as shown by the IPSL-CM5A-LR, MPI-ESM-P, MIROC-ESM, CCSM4, MRI-CGCM3 and GISS-E2-R models respectively. The plots show the anomalies (experiment minus *piControl*) of the change in temperature seasonality (MTWA-MTCO).

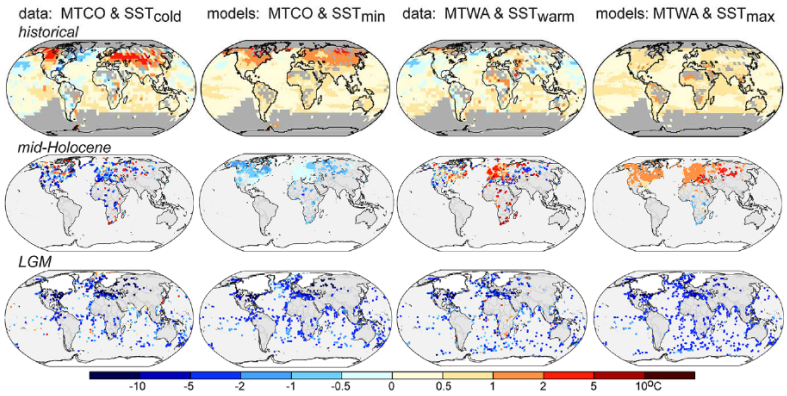

Figure S2.5. Comparison of simulated and observed changes in mean temperature of the coldest month (MTCO) and mean temperature of the warmest month (MTWA) for the *historical midHolocene* and *lgm* simulations compared with historical (20th century), mid-Holocene and Last Glacial Maximum observations. The historical observations are differences between the 1979-2005 and 1941-1970 long-term means from the HadCRUT3v combined land and ocean temperature data set (Brohan et al. 2006). The palaeoclimate reconstructions are from (Braconnot et al. 2012). The simulated values are ensemble averages of the outputs from the six CMIP5 models (for the *historical*, *midHolocene*, and *lgm* experiments) at the locations with observations at each time period.

Table S2.1**:** Summary of area-averaged climate anomalies for individual models for the *lgm (lgm), midHolocene (mH), historical (hist), 1pctCO$_2$ (1%)*, and *abrupt4xCO$_2$ (4x)* experiments compared to the control (*piControl*). The climate variables included are mean annual sea-surface temperature (SSTann), and minimum and maximum sea-surface temperature (SSTmin and SSTmax), and over land, mean annual temperature (MAT), mean temperature of the coldest month (MTCO), and mean temperature of the warmest month (MTWA), for the whole globe (global), northern hemisphere extratropics (30-85°N, NHEXT), and northern tropics (0-30°N, NHTrop).

	IPSL-CM5A-LR					MPI-ESM-P					MIROC-ESM					CCSM4					MRI-CGCM3					GISS-E2-R				
	lgm	*mH*	*hist*	*1%*	*4x*	*lgm*	*mH*	*hist*	*1%*	*4x*	*lgm*	*mH*	*hist*	*1%*	*4x*	*lgm*	*mH*	*hist*	*1%*	*4x*	*lgm*	*mH*	*hist*	*1%*	*4x*	*lgm*	*mH*	*hist*	*1%*	*4x*
SSTann																														
Global	-2.65	-0.17	0.69	2.35	4.65	-2.04	-0.22	0.38	2.19	3.98	-2.31	-0.35	0.04	2.21	4.62	-2.50	-0.19	0.66	1.92	3.39	-2.68	-0.1	0.18	1.77	3.07	-2.34	-0.15	0.37	1.49	1.87
NHEXT	-3.6	0.25	0.82	2.85	5.16	-2.58	-0.01	0.52	2.52	4.41	-5.16	-0.32	-0.46	2.7	5.44	-3.08	-0.22	0.58	2.17	3.28	-2.36	0.18	0.26	2.21	3.55	-4.07	0.20	0.15	1.36	1.75
NHTrop	-3.15	-0.22	0.84	2.69	4.98	-2.1	-0.32	0.54	2.72	4.67	-2.31	-0.51	0.06	2.54	4.95	-2.25	-0.26	0.62	1.79	3.05	-2.47	-0.19	0.16	1.93	3.24	-2.65	-0.32	0.44	1.82	2.22
MAT																														
Global	-7.22	-0.1	1.28	4.5	8.04	-7.58	-0.3	0.96	4.72	7.91	-8.97	-0.64	0.28	4.46	8.12	-7.49	-0.39	1.14	3.81	6.17	-6.8	-0.01	0.6	3.47	5.59	-8.95	-0.18	0.87	2.28	3.86
NHEXT	-10.9	0.13	1.45	5.2	8.9	-11.5	0.04	1.23	5.2	8.5	-15.0	-0.56	0.11	5.52	9.36	-11.4	-0.38	1.32	4.58	7.31	-9.35	0.28	0.85	4.26	6.54	-14.4	0.08	1.02	2.41	4.19
NHTrop	-4.21	-0.44	1.16	3.97	7.38	-3.65	-1.04	0.72	4.33	7.43	-3.16	-1.03	0.44	3.55	7.06	-3.46	-0.75	0.87	3.07	4.94	-3.51	-0.55	0.42	2.95	4.9	-3.83	-0.72	0.73	2.18	3.59
MTCO																														
Global	-7.07	-0.53	1.48	4.61	8.44	-7.92	-0.7	1.05	5.11	9.03	-10.0	-1.11	0.41	4.82	8.64	-8.73	-0.91	1.48	4.24	6.99	-8.25	-0.39	0.74	4.05	6.36	-8.67	-0.28	1.16	2.31	3.97
NHEXT	-10.5	-0.44	1.92	5.82	10.18	-11.9	-0.55	1.54	6.33	11.3	-16.7	-1.49	0.39	6.26	10.59	-12.7	-1.15	1.82	5.28	8.69	-11.4	-0.29	1.19	5.58	8.23	-14.2	0.05	1.46	2.52	4.42
NHTrop	-4.14	-1.07	0.96	3.42	6.67	-3.37	-1.47	0.54	3.94	6.74	-3.53	-1.56	0.45	3.33	6.39	-3.80	-1.27	0.84	2.97	4.82	-3.5	-0.99	0.37	2.92	4.81	-4.16	-1.06	0.83	2.10	3.65
MTWA																														
Global	-7.05	0.89	1.24	4.52	8.12	-6.81	0.59	0.8	4.58	7.98	-7.38	0.42	0.13	4.17	7.99	-5.93	0.66	0.94	3.58a	5.82	-4.19	0.82	0.52	2.91	4.77	-6.22	0.47	0.57	2.13	3.62
NHEXT	-10.1	1.67	1.22	4.87	8.4	-9.88	1.48	0.79	4.47	7.85	-11.7	1.33	-0.21	4.4	8.21	-9.21	1.51	0.98	4.04	6.43	-4.97	1.71	0.51	2.79	4.5	-12.9	1.15	0.50	2.05	3.67
NHTrop	-4.38	0.19	1.24	4.19	7.71	-3.7	-0.55	0.86	4.73	8.16	-3.05	-0.58	0.45	4.16	7.89	-3.21	-0.34	0.92	3.19	5.3	-3.29	-0.05	0.59	3.12	5.13	-3.73	-0.18	0.69	2.29	3.73
SSTmin																														
Global	-2.62	-0.25	0.65	2.14	4.35	-2.09	-0.28	0.35	2.04	3.75	-2.21	-0.39	0.05	2.06	4.28	-2.5	-0.25	0.62	1.83	3.25	-2.68	-0.16	0.18	1.68	2.94	-2.05	-0.01	0.35	1.42	1.78
SSTmax																														
Global	-2.83	-0.04	0.76	2.65	5.12	-2.05	-0.16	0.42	2.39	4.35	-2.42	-0.32	0.02	2.42	5	-2.66	-0.12	0.69	2.04	3.57	-2.79	0.02	0.19	1.91	3.29	-2.81	-0.25	0.41	1.62	2.01

Table S2.2: Summary of the reduced major axis (RMA) regressions for land-ocean contrast, high latitude amplification, and seasonality. The climate variables included are mean annual sea-surface temperature (SSTann), mean annual temperature (MAT), mean temperature of the coldest month (MTCO) and mean temperature of the warmest month (MTWA). Regressions are calculated separately for the whole globe (global), northern hemisphere extratropics (30-85°N, NHEXT), tropics (30°N to 30°S) and southern extratropics (65-30°S, SHEXT). We tested the null hypothesis that the RMA slope is equal to 1.0.

Feature	Region or variables	Slope	y-intercept	p-value
Land-ocean contrast, MAT	Global	2.370	-0.929	0.0000
	NHEXT	2.577	-1.342	0.0000
	Tropics	1.553	-0.002	0.0000
	SHEXT	1.864	-0.334	0.0000
Land-ocean contrast, MTCO	Global	2.707	-0.960	0.0000
	NHEXT	3.385	-0.959	0.0000
	Tropics	1.555	-0.090	0.0000
	SHEXT	2.443	-0.727	0.0000
Land-ocean contrast, MTWA	Global	1.922	-0.481	0.0000
	NHEXT	1.742	-1.156	0.0000
	Tropics	1.584	0.160	0.0000
	SHEXT	1.510	0.326	0.0001
High-latitude amplification	SST_{ann}	1.182	-0.302	0.0370
	MAT	2.019	-2.080	0.0000
	MTCO	2.278	-1.574	0.0000
	MTWA	1.647	-1.758	0.0030
Seasonality (land)	Global	1.207	-0.467	0.0052
	NHEXT	1.320	-0.269	0.0022
	Tropics	0.933	-0.294	0.0415
	SHEXT	1.480	-1.118	0.0161
Seasonality (ocean)	Global	0.885	-0.053	0.0000
	NHEXT	0.679	-0.247	0.0000
	Tropics	0.951	-0.035	0.0029
	SHEXT	0.914	-0.038	0.0651

High-latitude amplification (without LGM data)	SST_{ann}	1.007	0.065	0.4633
	MAT	1.180	0.515	0.0111
	MTCO	1.468	0.756	0.0000
	MTWA	0.918	0.694	0.2700

Table S2.3: Summary of large-scale ratios for individual models for the *lgm (lgm), midHolocene (mH), historical (hist), 1pctCO$_2$ (1%)*, and *abrupt4xCO$_2$ (4x)* experiments compared to the control (*piControl*). Land-ocean contrast (the ratio of the area-average mean near-surface air temperature changes over the land to area-average sea surface temperature) is shown for mean annual temperature (MAT versus SSTann), mean temperature of the warmest month (MTWA versus SSTmax) and mean temperature of the coldest month (MTCO versus SSTmin). High-latitude amplification (the ratio of the area-average mean surface temperature in the northern hemisphere extratropics to the area-average mean surface temperature in the northern hemisphere tropics) is shown for individual climate parameters (SSTann, MAT, MTCO, MTWA). Seasonality is the ratio of area-average mean MTCO to MTWA over the land and SSTmin to SSTmax over the ocean. Regressions are calculated separately for the whole globe (global), northern hemisphere extratropics (30-85°N, NHEXT), tropics (30°N to 30°S) and southern extratropics (65-30°S, SHEXT).

	IPSL-CM5A-LR					MPI-ESM-P					MIROC-ESM					CCSM4					MRI-CGCM3					GISS-E2-R				
	lgm	*mH*	*hist*	*1%*	*4x*	*lgm*	*mH*	*hist*	*1%*	*4x*	*lgm*	*mH*	*hist*	*1%*	*4x*	*lgm*	*mH*	*hist*	*1%*	*4x*	*lgm*	*mH*	*hist*	*1%*	*4x*	*lgm*	*mH*	*hist*	*1%*	*4x*
Land-ocean contrast																														
Global Annual	2.72	0.59	1.86	1.91	1.73	3.72	1.36	2.53	2.16	1.99	3.88	1.83	7.00	2.02	1.76	2.90	2.05	1.73	1.98	1.82	2.54	0.10	3.33	1.96	1.82	3.82	1.20	2.35	1.53	2.06
NHEXT Annual	3.02	0.52	1.77	1.84	1.72	4.46	4.00	2.37	2.06	1.93	2.91	1.75	0.24	2.04	1.72	2.87	1.73	2.28	2.11	2.23	3.96	1.56	3.27	1.93	1.84	3.53	0.40	6.80	1.77	2.39
NHTrop Annual	1.34	2.00	1.38	1.48	1.48	1.74	3.25	1.33	1.59	1.59	1.37	2.02	7.33	1.40	1.43	1.54	2.88	1.40	1.72	1.62	1.42	2.89	2.63	1.53	1.51	1.45	2.25	1.66	1.20	1.62
Tropics Annual	1.41	1.31	1.45	1.52	1.48	1.84	2.06	1.48	1.71	1.69	1.53	1.61	3.13	1.48	1.49	1.54	2.26	1.38	1.66	1.60	1.43	1.74	2.50	1.55	1.54	1.61	1.52	1.54	1.24	1.66
Global Warmest	2.49	22.3	1.63	1.71	1.59	3.32	3.69	1.90	1.92	1.83	3.05	1.31	6.50	1.72	1.72	2.23	5.50	1.36	1.74	1.63	1.50	41.0	2.74	1.52	1.45	2.93	1.88	1.39	1.31	1.80
Global Coldest	2.70	2.12	2.28	2.15	1.94	3.79	2.50	3.00	2.50	2.41	4.53	2.85	8.20	2.34	2.34	3.49	3.64	2.39	2.32	2.15	3.08	2.44	4.11	2.41	2.16	4.23	28.0	3.31	1.63	2.23
High-latitude amplification																														
SSTann	1.14	1.14	0.98	1.05	1.04	1.23	0.03	0.96	0.93	0.94	2.23	0.63	7.67	1.06	1.10	1.77	0.85	0.94	1.21	1.08	0.96	0.95	1.63	1.15	1.10	1.54	0.63	0.34	0.75	0.79
MAT	2.58	0.30	1.25	1.31	1.21	3.15	0.04	1.71	1.20	1.14	4.75	0.54	0.25	1.55	1.33	2.20	0.51	1.52	1.49	1.48	2.66	0.51	2.02	1.44	1.33	3.75	0.11	1.40	1.11	1.17
MTCO	2.53	0.41	2.00	1.70	1.53	3.54	0.37	2.85	1.61	1.68	4.74	0.96	0.87	1.88	1.56	3.30	0.91	2.17	1.78	1.80	3.24	0.29	3.22	1.91	1.71	3.40	0.05	1.76	1.20	1.21
MTWA	2.31	8.79	0.98	1.16	1.09	2.67	2.69	0.92	0.95	0.96	3.83	2.29	0.47	1.06	1.04	2.87	4.44	1.07	1.27	1.21	1.51	34.2	0.86	0.89	0.88	3.46	6.39	0.72	0.90	0.98
Seasonality																														
Global Land	1.00	-0.59	1.19	1.02	1.04	1.16	-1.19	1.31	1.12	1.13	1.36	2.64	3.15	1.16	1.08	1.47	-1.38	1.57	1.19	1.20	1.97	-0.48	1.42	1.39	1.33	1.05	-0.60	2.04	1.08	1.10
Global Ocean	0.93	6.25	0.86	0.81	0.85	1.02	1.75	0.83	0.85	0.86	0.91	1.22	2.50	0.85	0.86	0.94	2.08	0.90	0.90	0.91	0.96	-8.00	0.95	0.88	0.89	0.73	0.04	0.85	0.88	0.89
NHEXT LAND	1.03	-0.26	1.57	1.20	1.21	1.21	-0.37	1.95	1.42	1.44	1.43	-1.12	-1.86	1.42	1.29	1.37	-0.76	1.86	1.31	1.35	2.28	-0.17	2.33	2.00	1.83	1.10	0.04	2.92	1.23	1.20
NHEXT Ocean	0.61	-0.15	0.59	0.54	0.63	0.82	-0.45	0.68	0.72	0.71	0.75	-2.89	0.74	0.55	0.55	0.87	-1.26	0.70	0.75	0.76	0.92	-0.17	0.73	0.71	0.72	0.52	0.20	0.28	0.56	0.60

APPENDIX B

SUPPLEMENTARY INFORMATION TO CHAPTER III

Izumi, K., Department of Geography, University of Oregon, Eugene, Oregon 97403, USA
Bartlein, P.J., Department of Geography, University of Oregon, Eugene, Oregon 97403, USA
Harrison, S.P., School of Biological Sciences, Macquarie University, North Ryde, NSW 2109, Australia; Geography and Environmental Sciences, School of Human and Environmental Sciences, Reading University, Whiteknights, Reading, UK

The supplementary information (SI) contains the following:

(1) scatter plots of large-scale surface temperature responses in past, historical, and projected warm climates for various seasonal and spatial subsamples of data (Fig. S3.1);
(2) maps showing the robustness of the annual temperature anomalies and partial temperature change components (PTCs) for the *lgm* and *abrupt4xCO_2* simulations (Figs. S3.2 and S3.3);
(3) maps showing the seasonal (winter and summer) ensemble-average mean surface-temperature changes, seasonality changes (summer minus winter), and their robustness in warm and cold climates for CMIP5 multimodel mean (Figs. S3.4-S3.9)
(4) plots of ensemble-average zonal-mean temperature differences for winter, summer and summer minus winter for the *lgm* and *abrupt4xCO_2*, simulations (Figs. S3.10-S3.12)

(5) maps showing the annual mean surface temperature changes and the PTC of each component in warm and cold climates for each of the six individual models (Figs. S3.13-S3.24); and

(6) a table summarizing the global (85°S-85°N) TOA annual mean radiation budget anomalies for each CMIP5 model and their ensemble mean (Table S3.1).

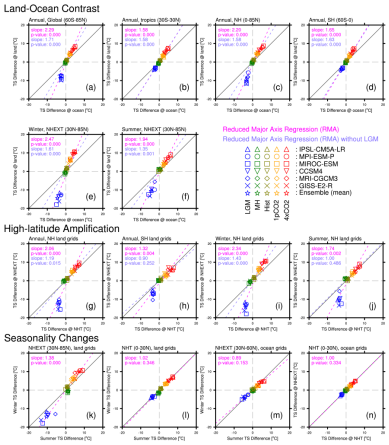

Figure S3.1. Scatter plots showing area-weighted average of surface temperature changes in past, historical and projected warmer climates. The values plotted are the simulated changes in surface temperature (experiment minus *piControl*) for each of the six models and their ensemble mean. Differences in relative warming/cooling over land and ocean (land-ocean contrast) are shown for (a) the globe (60°S-85°N), (b) the tropics (30°S-30°N), (c) the northern hemisphere (0-85°N), (d) the southern hemisphere (60°S-0), (e) the northern extratropics (30°N-85°N) in winter (DJF), and (f) the northern extratropics in summer (JJA). Differences in the relative warming/cooling in the northern extratropics (30°N-85°N) and northern tropics (0°-30°N) (latitudinal amplification) are shown for land areas, and for (g) annual mean, (i) winter (DJF), and (j) summer (JJA). Differences in the relative warming/cooling in the southern extratropics (85°S-30°S) and northern tropics (30°S-0) (latitudinal amplification) are shown for land areas, and for (h) annual mean. Changes in seasonality are shown for (k) northern extratropics land, (l) northern tropics land, (m) northern extratropics ocean, and northern tropics ocean (n). The diagonal gray lines are 1:1 lines, while the magenta lines are the reduced major axis (RMA) regression lines, and the p-values shown are those for a test of the null hypothesis that the slopes of the RMA regression line are equal to 1.0. In Figures 1a to 1g, an additional RMA regression line fit without using data from the *lgm* simulation, and the appropriate statistics, are shown in purple. The scatter of points in the individual panels show that the land-ocean contrast, high-latitude amplification and changes in seasonality are consistent across the cold-climate, historical and warm-climate simulations.

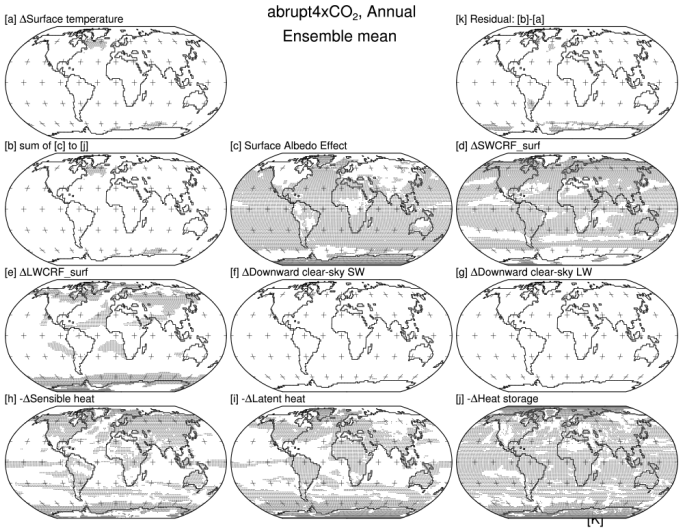

Figure S3.2. Maps of the robustness of the annual surface temperature differences (between *abrupt4xCO₂* and *piControl*) and partial temperature changes (PTC). Robustness is defined as agreement in the sign of the anomaly or PTC among all six models, and is shown by stippling at locations where there is *not* uniform agreement among models in the sign of the temperature changes. Locations without stippling are consequently those were there was agreement in sign across the six models.

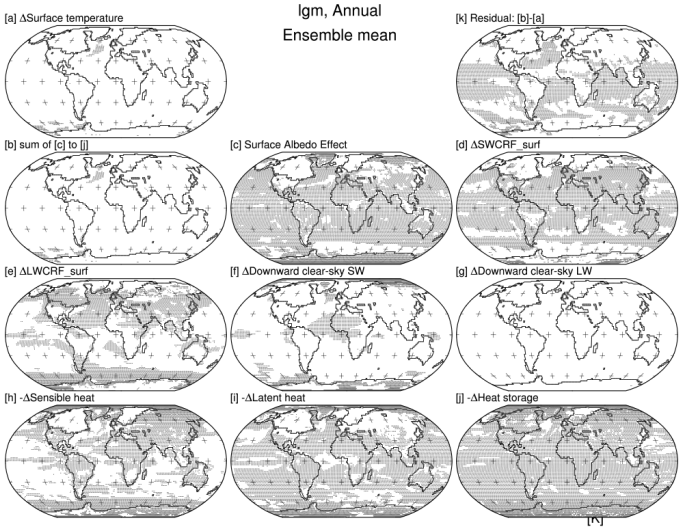

Figure S3.3. Maps of the robustness of the annual surface temperature differences (between *lgm* and *piControl*) and partial temperature changes (PTC) of each. Stippling as in Fig. S3.2.

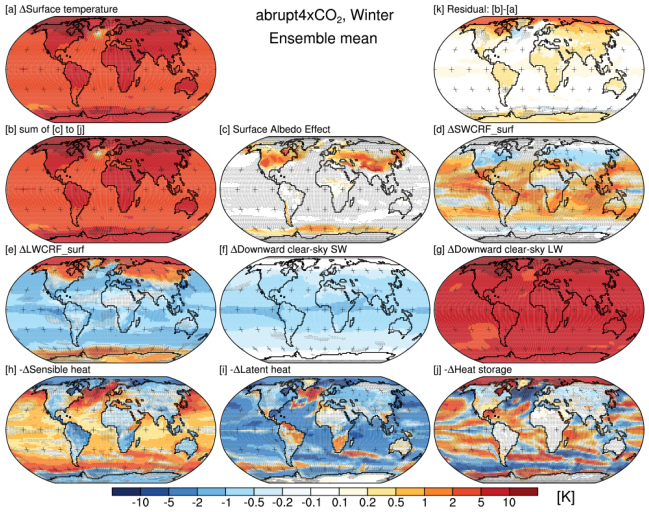

Figure S3.4. Maps of ensemble-average winter mean temperature differences between the *abrupt4xCO₂* and *piControl* simulations [a], and for the partial temperature change (PTC) of each component [b through j] (equation 11), and the residuals [k] (equation 12). Winter is defined as DJF in the northern hemisphere and JJA in the southern hemisphere. Stippling as in Fig. S3.2.

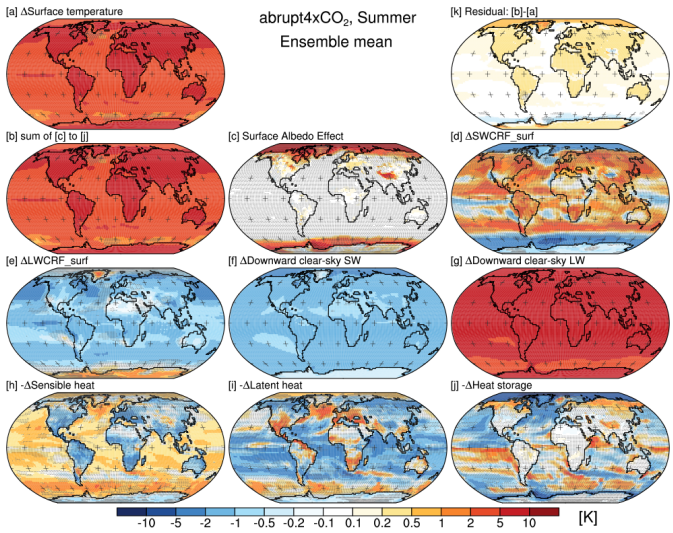

Figure S3.5. Maps of ensemble-average summer mean temperature differences between the *abrupt4xCO₂* and *piControl* simulations [a], and for the partial temperature change (PTC) of each component [b through j] (equation 11), and the residuals [k] (equation 12). Summer is defined as JJA in the northern hemisphere and DJF in the southern hemisphere. Stippling as in Fig. S3.2

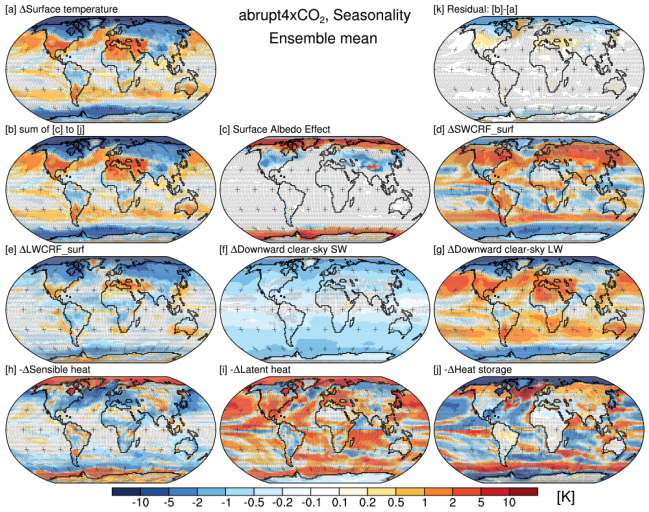

Figure S3.6. Maps of ensemble-average seasonality changes of temperature differences between the *abrupt4xCO₂* and *piControl* simulations [a], and for the partial temperature change (PTC) of each component [b through j] (equation 11), and the residuals [k] (equation 12). Seasonality change is defined as the difference between summer (JJA in the northern hemisphere and DJF in the southern hemisphere) and winter (DJF in the northern hemisphere and JJA in the southern hemisphere). Stippling as in Fig. S3.2.

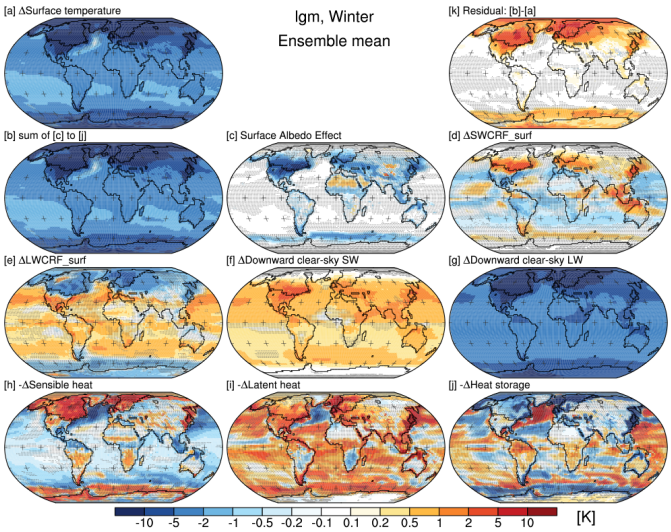

Figure S3.7. Maps of ensemble-average winter mean temperature differences between the *lgm* and *piControl* simulations [a], and for the partial temperature change (PTC) of each component [b through j] (equation 11), and the residuals [k] (equation 12). Winter is defined as DJF in the northern hemisphere and JJA in the southern hemisphere. Stippling as in Fig. S3.2.

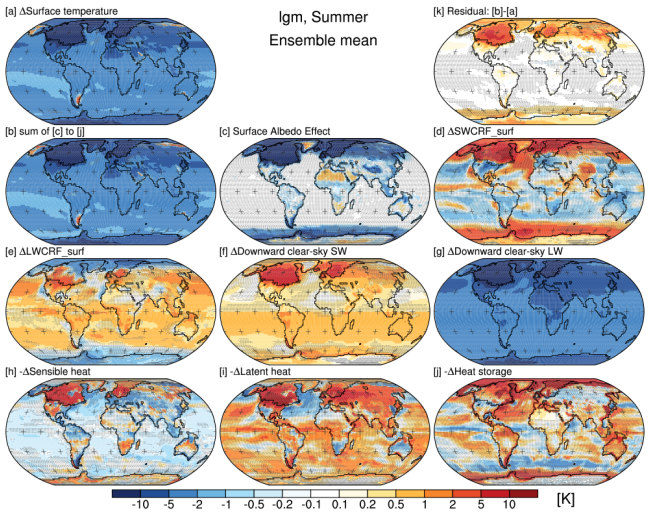

Figure S3.8. Maps of ensemble-average summer mean temperature differences between the *lgm* and *piControl* simulations [a], and for the partial temperature change (PTC) of each component [b through j] (equation 11), and the residuals [k] (equation 12). Summer is defined as JJA in the northern hemisphere and DJF in the southern hemisphere. Stippling as in Fig. S3.2.

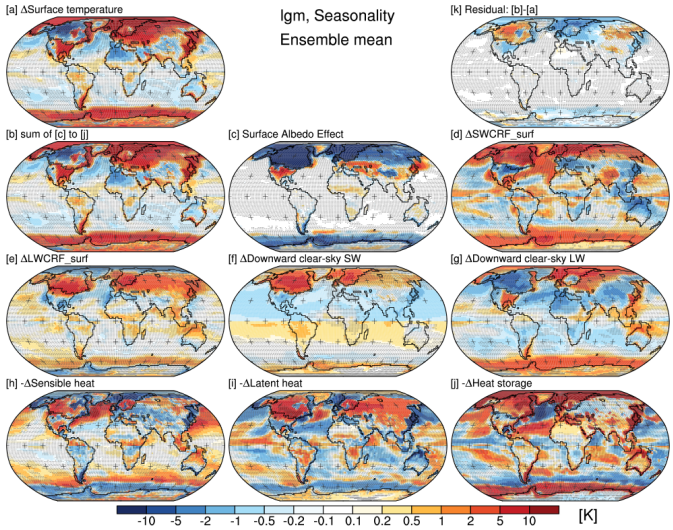

Figure S3.9. Maps of ensemble-average seasonality changes of temperature differences between the *lgm* and *piControl* simulations [a], and for the partial temperature change (PTC) of each component [b through j] (equation 11), and the residuals [k] (equation 12). Seasonality change is defined as the difference between summer (JJA in the northern hemisphere and DJF in the southern hemisphere) and winter (DJF in the northern hemisphere and JJA in the southern hemisphere). Stippling as in Fig. S3.2.

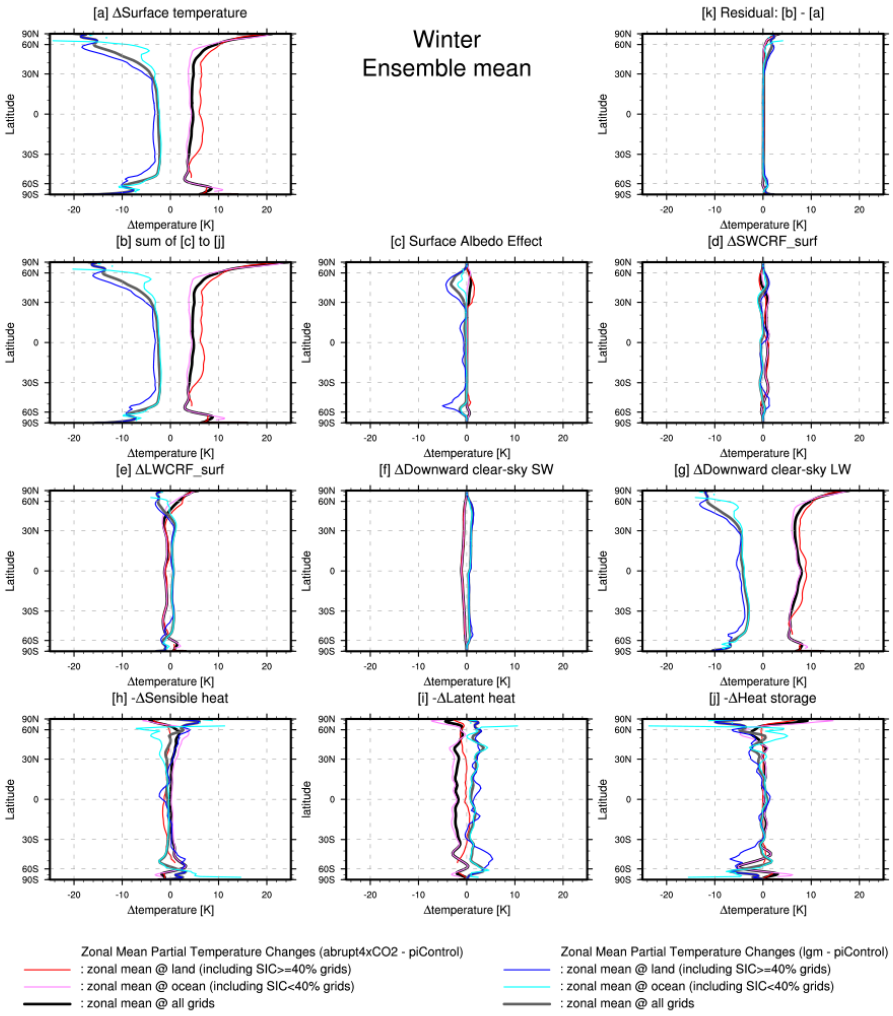

Figure S3.10. The ensemble-average zonal-mean winter surface temperature differences between the *abrupt4*×CO_2 and *lgm* and *piControl* simulations [a], and for the partial temperature change (PTC) of each component [b though j in equation 11], and the residuals [k] (equation 12); bold black (land + ocean), red (land only), and pink (ocean only) for *abrupt4*×CO_2; bold gray (land + ocean), blue (land only), and light blue (ocean only) for *lgm*. Winter is defined as the DJF mean over the Northern Hemisphere and JJA mean over the Southern Hemisphere.

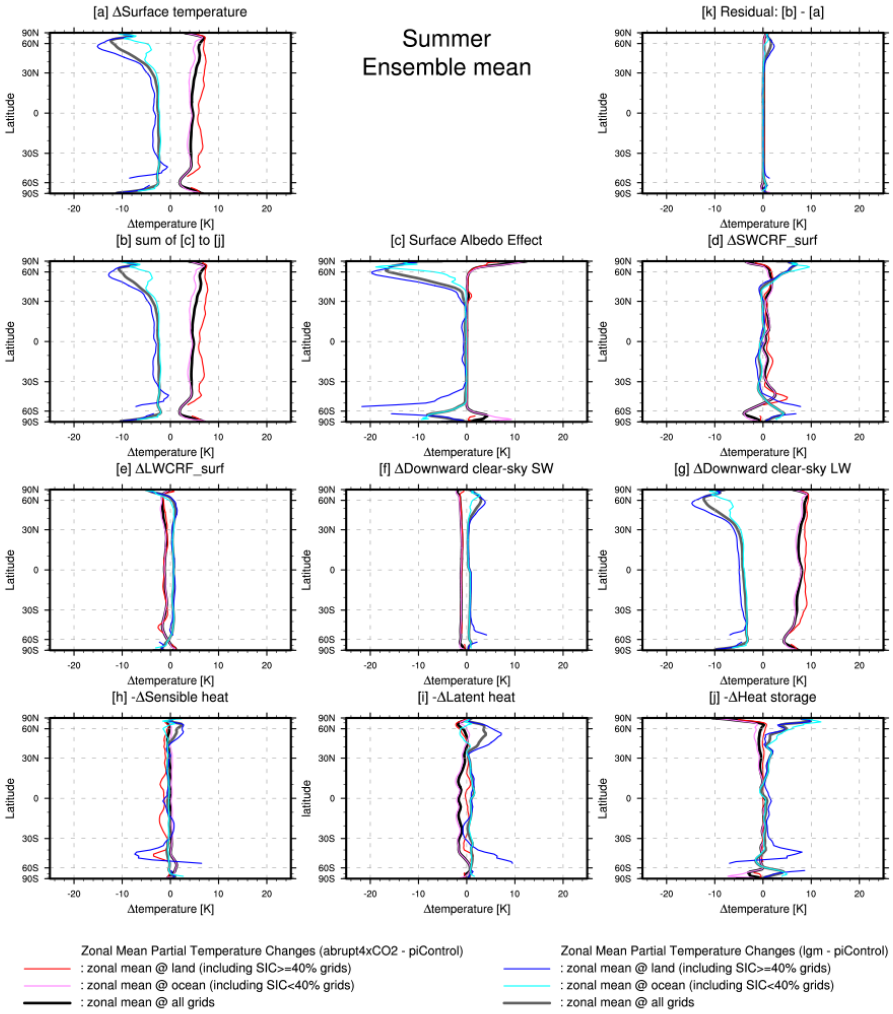

Figure S3.11. The ensemble-average zonal-mean summer surface temperature differences between the *abrupt4×CO_2* and *lgm* and *piControl* simulations [a], and for the partial temperature change (PTC) of each component [b though j in equation 11], and the residuals [k] (equation 12); bold black (land + ocean), red (land only), and pink (ocean only) for *abrupt4×CO_2*; bold gray (land + ocean), blue (land only), and light blue (ocean only) for *lgm*. Summer is defines as the JJA mean over the Northern Hemisphere and DJF mean over the Southern Hemisphere.

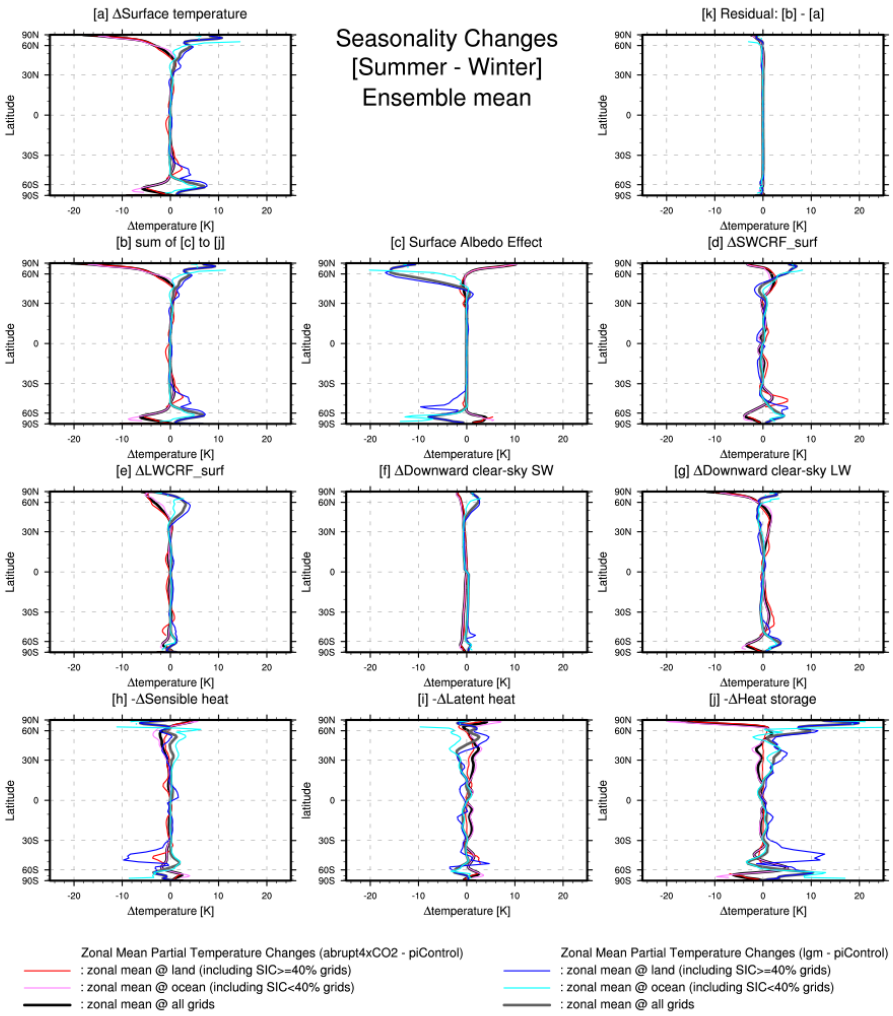

Figure S3.12. The ensemble-average zonal-mean summer minus winter surface temperature differences (changes in seasonality) between the *abrupt4*×CO_2 and *lgm* and *piControl* simulations [a], and for the partial temperature change (PTC) of each component [b though j in equation 11], and the residuals [k] (equation 12); bold black (land + ocean), red (land only), and pink (ocean only) for *abrupt4*×CO_2; bold gray (land + ocean), blue (land only), and light blue (ocean only) for *lgm*. Winter is defined as the DJF mean over the Northern Hemisphere and JJA mean over the Southern Hemisphere.

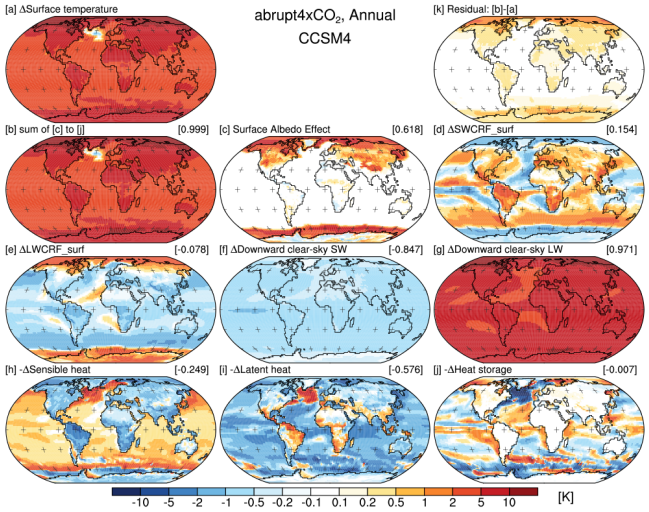

Figure S3.13. Maps of CCSM4 annual temperature differences between the *abrupt4×CO₂* and *piControl* simulations [a], and for the partial temperature change (PTC) of each component [b though j] (equation 11), and the residuals [k] (equation 12). The numbers in square brackets are the uncentered anomaly correlations (AC_U) between each map in panels [b] through [j] and the annual temperature differences [a] with global (85ºS-85ºN) data.

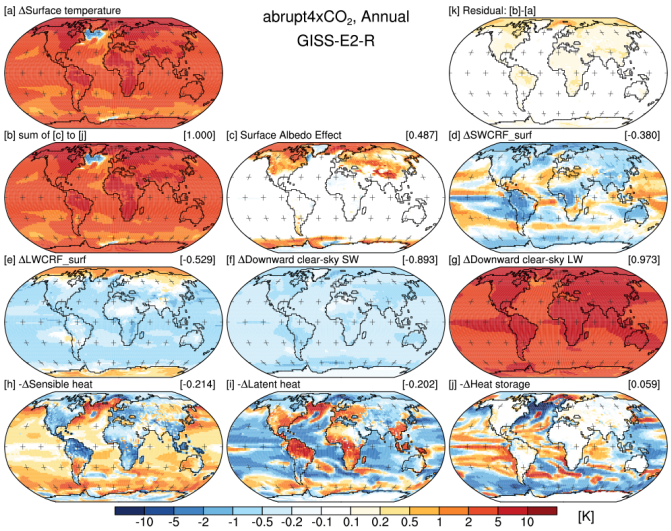

Figure S3.14. Maps of GISS-E2-R annual temperature differences between the *abrupt4×CO₂* and *piControl* simulations [a], and for the partial temperature change (PTC) of each component [b though j] (equation 11), and the residuals [k] (equation 12). The numbers in square brackets are the uncentered anomaly correlations (AC_U) between each map in panels [b] through [j] and the annual temperature differences [a] with global (85ºS-85ºN) data.

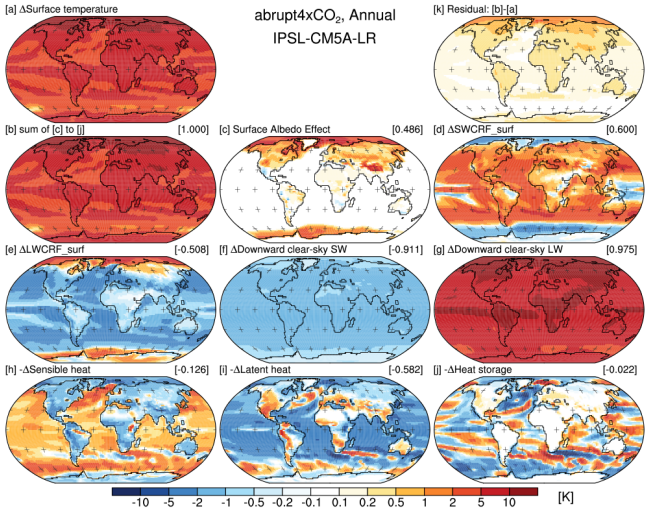

Figure S3.15. Maps of IPSL-CM5A-LR annual temperature differences between the *abrupt4×CO₂* and *piControl* simulations [a], and for the partial temperature change (PTC) of each component [b though j] (equation 11), and the residuals [k] (equation 12). The numbers in square brackets are the uncentered anomaly correlations (AC_U) between each map in panels [b] through [j] and the annual temperature differences [a] with global (85ºS-85ºN) data.

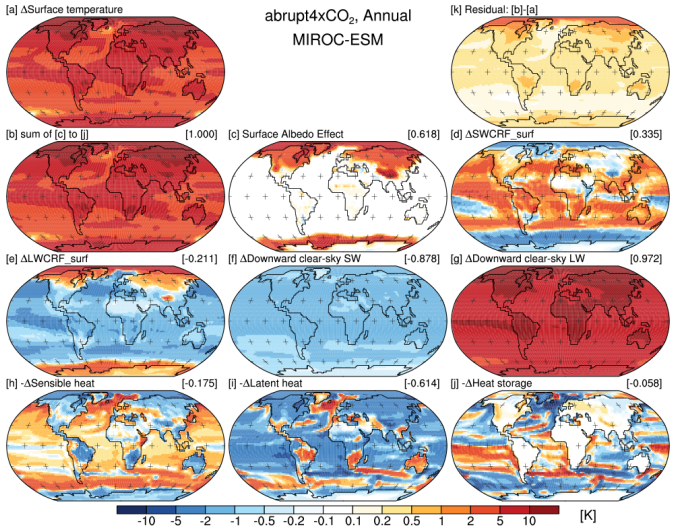

Figure S3.16. Maps of MIROC-ESM annual temperature differences between the *abrupt4×CO₂* and *piControl* simulations [a], and for the partial temperature change (PTC) of each component [b though j] (equation 11), and the residuals [k] (equation 12). The numbers in square brackets are the uncentered anomaly correlations (AC_U) between each map in panels [b] through [j] and the annual temperature differences [a] with global (85ºS-85ºN) data.

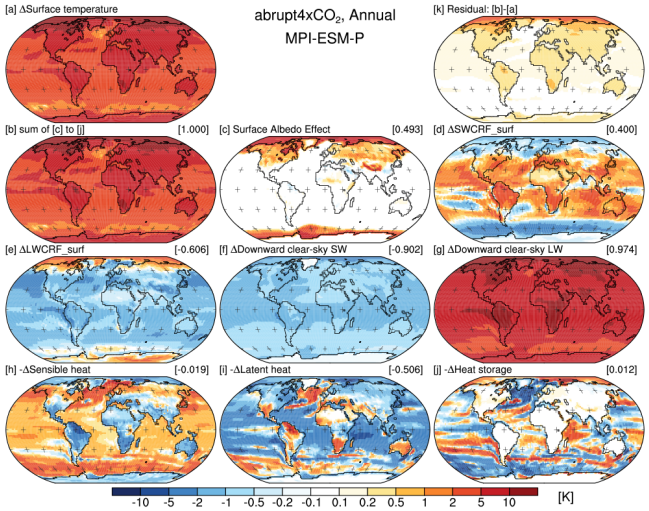

Figure S3.17. Maps of MPI-ESM-P annual temperature differences between the *abrupt4×CO₂* and *piControl* simulations [a], and for the partial temperature change (PTC) of each component [b though j] (equation 11), and the residuals [k] (equation 12). The numbers in square brackets are the uncentered anomaly correlations (AC_U) between each map in panels [b] through [j] and the annual temperature differences [a] with global (85ºS-85ºN) data.

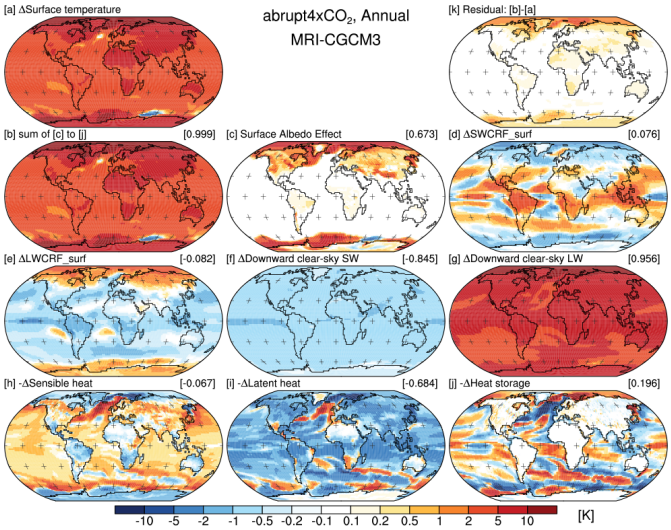

Figure S3.18. Maps of MRI-CGCM3 annual temperature differences between the *abrupt4×CO₂* and *piControl* simulations [a], and for the partial temperature change (PTC) of each component [b though j] (equation 11), and the residuals [k] (equation 12). The numbers in square brackets are the uncentered anomaly correlations (AC_U) between each map in panels [b] through [j] and the annual temperature differences [a] with global (85ºS-85ºN) data.

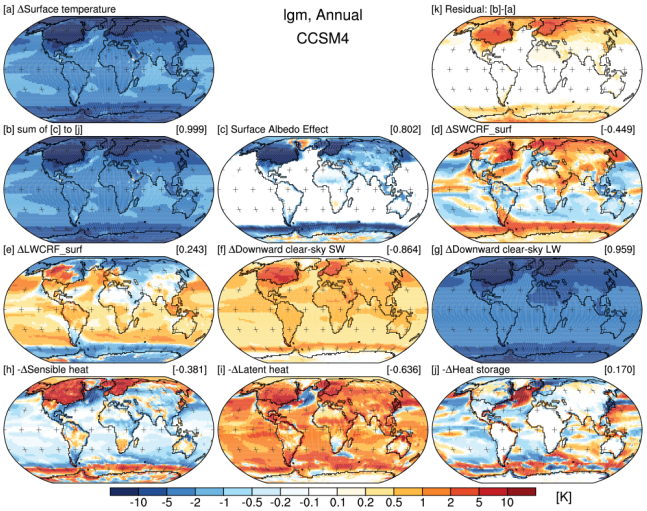

Figure S3.19. Maps of CCSM4 annual temperature differences between the *lgm* and *piControl* simulations [a], and for the partial temperature change (PTC) of each component [b though j] (equation 11), and the residuals [k] (equation 12). The numbers in square brackets are the uncentered anomaly correlations (AC_U) between each map in panels [b] through [j] and the annual temperature differences [a] with global (85ºS-85ºN) data.

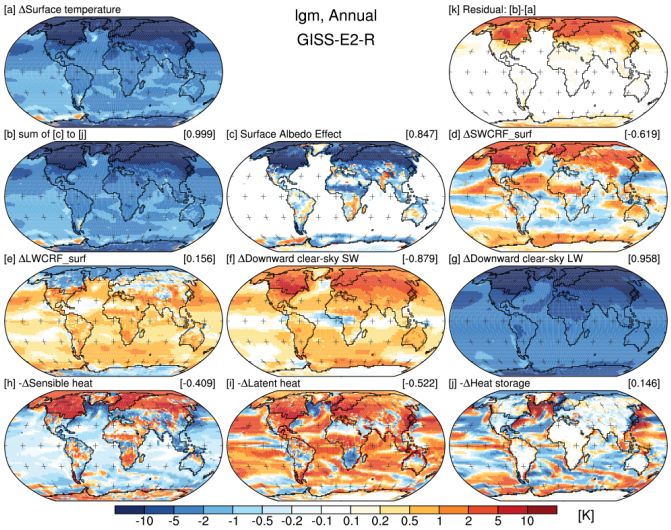

Figure S3.20. Maps of GISS-E2-R annual temperature differences between the *lgm* and *piControl* simulations [a], and for the partial temperature change (PTC) of each component [b though j] (equation 11), and the residuals [k] (equation 12). The numbers in square brackets are the uncentered anomaly correlations (AC_U) between each map in panels [b] through [j] and the annual temperature differences [a] with global (85ºS-85ºN) data.

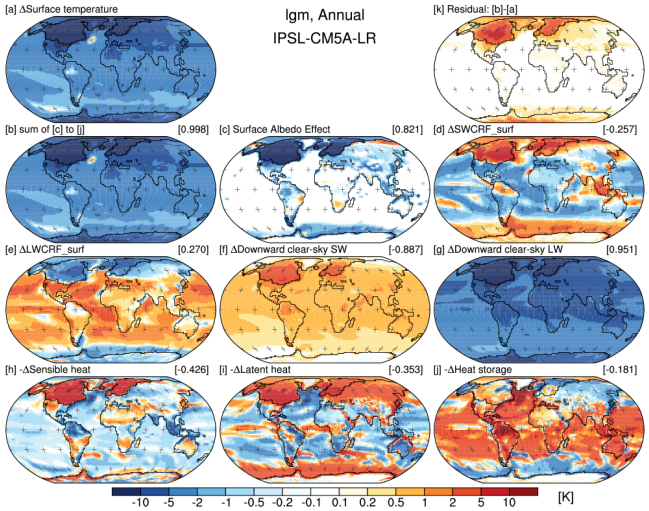

Figure S3.21. Maps of IPSL-CM5A-LR annual temperature differences between the *lgm* and *piControl* simulations [a], and for the partial temperature change (PTC) of each component [b though j] (equation 11), and the residuals [k] (equation 12). The numbers in square brackets are the uncentered anomaly correlations (AC_U) between each map in panels [b] through [j] and the annual temperature differences [a] with global (85ºS-85ºN) data.

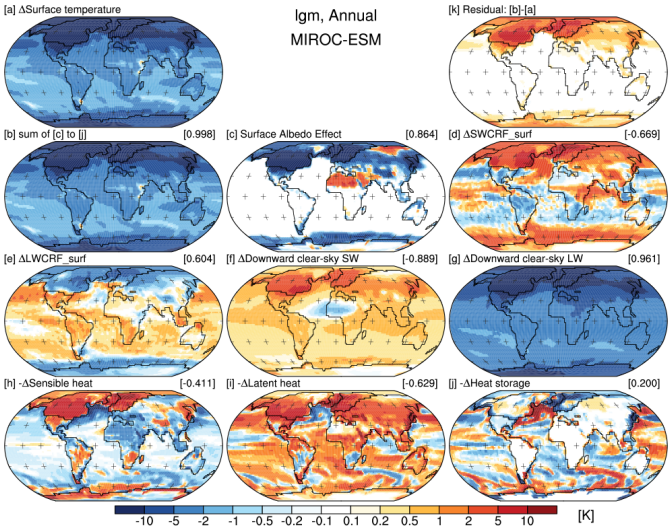

Figure S3.22. Maps of MIROC-ESM annual temperature differences between the *lgm* and *piControl* simulations [a], and for the partial temperature change (PTC) of each component [b though j] (equation 11), and the residuals [k] (equation 12). The numbers in square brackets are the uncentered anomaly correlations (AC_U) between each map in panels [b] through [j] and the annual temperature differences [a] with global (85ºS-85ºN) data.

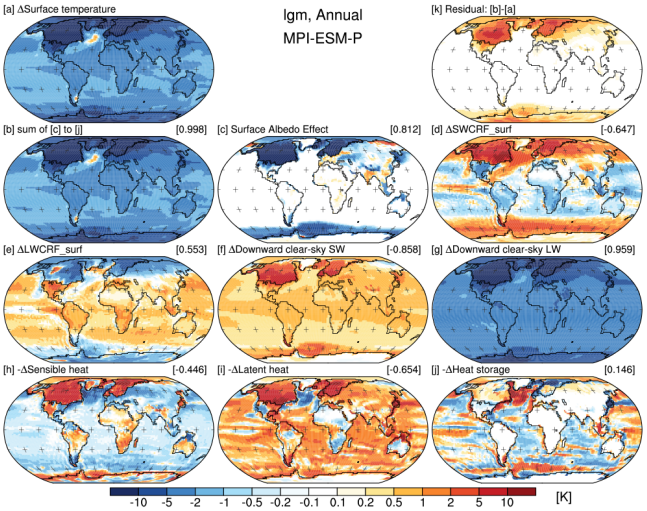

Figure S3.23. Maps of MPI-ESM-P annual temperature differences between the *lgm* and *piControl* simulations [a], and for the partial temperature change (PTC) of each component [b though j] (equation 11), and the residuals [k] (equation 12). The numbers in square brackets are the uncentered anomaly correlations (AC_U) between each map in panels [b] through [j] and the annual temperature differences [a] with global (85ºS-85ºN) data.

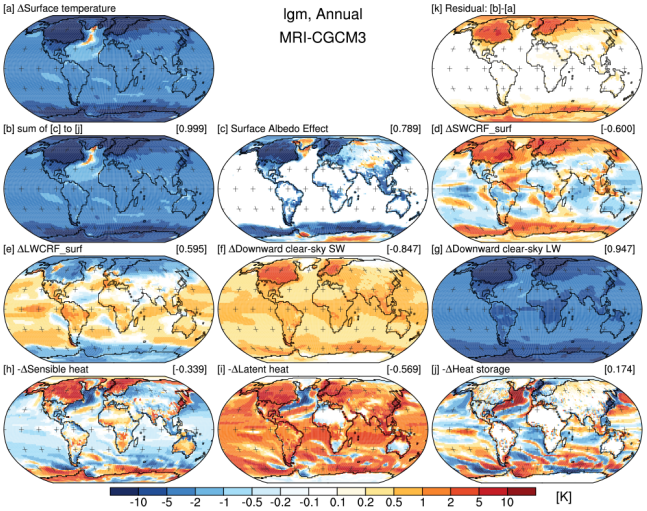

Figure S3.24. Maps of MRI-CGCM3 annual temperature differences between the *lgm* and *piControl* simulations [a], and for the partial temperature change (PTC) of each component [b though j] (equation 11), and the residuals [k] (equation 12). The numbers in square brackets are the uncentered anomaly correlations (AC_U) between each map in panels [b] through [j] and the annual temperature differences [a] with global (85ºS-85ºN) data.

Table S3.1. TOA annual mean radiation budget anomalies (from *piControl*) for CMIP5 models and multimodel mean for the globe (85°S to 85°N); a) *abrupt4×CO_2*, and b) *lgm* simulations. The downward solar (SW in), reflected solar (SW out), outgoing longwave radiation (LW out), and net (Imbalance) radiation is given in W m^{-2}.

a) abrupt4xCO2

	SW in	SW out	LW out	Imbalance
IPSL-CM5A-LR	0.0	-10.1	8.5	1.6
MPI-ESM-P	0.0	-4.5	2.9	1.6
MIROC-ESM	0.0	-7.2	4.4	2.8
CCSM4	0.0	-3.7	4.2	-0.5
MRI-CGCM3	0.0	-4.2	2.9	1.3
GISS-E2-R	0.0	0.8	-2.5	1.7
Ensemble mean	0.0	-4.8	3.5	1.3

b) lgm

	SW in	SW out	LW out	Imbalance
IPSL-CM5A-LR	0.0	8.8	-8.3	-0.5
MPI-ESM-P	0.0	5.0	-4.8	-0.2
MIROC-ESM	0.1	5.9	-5.9	0.0
CCSM4	0.1	6.7	-6.6	-0.1
MRI-CGCM3	0.1	6.5	-6.9	0.4
GISS-E2-R	-0.2	4.9	-4.8	-0.1
Ensemble mean	0.0	6.3	-6.2	-0.1

APPENDIX C

SUPPLEMENTARY INFORMATION TO CHAPTER IV

Izumi, K., Department of Geography, University of Oregon, Eugene, Oregon 97403, USA
Bartlein, P.J., Department of Geography, University of Oregon, Eugene, Oregon 97403, USA

This appendix contains supplementary information (SI) for Chapter IV and includes the following:

(1) an equation for calculating the biomization affinity scores
(2) an equation for calculating the climate moisture index (CMI)
(3) BIOME4 simulated biomes at modern, mid-Holocene, and last glacial maximum for North America (Fig. S1);
(4) Correlation between observed and simulated climate variable values by IMIFM using BIOME4 in North American for modern conditions (Fig. S2);
(5) Latitudinal cross sections of reconstructed temperature anomalies and hydrological anomalies (Fig. S3 and S4)

Calculating biome affinity scores

An affinity scores for a biomes is a measure of its likely presence at a site given a particular pollen spectrum (but are not equivalent to proportion of the area covered by individual biome at the site). The lower the score, the less likely the biome is, and the ordinal scale makes it a 'winner takes all' assignment. The scores are calculated for all potential biomes at each site according to the following equation (Prentice and Webb 1998):

$$\left\{\max\left[0,\left(p_{jk}-\theta_j\right)\right]\right\} \quad A_{ik}=\sum_j \delta_{ij}\sqrt{\left\{\max\left[0,\left(p_{jk}-\theta_j\right)\right]\right\}}$$

where
A_{ik} : the affinity score of pollen sample k for biome i.
$\sum$: summation is over all taxa j.
p_{jk} : the pollen percentage of taxon j in sample k.
δ_{ij} :the entry in he biome × taxon matrix for biome i and taxon j (δ_{ij}= 0 or 1).
θ_j : a threshold value, initially set for all taxa at 0.5%.

The equation indicates that the contribution to the affinity score made by a group of taxa constituting a fixed percentage of the total pollen sum increases with the diversity of the group. For example, two taxa with 10% each of the total pollen sum would contribute $2\times\sqrt{10-0.5}=6.16$ to the affinity score; four taxa with 5% each would contribute $4\times\sqrt{5-0.5}=8.49$; eight taxa with 2.5% each would contribute $8\times\sqrt{2.5-0.5}=11.31$. Thus, the occurrence of several taxa that each could occur in a particular biome, increases the affinity score for that biome.

Taking the square root of the term $\left\{\max\left[0,\left(p_{jk}-\theta_j\right)\right]\right\}$ downweights the more abundant taxa (stabilizes variance and increase the method's sensitivity to less abundant taxa), while the threshold value reduces noise arising from low amounts of pollen.

Climate moisture index (CMI)

The annual average climate moisture index (CMI, Willmott and Feddema 1992) is calculated according to the following equation:

$CMI=\left(MAP/PET\right)-1$ when MAP < PET
$CMI=1-\left(PET/MAP\right)$ when MAP ≥ PET

where
MAP: mean annual precipitation (mm/yr)
PET: potential evapotranspiration (mm/yr)

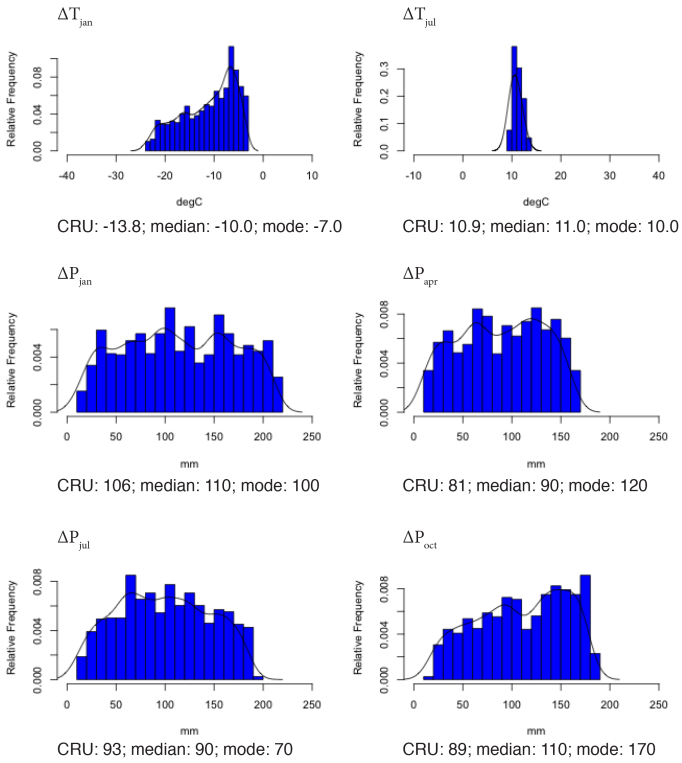

Figure S4.1. BIOME5 inferred climate distribution at a taiga site (laritude: 52°52'; longitude: -57°03'; elevation: 200 m). Both median and mode of each climatic and bioclimatic variables were calculated for the optimal value of reconstructed climate at each site.

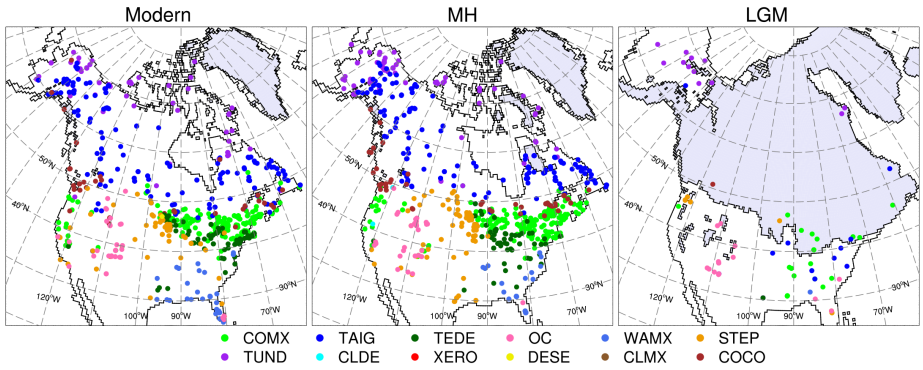

Figure S4.2. Simulated biomes (by IMIFM with BIOME4) at modern, mid-Holocene, and last glacial maximum. COMX, cool mixed forest; TAIG, taiga; TEDE, temperate deciduous forest; OC, open conifer woodland; WAMX, broadleaved evergreen/warm mixed forest; STEP, steppe; TUND, tundra; CLDE, cold deciduous forest; XERO, xerophytic woods/scrub; DESE, desert; CLMX, cold mixed forest; COCO, cool conifer forest

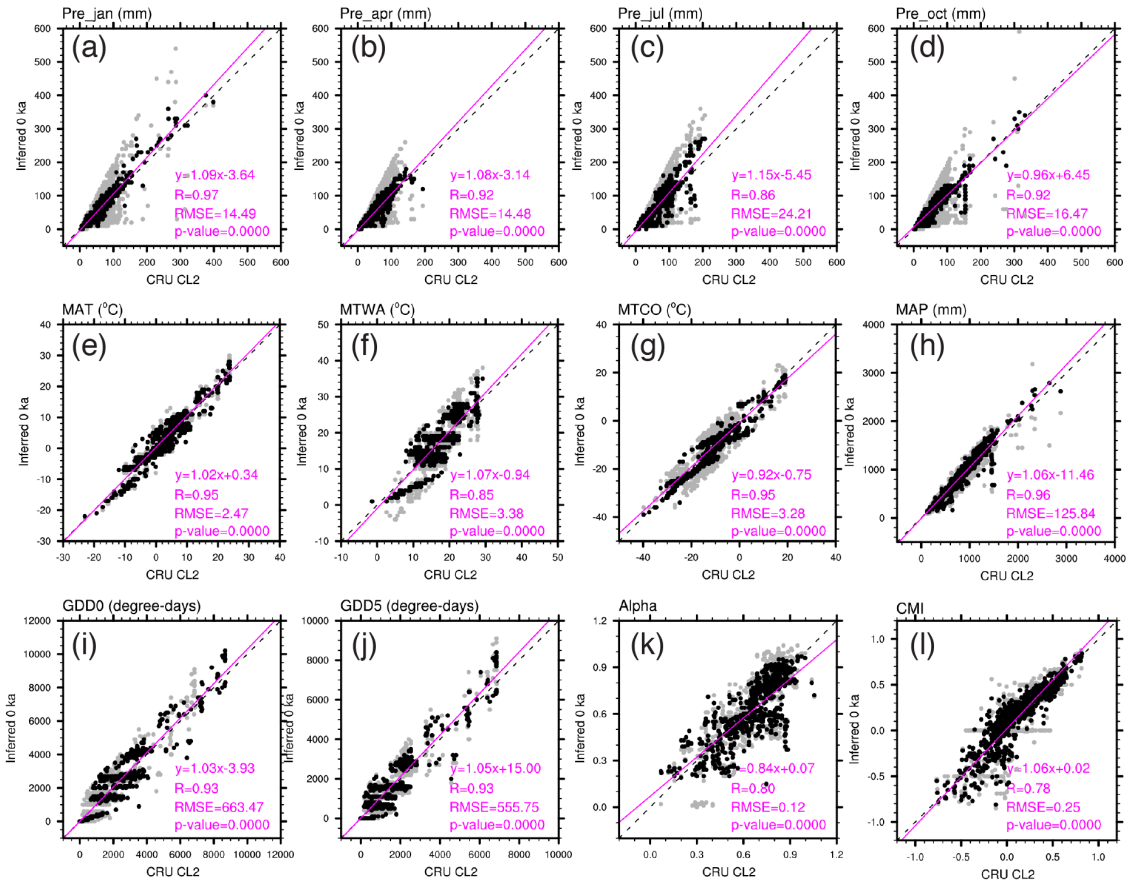

Figure S4.3. Correlation between observed climates and simulated values by IMIFM with BIOME4 in North America at modern condition: a) January precipitation b) April precipitation, c) July precipitation, d) October precipitation, e) mean temperature coldest month (MTCO), f) mean temperature warmest month (MTWA), g) growing degree-days above 0°C (GDD0), h) growing degree-days above 5°C (GDD5), i) mean annual temperature (MAT), and j) mean annual precipitation (MAP). The gray dot is mode and the black dot is median values at each sample site. The dash line is the 1:1 line, and the solid magenta line is least-squares regression. R is correlation coefficient, and RMSE is the root mean square error of the residuals.

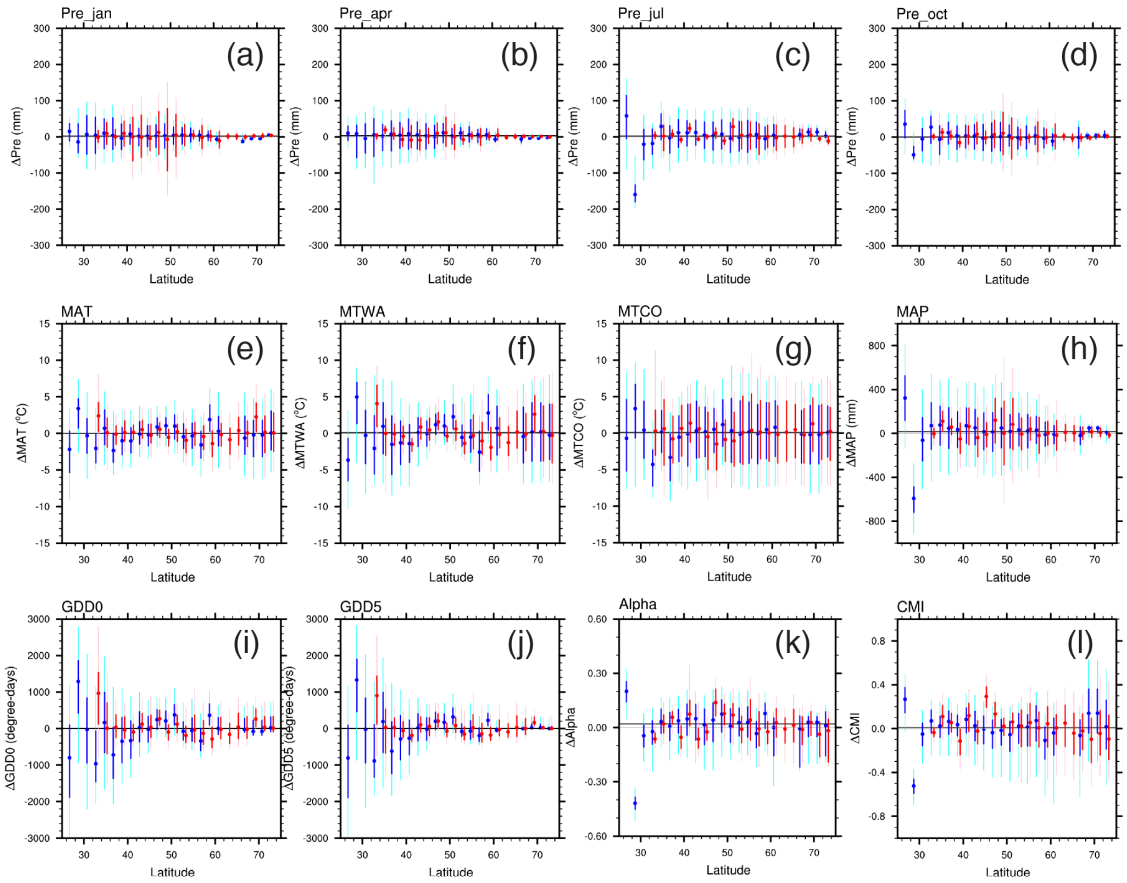

Figure S4.4. Latitudinal cross section of IMIFM simulated MH climate values using BIOME4: a) January precipitation, b) April precipitation, c) July precipitation, d) October precipitation, e) mean annual temperature, f) mean temperature warmest month, g) mean temperature coldest month, h) mean annual precipitation, i) growing degree-days 0°C base, j) growing degree-days 5°C base, k) alpha (the ratio of actual to potential evapotranspiration), and l) climate moisture index (the ratio annual precipitation to annual potential evapotranspiration) at 6ka. Blue represents sites of North America east of 105°W, and red for west of 105°W. The thin line extends to the 5th and 95th percentiles of reconstructed values and the bold line extends to the 25th and 75th percentiles interquartile intervals, and dot indicates the median value. The black line shows the North American area-average value.

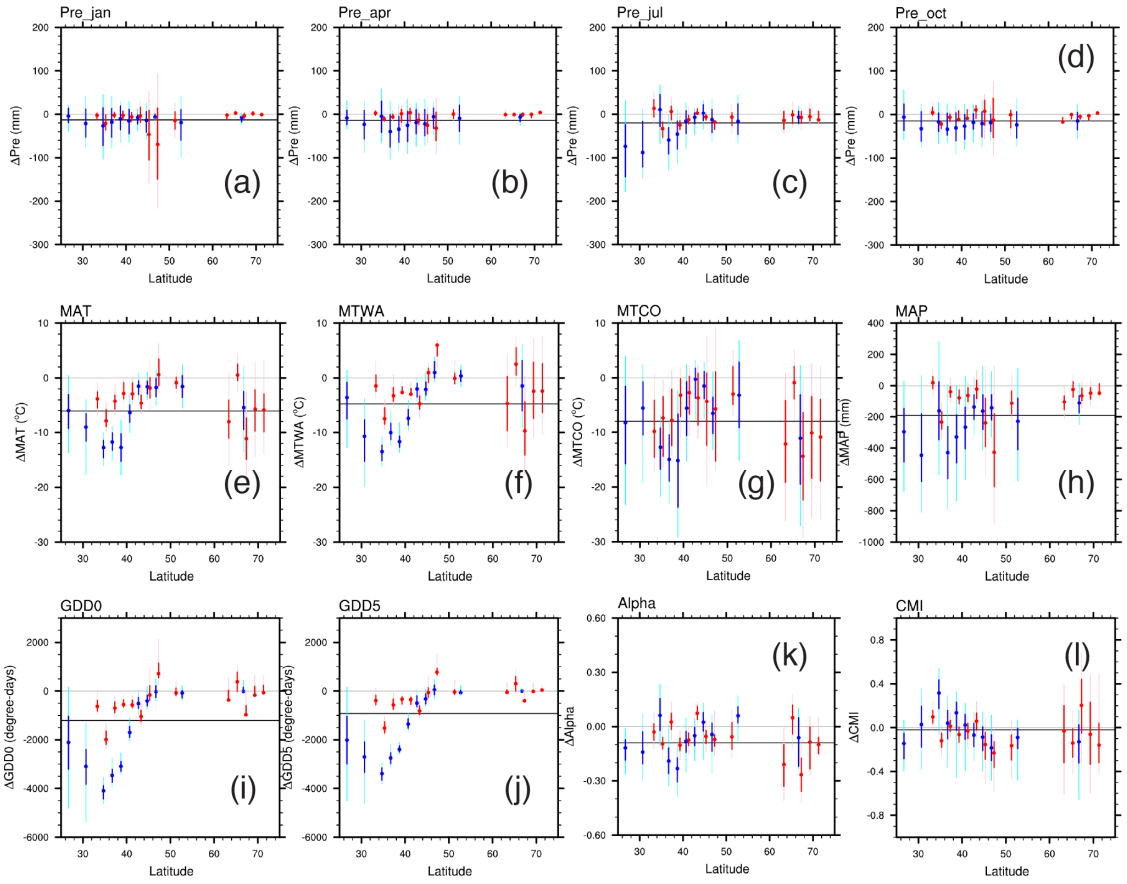

Figure S4.5. Latitudinal cross section of IMIFM simulated LGM climate values using BIOME4: a) January precipitation, b) April precipitation, c) July precipitation, d) October precipitation, e) mean annual temperature, f) mean temperature warmest month, g) mean temperature coldest month, h) mean annual precipitation, i) growing degree-days 0°C base, j) growing degree-days 5°C base, k) alpha (the ratio of actual to potential evapotranspiration), and l) climate moisture index (the ratio annual precipitation to annual potential evapotranspiration) at 21ka. Blue represents sites of North America east of 105°W, and red for west of 105°W. The thin line extends to the 5th and 95th percentiles of reconstructed values and the bold line extends to the 25th and 75th percentiles interquartile intervals, and dot indicates the median value. The black line shows the North American area-average value.

APPENDIX D

SUPPLEMENTARY INFORMATION ABOUT BIOME5 (BETA VERSION)

Izumi, K., Department of Geography, University of Oregon, Eugene, Oregon 97403, USA

This appendix contains supplementary information (SI) for a new biogeography model, BIOME5 (beta version) used in this research. BIOME5 has been developed from BIOME4 for better reconstruction of paleo-vegetation and its related climate, and BIOME5 (beta version), which uses the two-layer soil characteristic and the same biome assignment scheme as BIOME4, was adopted for the inverse-modeling through iterative forward-modeling (IMIFM) approach in order to allow a simple comparison between two models.

BIOME4

BIOME4 (Kaplan et al. 2003) is an equilibrium terrestrial biogeography model, and simulates the geographic distribution and quantitative properties of vegetation based on climate (temperature, precipitation, sunshine, and absolute minimum temperature), soil physical properties (water holding capacity and percolation rate), insolation, and atmospheric CO_2 concentration. BIOME4 simulates 27 major potential natural vegetation types (biomes) that represent global plant communities with distinctive composition, phenology, and climate regimes.

The model is run globally at a 0.5° resolution, using gridded climate data at that resolution. (In its original applications, BIOME4 model was tuned to a gridded long-tern mean climatology for the late 20th century, CLIMATE 2.2 (Leemans and Cramer 1991), but those data are no longer available.) The model simulates 13 plant functional types

(PFTs; table S5.1) representing physiologically distinct plant-species classes. Each PFT is assigned absolute bioclimatic limits which determine whether or not its net primary productivity (NPP) is calculated for a given grid cell. BIOME4 then simulates competition among PFTs as a function of relative NPP and uses an optimization algorithm to calculate the maximum sustainable leaf area (LAI) of each PFT and its associated NPP. PFT-specific parameters determine the sensitivity of each PFT to changes in environment. The BIOME4 separately calculates gross primary productivity (GPP) and autotrophic respiration (i.e. growth respiration and maintenance respiration), and the NPP is defined as the difference between GPP and autotrophic respiration.

Table S5.1. BIOME4 plant functional types

PFT #	Climate tolerance	Leaf form	Phenology	Life form /photo_path
1	Tropical	Broadleaf	Evergreen	Trees / C3
2	Tropical	Broadleaf	Raingreen	Trees / C3
3	Temperate	Broadleaf	Evergreen	Trees / C3
4	Temperate	Broadleaf	Summergreen	Trees / C3
5	Temperate	Needleleaf	Evergreen	Trees / C3
6	Boreal	Needleleaf	Evergreen	Trees / C3
7	Boreal	Broadleaf	Summergreen	Trees / C3
8	Temperate		Raingreen & Summergreen	Grasses / C3 & C4
9	Tropical		Raingreen	Grasses / C3 & C4
10	Tropical/Temperate	Needleleaf?	Evergreen	Shrubs / C3 & C4
11	Arctic	Needleleaf?	Evergreen	Shrubs / C3
12	Arctic		Summergreen	Grasses / C3
13	Arctic		Evergreen	Lichen & Forb / C3

The woody PFT (PFT# 1-7 in Table S5.1) that achieves the maximum annual NPP (at its optimized LAI) is generally considered as the dominant on each grid cell. The most important process in BIOME4 is the calculation of the maximum annual NPP because this value is used to identify the dominant PFT and biome at each cell. Since its publication (Kaplan et al. (2003)), new global-scale observational datasets such as gross primary productivity (GPP) and NPP, have become available, and so I began by comparing BIOME4 output with available benchmarking datasets (e.g. Kelley et al. 2013). Although the result will be described hereinafter in more detail, BIOME4 clearly overestimates GPP and NPP and underestimates atmospheric respiration. As mentioned

before, BIOME4 simulates NPP as the difference between GPP and autotrophic respiration, and the error could lead to biased biome simulations under different climate and atmospheric CO_2 concentration because each simulated biome is based on its NPP. (Because the BIOME4 vegetation distribution was tuned under modern condition, the simulated modern biome distribution captures the features of observed global vegetation, but that is no guarantee that the model will correctly simulate paleovegetation.)

BIOME5

BIOME5 (Izumi et al. in prep) has been developed from BIOME4 for use in making paleoclimate reconstructions. For climate input values the BIOME5 model is tuned to the updated modern climatology (CRU TS3.21; Harris et al. 2014) and modified to include snow-moisture accounting and to use a multi-layer soil characteristic data set (IGBP-DIS). The model includes several new plant functional types (PFTs; Table S5.2) to improve the representation of non-woody vegetation types, particularly in arid regions. The parameters of the carbon flux model have been modified in line with MODIS (MOD17A3) GPP and NPP data (Zhao et al. 2005; Zhao and Running 2010).

Table S5.2. BIOME5 plant functional types

PFT #	Climate tolerance	Leaf form	Phenology	Life form /photo_path
1	Tropical	Broadleaf	Evergreen	Trees / C3
2	Tropical	Broadleaf	Raingreen	Trees / C3
3	Temperate	Broadleaf	Evergreen	Trees / C3
4	Temperate	Broadleaf	Summergreen	Trees / C3
5	Temperate	Needleleaf	Evergreen	Trees / C3
6	Boreal	Needleleaf	Evergreen	Trees / C3
7	Boreal	Broadleaf	Summergreen	Trees / C3
8	Boreal	Needleleaf	Summergreen	Trees / C3
9	Temperate	Broadleaf	Raingreen	Shrub/C3 & C4
10	Temperate	Broadleaf	Summergreen	Shrub/C3 & C4
11	Boreal	Broadleaf	Summargreen	Shrub/C3
12	Arctic	Broadleaf	Summergreen	Shrub/C3
13	Arctic	Broadleaf	Evergreen	Shrub/C3
14	Tropical		Raingreen	Grasses / C3 & C4
15	Temperate		Raingreen & Summergreen	Grasses / C3 & C4
16	Arctic		Summergreen	Grasses / C3
17	Arctic		Evergreen	Lichen & Forb / C3

BIOME5 beta version

Because the "inverse modeling through iterative forward-modeling" (IMIFM) approach is highly dependent on the quality of the process-based model used, I applied both BIOME4 and BIOME5 in order to compare the results and ideally decrease the dependence of the results on a particular model. In our IMIFM study, I adopted a beta version of BIOME5 that uses the two-layer soil characteristics (FAO) and the same biome assignment scheme as BIOME4 to allow a simple comparison between the two models.

Global-scale data-model comparison for BIOME4 using plant-productivity datasets

In order to diagnose in BIOME4 the particular issues that exist for the GPP and NPP calculations, I used the Moderate-resolution Imaging Spectroradiomater (MODIS) Gross/Net Primary Production (GPP/NPP) project (MOD 17, version 055) data (Zhao et al. 2005). These data are produced using a hybrid satellite remote-sensing and terrestrial ecosystem model (BIOME-BGC; Running and Hunt 1993), and are generated by the Numerical Terradynamic Simulation Group (NTSG) at the University of Montana (http://www.ntsg.umt.edu/project/mod17). Input data for MOD17 (version 055) comes from combination of satellite remote sensing and meteorological information; the NCEP/NCAR Reanalysis II for meteorology, MOD12Q1 (version 004; Type2) for land cover, and MOD15A2 (version 005) for FPAR/LAI. Unlike in the case of BIOME models (i.e. BIOME4 and BIOME5), Biome-BGC does not simulate vegetation and FPAR/LAI in this project. As a result, I consider that the MODIS GPP/NPP is based on observations in spite of utilization of BIOME-BGC.

I adopted the MODIS GPP/NPP project (MOD17A3) data as the observed data for plant productivity. GPP is the amount of carbon taken up in photosynthesis, and NPP is the net production of organic matter by plants in an ecosystem – that is, GPP reduced

by losses resulting from the respiration of the plants. Therefore, after MOD17A3 NPP is subtracted from MOD17A3 GPP, the reminder is regarded as MOD17A3 autotrophic respiration (*Ra*), the amount of carbon that returned to the atmospheric as CO_2 during plant metabolism.

BIOME4 (distribution version) has some significant issues in the calculation of plant productivity;

1. Gross primary production (GPP): compared with observations (MODIS, MOD17A3 2000-2012 mean GPP), GPP simulated by BIOME4 is overestimated under the modern climate (CRU TS 3.21, 2000-2012 mean) over the globe, in particular in the warm-temperate and temperate forest regions (Fig. S5.1). One of the causes for the overestimation is a model parameterization issue (for calculating photosynthesis rate) including the scaling parameter and temperature-inhibition function.
2. Autotrophic respiration (*Ra*: the difference between GPP and NPP): compared with observations (MODIS, MOD17A3 2000-2012 mean), *Ra* by BIOME4 is underestimated over the tropics and overestimated over the extratropics (Fig. S5.1). One of the causes for the overestimation is a model parameterization issue for calculating growth respiration and root respiration.
3. Net primary productivity (NPP): compared with observations (MODIS, MOD17A3 2000-2012 mean), NPP by BIOME4 is overestimated under the modern climate over the globe, in particular the tropical/warm-temperate/temperature forest regions (Fig. S5.1). NPP is defined as the difference GPP and *Ra*, NPP = GPP – *Ra*. Thus, overestimation of NPP is related to overestimation of GPP and/or underestimation of *Ra*.

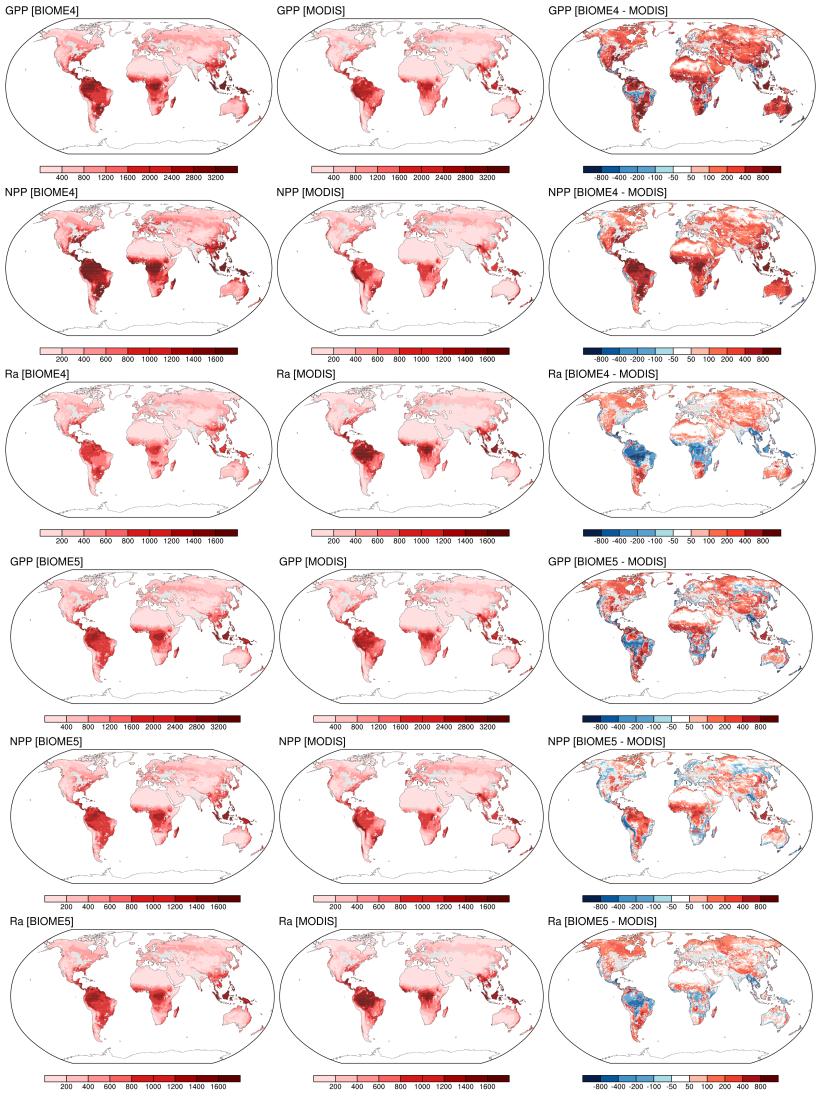

Figure S5.1. BIOME4 and BIOME5 simulated plant productivity maps: BIOME4 (top nine maps, CRU TS3.21 2000-2012 ltm, 381.6 ppm CO_2) GPP, NPP, and autotrophic respiration (left column); MODIS MOD17A3 (2000-2012 mean) GPP, NPP, and autotrophic respiration (middle column); the differences (BIOME4 – MODIS MOD17A3) of GPP, NPP, and autotrophic respiration (right column). Cropland was masked out (cropprop > 40%) with HYDE3.1, 1990-2000 mean values. BIOME5 beta (bottom nine maps, CRU TS3.21 2000-2012 ltm, 381.6 ppm CO_2) GPP, NPP, and autotrophic respiration (left column); MODIS MOD17A3 (2000-2012 mean) GPP, NPP, and autotrophic respiration (middle column); the differences (BIOME5 – MODIS MOD17A3) of GPP, NPP, and autotrophic respiration (right column). Cropland was masked out (cropprop > 40%) with HYDE3.1, 1990-2000 mean values.

Modification of the photosynthesis model in BIOME5

BIOME4 and BIOME5 have been developed from BIOME3. The photosynthesis scheme in BIOME3 (Haxeltine and Prentice 1996) was based on the Farquhar photosynthesis model (Farquhar et al. 1980) as simplified by (Collatz et al. 1991) for C3 photosynthesis and (Collatz et al. 1992) C4 photosynthesis. Photosynthesis is calculated as a function of the following five parameters: 1) absorbed photosynthetically active radiation (APAR), 2) leaf temperature or surface air temperature, 3) atmospheric CO_2 concentration, 4) day length, and 5) canopy conductance. These calculations are made for an averaged mid-month day and multiplied by the number of days in the month. The general photosynthesis scheme is consistent among all BIOME models.

The overestimation of the BIOME4 simulated GPP results from the calculation of the daily gross photosynthesis in the carbon-flux submodel. The inhibition function, which describes the effect of low temperatures on C3 photosynthesis, did not include the effect of high temperatures on C3 photosynthesis in BIOME4, but other vegetation models (e.g., LPJ, LPJ-GUESS, and LPX) include the feature. Thus, I modified the carbon-flux submodel. As a result, the photosynthesis rate in BIOME5 drops off as temperatures rise beyond the thermal optimum (Fig. S5.2). The new function in BIOME5 holds promise for simulating GPP over the globe. The modified GPP constrains NPP over the globe, in particular tropical to temperate regions.

Respiration in BIOME5

In BIOME4 and BIOME5, autotrophic respiration (*Ra*) is composed of maintenance respiration (*Rm*) and growth respiration (*Rg*), and they are calculated at monthly time step.

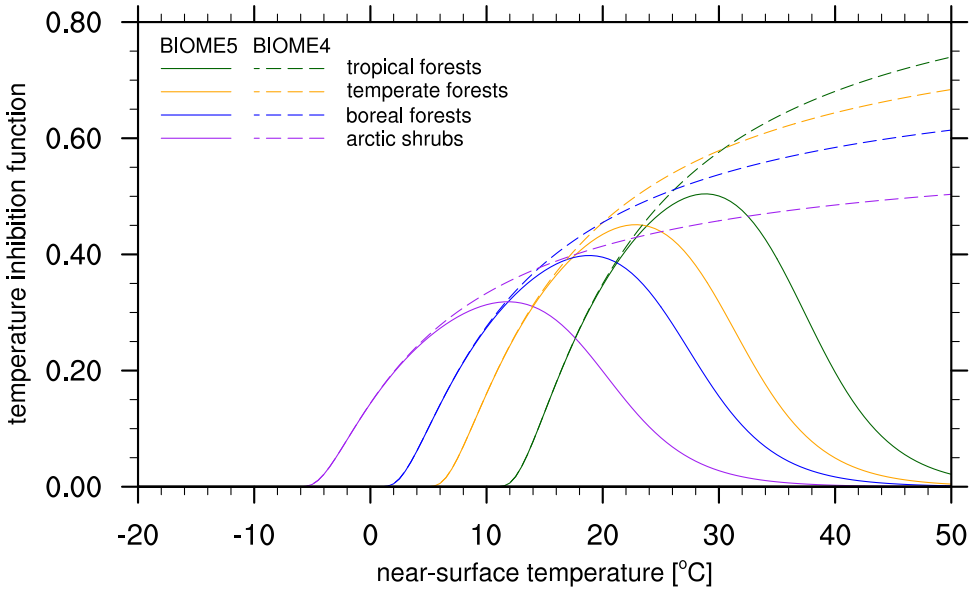

Figure. S5.2. Temperature inhibition function for each plant in BIOME4 and BIOME5. A modified temperature inhibition function for each PFT. A peak for tropical/temperate/boreal/forests is between 18°C to 30°C, and the function shows that photosynthesis rate drops off as temperatures rises above the thermal optimum.

$$R_a = R_m + R_g$$

$$R_m = R_{transport} + R_{root} + R_{leaf}$$

where

$R_{transport}$: maintenance respiration cost for transport tissues (e.g., stem and woody root sapwood)

R_{root} : root respiration

R_{leaf} : leaf respiration

The maintenance respiration cost for transport tissues ($R_{transport}$) in BIOME5 uses the same calculation method as one in BIOME4, and the leaf respiration cost (R_{leaf}) in BIOME5 is calculated with a traditional method (i.e. BIOME3 scheme) taking leaf longevity into consideration. The calculation method of root respiration (R_{root}) and growth respiration (R_g) is different between the two models. Although R_{root} depends on LAI (Fig. S5.3) and the surface air temperature does not directly influence R_{root} in

BIOME4, Burton et al. (2008) showed the close relationship between mean annual R_{root} and mean annual temperature (i.e. an increase in forest ecosystem annual root respiration with increasing mean annual temperature) in forest ecosystems. Consequently, I modified this function in line with (Burton et al. 2008) for tropical/warm-temperate/temperate/boreal vegetation types (Fig. S5.4), but used the unmodified function in BIOME4 for Arctic vegetation.

After maintenance respiration (R_m) is subtracted from GPP, 2% of the remainder is taken as growth respiration (R_g) in BIOME4. Because this parameter (2%) is clearly too low, I adopted a value 20% (a general value for vegetation models) for the calculation in BIOME5. As a result, R_{root} and R_g in BIOME5 generally become enlarged over the tropical/warm-temperate/temperature regions. These modified R_a values constrain NPP over the globe, in particular tropical to temperate regions.

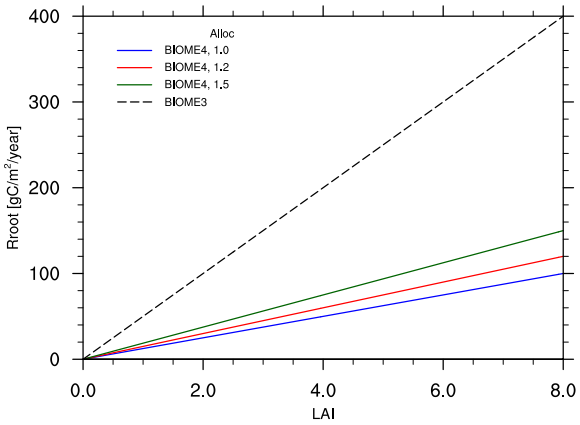

Figure S5.3. The relationship between root respiration (R_{root}) and LAI in BIOME4

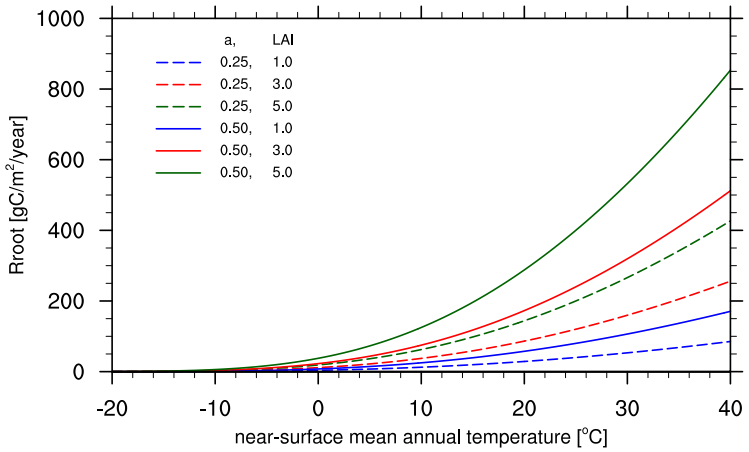

Figure S5.4. The relationship between root respiration (R_{root}) and annual mean temperature in BIOME5

Evapotranspiration and moisture index in BIOME5

BIOME4 (distribution version) also has some issues regarding the definition of evapotranspiration and moisture index. The plant-available moisture index (α) in BIOME4 is calculated as the ratio actual to equilibrium evapotranspiration (AET/EET), and the calculation of these evapotranspiration is based on Haxeltine and Prentice (1996). The α in BIOME4 can exceed 1.0 in some tropical regions (Fig. S5.5). In BIOME5, I defined the α as the ratio actual to potential evapotranspiration (AET/PET) ranging from 0 = extremely dry to 1 = extremely wet based on Thornthwaite and Mather (1955) and (Thornthwaite et al. 1957). The calculation of evapotranspiration in BIOME5 is also based on Haxeltine and Prentice (1996). PET is the amount of water that would be evaporated and transpirated if there were sufficient water available, and AET is the amount of water that is actually removed from a surface because of the evapotranspiration and transpiration. Thus, AET should be equal PET (i.e. α = 1) when there is ample water.

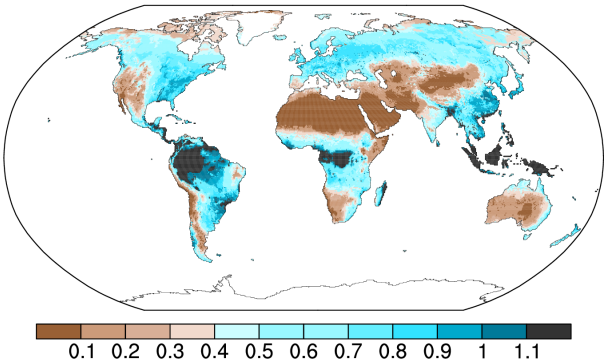

Figure S5.5. BIOME4 plant-available moisture index under modern climatology

In BIOME4, PET is equal to the equilibrium evapotranspiration (EET), and AET is estimated by multiplying EET by the Priestly-Taylor coefficient, the fraction of surface moisture available for evaporation in the Priestly-Taylor equation, depending on surface conditions (α_{surf}). Therefore, if α_{surf} is more than 1.0, the moisture index is more than 1.0. This definition of PET in BIOME4 is different from some previous research. Priestley and Taylor (1972) showed that PET is can be determined by multiplying EET with Priestly-Taylor coefficient, α (1.26 for wet surfaces) in a radiational-based PET model. Priestley and Taylor (1972) basically applied the equation to oceanic and saturated land surfaces (with no modification for advection), and the equation largely reflects the equilibrium evaporation or the evaporation from a wet surface into saturated air. This equilibrium connects energy at the surface to the air above it (called the convective boundary layer) so that AET, sensible heat flux, air temperature, and air humidity all balance around an α constant of 1.26 (Raupach 2001). Hobbins et al. (2001) suggested that PET can be estimated by multiplying EET by an α equal to 1.32. EET describes the evaporative equilibrium for evapotranspiration into a closed vessel and presents the lower limit of evapotranspiration from wet surfaces. PET, which presents the upper limit of evapotranspiration from wet surfaces, can be higher than EET because of parts of the dynamics of the planetary boundary layer (Haque 2003; Hobbins et al. 2001). Thus, I used α =1.26 for computation of PET in BIOME5.

In order to modify the α within an appropriate range, I also need to consider α_{sur} in calculating AET. In BIOME4 and 5, AET is modeled as the lesser of a plant-controlled supply function (S) and atmosphere-controlled demand function (D):

$$AET = \min\{S, D\}$$

Transpirational supply (S) is determined by the maximum transpiration rate that can be sustained under well-watered conditions (E_{max}, PFT-specific parameter), and declines lineally with relative soil moisture (Wr)

$$S = E_{\max} Wr$$

Wr gives the ratio between current soil water content and plant-available water capacity (the texture-dependent difference between field capacity (the upper limit of water storage in the soil) and wilting point (the lower limit of water storage in the soil)). The soil is treated as a simple bucket consisting of two or more than two layers with fixed thickness. The Wr ratio is computed for both soil layers by weighting their relative soil water contents with the fraction of roots present in the respective layer.

Atmospheric demand (D) represents unstressed transpiration, which occurs when stomatal opening is not limited by reduced water potential in the plant. In Monteith (1995), daily demand is either an "exponential" or a "hyperbolic" function of canopy conductance (the sum of stomatal conductance of all leaves for a given PFT):

$$D = E_q \alpha_m \left[1 - \exp\left(-g/g_c\right)\right], \quad 1') \ \alpha_{surf} = \alpha_m \left[1 - \exp\left(-g/g_c\right)\right]$$

$$D = E_q \alpha_m \Big/ \left[1 + \left(g_c/g\right)\right], \quad 2') \ \alpha_{surf} = \alpha_m \Big/ \left[1 + \left(g_c/g\right)\right]$$

where
E_q: daily equilibrium evapotranspiration (EET) rate
α_m: a maximum Priestley-Taylor coefficient,
g_c: a scaling conductance (it depends on conditions at the top of the CBL*)
g: a surface conductance of vegetation & canopy
(*CBL: the Convective Boundary Layer)

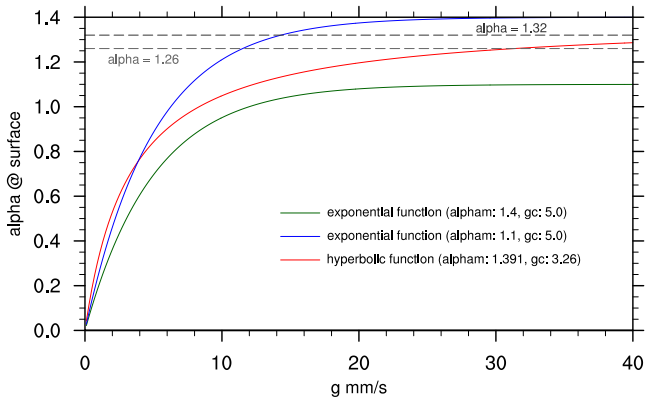

Figure S5.6. The relationship between Priestley-Taylor coefficient (α_{surf}) and canopy conductance (g)

In BIOME4, the exponential function of canopy conductance is adopted for *D*. α_m (=1.4) and g_c (=5.0) was defined following Monteith (1995) (Fig. S5.6). In BIOME5, the hyperbolic function of canopy conductance was adopted for D. α_m (=1.391) and g_c (=3.26) is defined following (Huntingford and Monteith 1998) in parallel with other vegetation models (e.g. LPJ-GUESS and LPX) (Fig. S5.6).

Demand approximates $E_q\alpha_m$ when the canopy is dry and the potential canopy conductance (g) that can be achieved when there is no water limitation – tends to infinity. The potential canopy conductance (g) is directly related to the photosynthesis rate (details in Haxeltine and Prentice 1996).

Comparison of BIOME5 (beta version) and BIOME4 with benchmark data sets

Simulated NPP, GPP, autotrophic respiration (R_a), and runoff by BIOME4 and BIOME5 (beta) were compared with observations (NPP, GPP, and Ra from MODIS17A3; runoff from Fekete et al. 2002). Global-scale and regional-scale (Asia, North America, South America, Europe, Africa and Middle East, and Oceania) values were separately compared and Taylor diagrams (Taylor 2001) were used to provide a visual framework for comparing model results to observations (Fig. S5.7). In Taylor

diagrams, the performance of an individual simulation (relative to some observational or standard "reference" data set) is summarized by the location of a point on the diagram where the distance from the point to the location on the x-axis identified as "REF" (i.e. across the green contours on the diagram) is proportional to the centered root-mean-square (RMS) difference between the simulated and observed pattern while the radial distance of the point from the origin is proportional to the standard deviation of the simulated pattern. The correlation between the two fields is given by the azimuthal position of each point. Points closer to both the "REF" point and line thus represent simulations that are better in terms of the amplitude of the simulations than points farther away.

Global-scale simulated GPP, NPP, R_a by BIOME5 (beta) show better agreement in amplitude (the points plot closer to the reference observations (REF)) than do the simulations of these variables by BIOME4, while the simulation of runoff does not change much between models (Fig. S5.8). Although the amplitude changes in BIOME5 (beta) are better than the ones in BIOME4, the spatial patterns of all variables do not change much (i.e. there are similar spatial patterns between BIOME4 and BIOME5 (beta)). While regional scale values also show the same trend (improvement) as global one, particularly Asia, North America, South America, and Africa and Middle East, BIOME5 (beta) plant productivity and runoff were not improved in Europe and Oceania regions (Fig. S5.7).

In addition, I compare simulated vegetation/biome (with 1961-1990 long term mean climate, 331 ppm CO_2; Fig. S.5.10 and S5.11) with observed tree-cover data (Fig. 9: ISLSCP II vegetation continuous fields; DeFries and Hansen 2009). The observed data sets provide separate information on life form, leaf type and leaf phenology at 0.5° resolution for 1992-1993. I defined the observed target tree cover at each grid as in Table S5.3). I used the Kappa statistic for comparison of simulated tree cover with the observed. BIOME4 vegetation distribution was tuned under modern condition in order to

capture the features of observed global vegetation. Both BIOME4 (Fig. S5.10) and BIOME5 (beta) (Fig. S5.11) show almost same kappa statistics, and thus BIOME5 simulates vegetation adequatly, in particular forests, for biogeographic research and paleovegetation reconstructions.

Table S5.3. The classification system for DeFries and Hansen tree cover data

Tree types	
Mixed forest	evergreen >10%, deciduous>10%, needleleaf>10%, broadleaf>10%, and herbaceous<60%
Deciduous broadleaf forest	deciduous>20%, broadleaf>20%, herbaceous<60%, and not mixed forest
Deciduous needleleaf forest	deciduous>20%, needleleaf>20%, herbaceous<60%, and not mixed forest
Evergreen broadleaf forest	evergreen >20%, broadleaf>20%, herbaceous<60%, and not mixed forest
Evergreen needleleaf forest	evergreen>20%, needleleaf>20%, herbaceous<60%, and not mixed forest

The comparison of BIOME 4 and BIOME5 (beta) outputs with the benchmarking datasets shows the following features of BIOME5 (beta);

1. BIOME5 plant productivity measures such as GPP, NPP, and autotrophic respiration are better in terms of values than in BIOME4.
2. The spatial patterns of the plant productivity are similar between BIOME4 and BIOME5 (beta).
3. The amplitude and spatial pattern of runoff in BIOME5 (beta) is similar the to one in BIOME4.
4. The spatial pattern of tree-cover is similar between BIOME4 and BIOME5 (beta).

Overall, BIOME5 (beta) simulates plant-productivity variables better than BIOME4 without any loss of skill in simulating vegetation or runoff patterns.

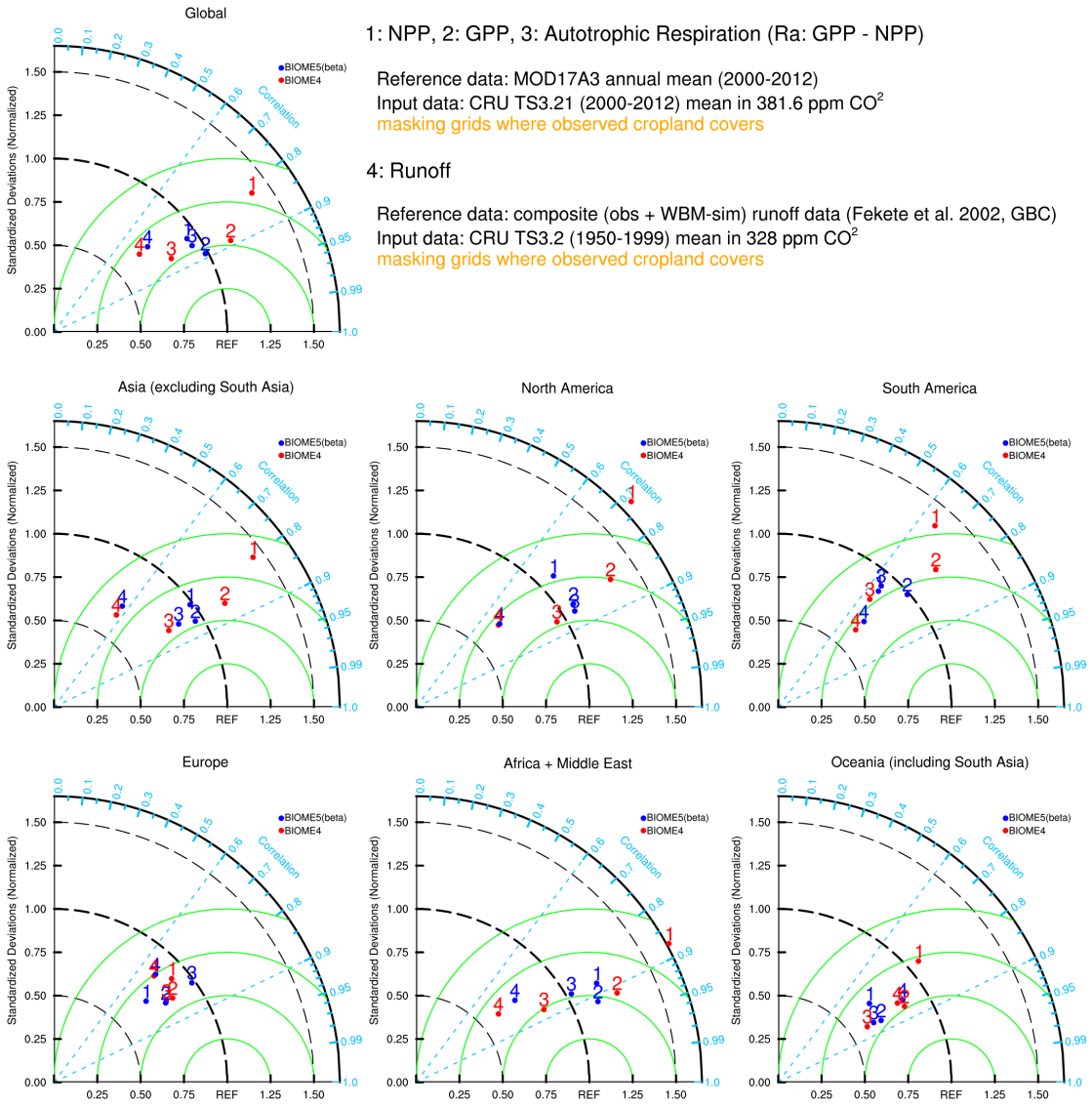

Figure S5.7. Data-model comparison about plant productivity and runoff: Taylor diagrams display normalized amplitudes and spatial patterns between simulations and observations about GPP, NPP, autotrophic respiration, and runoff. The centered root-mean-square (RMS) difference between the simulated and observed pattern is proportional to the distance to the point on the x-axis identified as "REF" (green contours). The standard deviation of the simulated pattern is proportional to the radial distance from "REF" bold line. The correlation between the two fields is given by the azimuthal position of the each point.

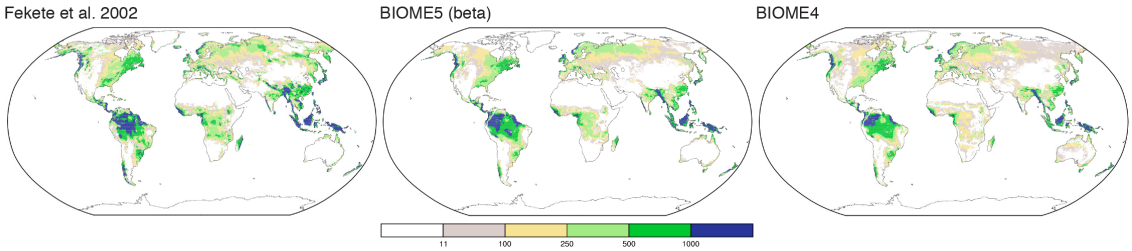

Figure S.5.8. Observed and simulated (BIOME5 (beta) and BIOME4) runoff maps.

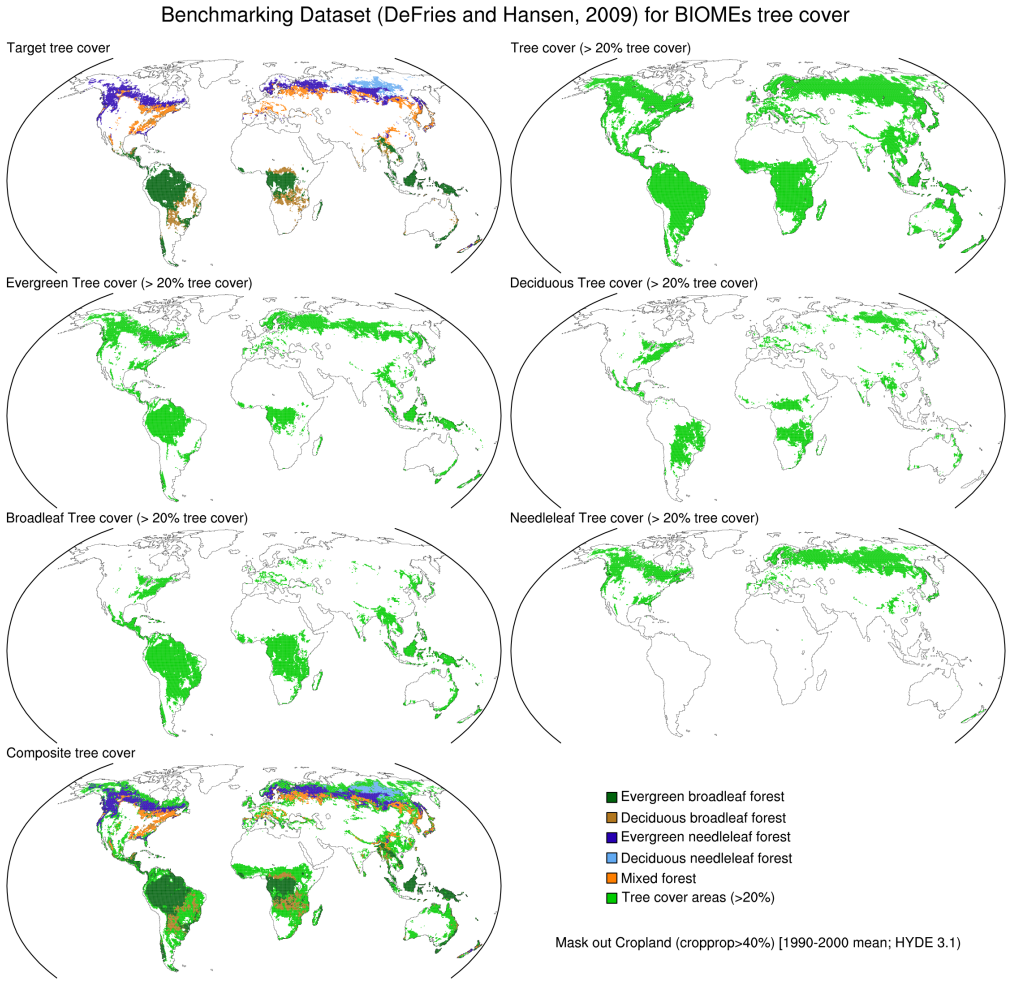

Figure S5.9. Observed tree cover maps: ISLSCP II continuous vegetation based on a snapshot for 1992-1993 (DeFries and Hansen, 2009) includes tree cover, evergreen tree cover, deciduous tree cover, broadleaf tree cover, needleleaf tree cover, and their composite tree cover.

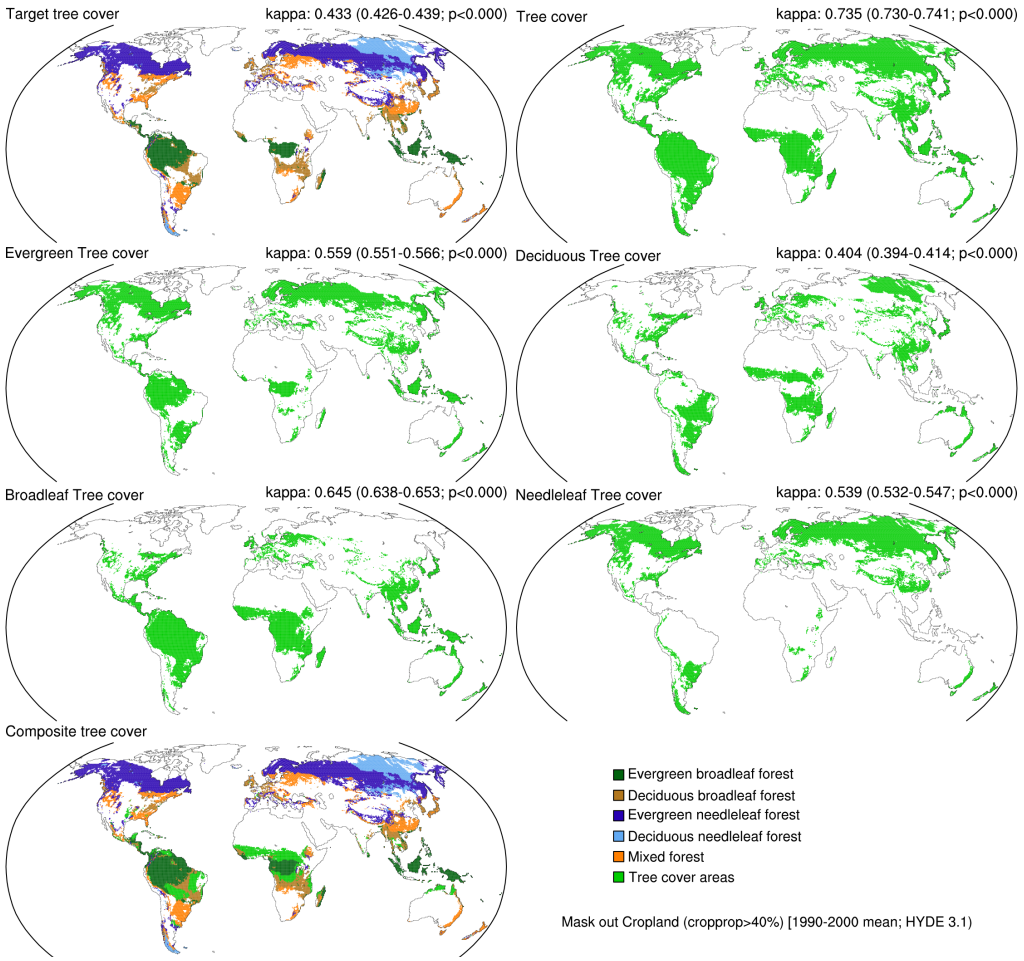

Figure S5.10. BIOME4 simulated tree cover maps.

CO_2 Sensitivity of BIOME4 and BIOME5 (beta)

I also explored the response of the simulated vegetation to the changes in CO_2 using BIOME4 and BIOME5 (beta) (Fig. S5.12). In order to explore the response, I run both models using the same modern climate but the varying CO_2 concentration within a range. In the tropics, the variations in CO_2 can result in large changes in the relative importance of grasslands and dry shrublands and forests (Fig. S5.12). The impact on extratropical vegetation is less, but changes in CO_2 can lead to appreciable shifts in the

relative abundance of forest and non-forest vegetation types (Fig. S5.12). In other words, as atmospheric CO_2 decreases, the forest covers decease. The changes lead to decreases in global NPP and GPP. Both BIOME4 and BIOME5 (beta) show the similar responses to CO_2 changes (Fig. S5.12).

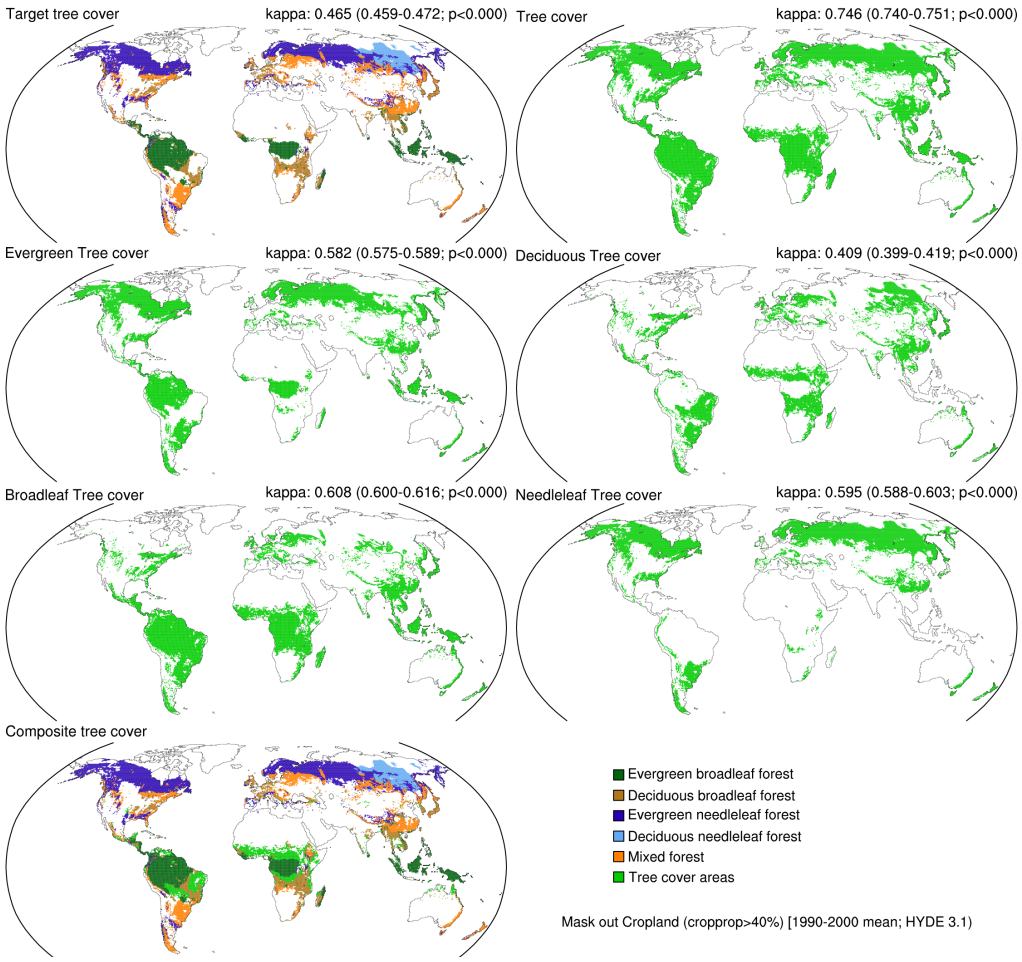

Figure S5.11. BIOME5 (beta) simulated tree cover maps.

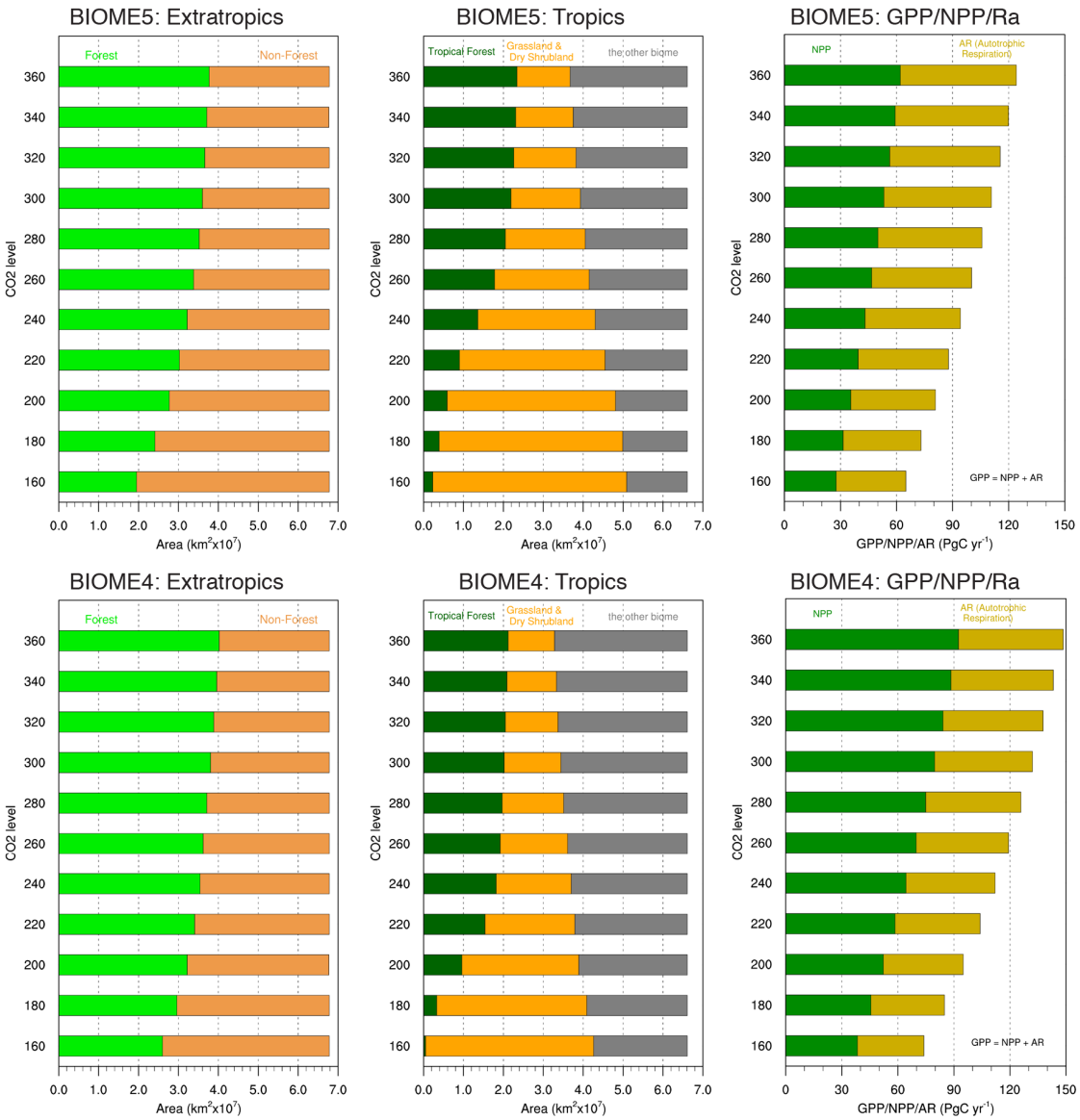

Figure S5.12. The responses of BIOME5 and BIOME4 vegetation to changes in CO_2 concentration: simulated changes in the area of extratropical and tropical biomes, and changes in plant productivity as a result of the effect of changes in CO_2 on the competition between C3 and C4 plants under modern climate conditions. In these simulations with BIOME5 (beta) and BIOME4, atmospheric CO_2 levels have been systematically varied between 160 ppmv and 360 ppmv, but climate (CRU TS3.21 1961-1990) was kept constant.

REFERENCES CITED

Chapter I

Bartlein P (1997) Past environmental changes: Characteristic features of Quaternary climate variations. In: Huntley B, Cramer W, Morgan A, Prentice H, Allen JM (eds) Past and Future Rapid Environmental Changes, vol 47. NATO ASI Series. Springer Berlin Heidelberg, pp 11-29. doi:10.1007/978-3-642-60599-4_2

Bartlein PJ, Anderson PM, Edwards ME, McDowell PF (1991) A framework for interpreting paleoclimatic variations in Eastern Beringia. Quaternary International 10–12 (0):73-83. doi:http://dx.doi.org/10.1016/1040-6182(91)90041-L

Bartlein PJ, Harrison SP, Brewer S, Connor S, Davis BAS, Gajewski K, Guiot J, Harrison-Prentice TI, Henderson A, Peyron O, Prentice IC, Scholze M, Seppa H, Shuman B, Sugita S, Thompson RS, Viau AE, Williams J, Wu H (2011) Pollen-based continental climate reconstructions at 6 and 21 ka: a global synthesis. Climate Dynamics 37 (3-4):775-802. doi:10.1007/s00382-010-0904-1

Bartlein PJ, Hostetler SW (2003) Modeling paleoclimates. In: A.R. Gillespie SCP, Atwater BF (eds) Developments in Quaternary Sciences, vol Volume 1. Elsevier, pp 565-584. doi:http://dx.doi.org/10.1016/S1571-0866(03)01027-3

Bartlein PJ, Prentice IC, Webb T (1986) Climatic response surfaces from pollen data for some eastern North-American taxa. In: Journal of Biogeography, vol 13. vol 1. pp 35-57. doi:10.2307/2844848

Braconnot P, Harrison SP, Kageyama M, Bartlein PJ, Masson-Delmotte V, Abe-Ouchi A, Otto-Bliesner B, Zhao Y (2012) Evaluation of climate models using palaeoclimatic data. Nature Climate Change 2 (6):417-424. doi:10.1038/nclimate1456

Braconnot P, Otto-Bliesner B, Harrison S, Joussaume S, Peterchmitt JY, Abe-Ouchi A, Crucifix M, Driesschaert E, Fichefet T, Hewitt CD, Kageyama M, Kitoh A, Laine A, Loutre MF, Marti O, Merkel U, Ramstein G, Valdes P, Weber SL, Yu Y, Zhao Y (2007a) Results of PMIP2 coupled simulations of the Mid-Holocene and Last Glacial Maximum - Part 1: experiments and large-scale features. Climate of the Past 3 (2):261-277

Braconnot P, Otto-Bliesner B, Harrison S, Joussaume S, Peterchmitt JY, Abe-Ouchi A, Crucifix M, Driesschaert E, Fichefet T, Hewitt CD, Kageyama M, Kitoh A, Loutre MF, Marti O, Merkel U, Ramstein G, Valdes P, Weber L, Yu Y, Zhao Y (2007b) Results of PMIP2 coupled simulations of the Mid-Holocene and Last Glacial Maximum - Part 2: feedbacks with emphasis on the location of the ITCZ and mid- and high latitudes heat budget. Climate of the Past 3 (2):279-296

Bradley RS (2014) Paleoclimatology: Reconstructing Climates of the Quaternary. Elsevier/Academic Press, San Diego

Broccoli AJ, Manabe S (1987) The influence of continental ice, atmospheric CO2, and land albedo on the climate of the last glacial maximum. Climate Dynamics 1 (2):87-99. doi:10.1007/bf01054478

Claussen M, Mysak LA, Weaver AJ, Crucifix M, Fichefet T, Loutre MF, Weber SL, Alcamo J, Alexeev VA, Berger A, Calov R, Ganopolski A, Goosse H, Lohmann G, Lunkeit F, Mokhov, II, Petoukhov V, Stone P, Wang Z (2002) Earth system models of intermediate complexity: closing the gap in the spectrum of climate system models. Climate Dynamics 18 (7):579-586. doi:10.1007/s00382-001-0200-1

CLIMAP Project Members (1976), The surface of the ice-age earth. Science 191:1131-1137.

CLIMAP Project Members (1981), Seasonal reconstructions of the earth's at the Last Glacial Maximum, Geol. Soc. Am. Map Chart Ser., MC-36:1-18.

COHMAP Members (1988) Climatic changes of the last 18,000 years: Observations and model simulations. Science 241 (4869):1043-1052. doi:10.1126/science.241.4869.1043

Cowling SA, Sykes MT (1999) Physiological significance of low atmospheric CO2 for plant-climate interactions. Quaternary Research 52 (2):237-242. doi:10.1006/qres.1999.2065

Daniau AL, Bartlein PJ, Harrison SP, Prentice IC, Brewer S, Friedlingstein P, Harrison-Prentice TI, Inoue J, Izumi K, Marlon JR, Mooney S, Power MJ, Stevenson J, Tinner W, Andric M, Atanassova J, Behling H, Black M, Blarquez O, Brown KJ, Carcaillet C, Colhoun EA, Colombaroli D, Davis BAS, D'Costa D, Dodson J, Dupont L, Eshetu Z, Gavin DG, Genries A, Haberle S, Hallett DJ, Hope G, Horn SP, Kassa TG, Katamura F, Kennedy LM, Kershaw P, Krivonogov S, Long C, Magri D, Marinova E, McKenzie GM, Moreno PI, Moss P, Neumann FH, Norstrom E, Paitre C, Rius D, Roberts N, Robinson GS, Sasaki N, Scott L, Takahara H, Terwilliger V, Thevenon F, Turner R, Valsecchi VG, Vanniere B, Walsh M, Williams N, Zhang Y (2012) Predictability of biomass burning in response to climate changes. Global Biogeochemical Cycles 26. doi:10.1029/2011gb004249

Farquhar GD (1997) Carbon dioxide and vegetation. Science 278 (5342):1411-1411. doi:10.1126/science.278.5342.1411

Gates WL (1976) Modeling the ice-age climate. SIGSIM Science 191(4232):1138-44. doi:10.1145/1102746.1102757

Gonzales LM, Williams JW, Grimm EC (2009) Expanded response-surfaces: a new method to reconstruct paleoclimates from fossil pollen assemblages that lack modern analogues. Quaternary Science Reviews 28 (27-28):3315-3332. doi:10.1016/j.quascirev.2009.09.005

Guiot J, Torre F, Jolly D, Peyron O, Boreux JJ, Cheddadi R (2000) Inverse vegetation modeling by Monte Carlo sampling to reconstruct palaeoclimates under changed precipitation seasonality and CO2 conditions: application to glacial climate in Mediterranean region. Ecological Modelling 127 (2-3):119-140. doi:10.1016/s0304-3800(99)00219-7

Guiot J, Wu HB, Garreta V, Hatte C, Magny M (2009) A few prospective ideas on climate reconstruction: from a statistical single proxy approach towards a multi-proxy and dynamical approach. Climate of the Past 5 (4):571-583

Harrison SP (2013) Paleoclimate Modeling | Data–Model Comparisons. In: Elias SA, Mock CJ (eds) Encyclopedia of Quaternary Science (Second Edition). Elsevier, Amsterdam, pp 135-146. doi:http://dx.doi.org/10.1016/B978-0-444-53643-3.00007-8

Haywood AM, Dowsett HJ, Otto-Bliesner B, Chandler MA, Dolan AM, Hill DJ, Lunt DJ, Robinson MM, Rosenbloom N, Salzmann U, Sohl LE (2010) Pliocene Model Intercomparison Project (PlioMIP): experimental design and boundary conditions (Experiment 1). Geosci Model Dev 3 (1):227-242. doi:10.5194/gmd-3-227-2010

Haywood AM, Dowsett HJ, Robinson MM, Stoll DK, Dolan AM, Lunt DJ, Otto-Bliesner B, Chandler MA (2011) Pliocene Model Intercomparison Project (PlioMIP): experimental design and boundary conditions (Experiment 2). Geosci Model Dev 4 (3):571-577. doi:10.5194/gmd-4-571-2011

Izumi K, Bartlein PJ, Harrison SP (2013) Consistent large-scale temperature responses in warm and cold climates. Geophysical Research Letters 40 (9):1817-1823. doi:10.1002/grl.50350

Izumi K, Bartlein P, Harrison S (2014) Energy-balance mechanisms underlying consistent large-scale temperature responses in warm and cold climates. Climate Dynamics:1-17. doi:10.1007/s00382-014-2189-2

Jackson ST, Williams JW (2004) Modern analogs in Quaternary paleoecology: Here today, gone yesterday, gone tomorrow? Annual Review of Earth and Planetary Sciences 32:495-537. doi:10.1146/annurev.earth.32.101802.120435

Jolly D, Haxeltine A (1997) Effect of low glacial atmospheric CO2 on tropical African montane vegetation. Science 276 (5313):786-788. doi:10.1126/science.276.5313.786

Joussaume S, Taylor KE, Braconnot P, Mitchell JFB, Kutzbach JE, Harrison SP, Prentice IC, Broccoli AJ, Abe-Ouchi A, Bartlein PJ, Bonfils C, Dong B, Guiot J, Herterich K, Hewitt CD, Jolly D, Kim JW, Kislov A, Kitoh A, Loutre MF, Masson V, McAvaney B, McFarlane N, de Noblet N, Peltier WR, Peterschmitt JY, Pollard D, Rind D, Royer JF, Schlesinger ME, Syktus J, Thompson S, Valdes P, Vettoretti G, Webb RS, Wyputta U (1999) Monsoon changes for 6000 years ago: Results of 18 simulations from the Paleoclimate Modeling Intercomparison Project (PMIP). Geophysical Research Letters 26 (7):859-862. doi:10.1029/1999gl900126

Kaplan JO, Bigelow NH, Prentice IC, Harrison SP, Bartlein PJ, Christensen TR, Cramer W, Matveyeva NV, McGuire AD, Murray DF, Razzhivin VY, Smith B, Walker DA, Anderson PM, Andreev AA, Brubaker LB, Edwards ME, Lozhkin AV (2003) Climate change and Arctic ecosystems: 2. Modeling, paleodata-model comparisons, and future projections. Journal of Geophysical Research-Atmospheres 108 (D19). doi:10.1029/2002jd002559

Kim J-H, Schneider R (2004) GHOST global database for alkenone-derived 10 ka sea-surface temperatures. PANGAEA, Bremerhaven

Kohfeld KE, Harrison SP (2000) How well can we simulate past climates? Evaluating the models using global palaeoenvironmental datasets. Quaternary Science Reviews 19 (1-5):321-346. doi:10.1016/s0277-3791(99)00068-2

Kohfeld KE, Harrison SP (2001) DIRTMAP: the geological record of dust. Earth-Science Reviews 54 (1–3):81-114. doi:http://dx.doi.org/10.1016/S0012-8252(01)00042-3

Kohfeld KE, Quéré CL, Harrison SP, Anderson RF (2005) Role of Marine Biology in Glacial-Interglacial CO2 Cycles. Science 308 (5718):74-78. doi:10.1126/science.1105375

Kucera M, Rosell-Mele A, Schneider R, Waelbroeck C, Weinelt M (2005) Multiproxy approach for the reconstruction of the glacial ocean surface (MARGO). Quaternary Science Reviews 24 (7-9):813-819. doi:10.1016/j.quascirev.2004.07.017

Kutzbach JE, Guetter PJ, Behling PJ, Selin R (1993) Simulated climatic changes: Results of the COHMAP climate-model experiments. Global climates since the last glacial maximum.

Leduc G, Schneider R, Kim J-H, Lohmann G (2010) Holocene and Eemian sea surface temperature trends as revealed by alkenone and Mg/Ca paleothermometry. Quaternary Science Reviews 29 (7-8):989-1004

Li G, Harrison SP, Bartlein PJ, Izumi K, Colin Prentice I (2013) Precipitation scaling with temperature in warm and cold climates: An analysis of CMIP5 simulations. Geophysical Research Letters 40 (15):4018-4024. doi:10.1002/grl.50730

MARGO Project Members (2009) Constraints on the magnitude and patterns of ocean cooling at the Last Glacial Maximum. Nature Geoscience 2 (2):127-132. doi:10.1038/ngeo411

McGuffie K, Henderson-Sellers A (2005) Practical Climate Modelling. In: A Climate Modelling Primer. John Wiley & Sons, Ltd, pp 213-248. doi:10.1002/0470857617.ch6

Otto-Bliesner BL, Schneider R, Brady EC, Kucera M, Abe-Ouchi A, Bard E, Braconnot P, Crucifix M, Hewitt CD, Kageyama M, Marti O, Paul A, Rosell-Mele A, Waelbroeck C, Weber SL, Weinelt M, Yu Y (2009) A comparison of PMIP2 model simulations and the MARGO proxy reconstruction for tropical sea surface temperatures at last glacial maximum. Climate Dynamics 32 (6):799-815. doi:10.1007/s00382-008-0509-0

Overpeck JT, Webb T, Prentice IC (1985) Quantitative interpretation of fossil pollen spectra - dissimilarity coefficients and the method of modern analogs. In: Quaternary Research, vol 23. vol 1. pp 87-108. doi:10.1016/0033-5894(85)90074-2

Power MJ, Marlon JR, Bartlein PJ, Harrison SP (2010) Fire history and the Global Charcoal Database: A new tool for hypothesis testing and data exploration. Palaeogeography Palaeoclimatology Palaeoecology 291 (1-2):52-59. doi:10.1016/j.palaeo.2009.09.014

Prentice IC, Harrison SP (2009) Ecosystem effects of CO2 concentration: evidence from past climates. Clim Past 5 (3):297-307. doi:10.5194/cp-5-297-2009

Prentice IC, Kelley DI, Foster PN, Friedlingstein P, Harrison SP, Bartlein PJ (2011a) Modeling fire and the terrestrial carbon balance. Global Biogeochemical Cycles 25. doi:10.1029/2010gb003906

Prentice IC, Harrison SP, Bartlein PJ (2011b) Global vegetation and terrestrial carbon cycle changes after the last ice age. New Phytologist 189 (4):988-998. doi:10.1111/j.1469-8137.2010.03620.x

Prentice IC, Webb T (1998) BIOME 6000: reconstructing global mid-Holocene vegetation patterns from palaeoecological records. Journal of Biogeography 25 (6):997-1005. doi:10.1046/j.1365-2699.1998.00235.x

Rind D, Peteet D (1985) Terrestrial conditions at the Last Glacial Maximum and CLIMAP sea-surface temperature estimates: Are they consistent? Quaternary Research 24 (1):1-22. doi:http://dx.doi.org/10.1016/0033-5894(85)90080-8

Schmidt GA (2010) Enhancing the relevance of palaeoclimate model/data comparisons for assessments of future climate change. Journal of Quaternary Science 25 (1):79-87. doi:10.1002/jqs.1314

Schmidt GA, Annan JD, Bartlein PJ, Cook BI, Guilyardi E, Hargreaves JC, Harrison SP, Kageyama M, LeGrande AN, Konecky B, Lovejoy S, Mann ME, Masson-Delmotte V, Risi C, Thompson D, Timmermann A, Tremblay LB, Yiou P (2014) Using palaeo-climate comparisons to constrain future projections in CMIP5. Clim Past 10 (1):221-250. doi:10.5194/cp-10-221-2014

Schmidt GA, Jungclaus JH, Ammann CM, Bard E, Braconnot P, Crowley TJ, Delaygue G, Joos F, Krivova NA, Muscheler R, Otto-Bliesner BL, Pongratz J, Shindell DT, Solanki SK, Steinhilber F, Vieira LEA (2012) Climate forcing reconstructions for use in PMIP simulations of the Last Millennium (v1.1). Geosci Model Dev 5 (1):185-191. doi:10.5194/gmd-5-185-2012

Sitch S, Smith B, Prentice IC, Arneth A, Bondeau A, Cramer W, Kaplan JO, Levis S, Lucht W, Sykes MT, Thonicke K, Venevsky S (2003) Evaluation of ecosystem dynamics, plant geography and terrestrial carbon cycling in the LPJ dynamic global vegetation model. Global Change Biology 9 (2):161-185. doi:10.1046/j.1365-2486.2003.00569.x

Sloan LC, Barron EJ (1992) A comparison of Eocene climate model results to quantified paleoclimatic interpretations Palaeogeography Palaeoclimatology Palaeoecology 93 (3-4):183-202. doi:10.1016/0031-0182(92)90096-n

Solomon S, Change IPoC, I. IPoCCWG (2007) Climate Change 2007 - The Physical Science Basis: Working Group I Contribution to the Fourth Assessment Report of the IPCC. Cambridge University Press

Street-Perrott FA, Huang YS, Perrott RA, Eglinton G, Barker P, BenKhelifa L, Harkness DD, Olago DO (1997) Impact of lower atmospheric carbon dioxide on tropical mountain ecosystems. Science 278 (5342):1422-1426. doi:10.1126/science.278.5342.1422

Taylor KE, Stouffer RJ, Meehl GA (2012) An overview of CMIP5 and the experiment design. Bulletin of the American Meteorological Society 93 (4):485-498. doi:10.1175/bams-d-11-00094.1

Toscano MA, Peltier WR, Drummond R (2011) ICE-5G and ICE-6G models of postglacial relative sea-level history applied to the Holocene coral reef record of northeastern St Croix, U.S.V.I.: investigating the influence of rotational feedback on GIA processes at tropical latitudes. Quaternary Science Reviews 30 (21–22):3032-3042. doi:http://dx.doi.org/10.1016/j.quascirev.2011.07.018

Washington WM, Parkinson CL (2005) An Introduction to Three-dimensional Climate Modeling. University Science Books,

Williams J, Barry RG, Washington WM (1974) Simulation of the Atmospheric Circulation Using the NCAR Global Circulation Model with Ice Age Boundary Conditions. Journal of Applied Meteorology 13 (3):305-317. doi:10.1175/1520-0450(1974)013<0305:sotacu>2.0.co;2

Williams JW, Webb T, Shurman BN, Bartlein PJ (2000) Do low CO2 concentrations affect pollen-based reconstructions of LGM climates? A response to "Physiological significance of low atmospheric CO2 for plant-climate interactions" by Cowling and Sykes. Quaternary Research 53 (3):402-404. doi:10.1006/qres.2000.2131

Wu H, Guiot J, Brewer S, Guo Z (2007) Climatic changes in Eurasia and Africa at the last glacial maximum and mid-Holocene: reconstruction from pollen data using inverse vegetation modelling. Climate Dynamics 29 (2-3):211-229. doi:10.1007/s00382-007-0231-3

Chapter II

Bartlein, P. J., et al. (2011), Pollen-based continental climate reconstructions at 6 and 21 ka: a global synthesis, *Climate Dynamics*, *37*(3-4), 775-802.

Boer, G. J. (2011), The ratio of land to ocean temperature change under global warming, *Climate Dynamics*, *37*(11-12), 2253-2270.

Braconnot, P., S. P. Harrison, M. Kageyama, P. J. Bartlein, V. Masson-Delmotte, A. Abe-Ouchi, B. Otto-Bliesner, and Y. Zhao (2012), Evaluation of climate models using palaeoclimatic data, *Nature Climate Change*, *2*(6), 417-424.

Braconnot, P., et al. (2007), Results of PMIP2 coupled simulations of the Mid-Holocene and Last Glacial Maximum - Part 1: experiments and large-scale features, *Climate of the Past*, *3*(2), 261-277.

Brohan, P., J. J. Kennedy, I. Harris, S. F. B. Tett, and P. D. Jones (2006), Uncertainty estimates in regional and global observed temperature changes: A new data set from 1850, *Journal of Geophysical Research: Atmospheres*, *111*(D12), D12106.

Dowsett, H. J., et al. (2012), Assessing confidence in Pliocene sea surface temperatures to evaluate predictive models, *Nature Clim. Change*, *2*(5), 365-371.

Dwyer, J., B. Biasutti, and A. Sobel (2012), Projected changes in the seasonal cycle of surface temperature, *Journal of Climate*.

Fasullo, J. T. (2010), Robust Land-Ocean Contrasts in Energy and Water Cycle Feedbacks, *Journal of Climate*, *23*(17), 4677-4693.

Gleckler, P. J., K. E. Taylor, and C. Doutriaux (2008), Performance metrics for climate models, *Journal of Geophysical Research: Atmospheres*, *113*(D6), D06104.

Hargreaves, J. C., A. Abe-Ouchi, and J. D. Annan (2007), Linking glacial and future climates through an ensemble of GCM simulations, *Climate of the Past*, *3*(1), 77-87.

Holland, M. M., and C. M. Bitz (2003), Polar amplification of climate change in coupled models, *Climate Dynamics*, *21*(3-4), 221-232.

Joshi, M. M., J. M. Gregory, M. J. Webb, D. M. H. Sexton, and T. C. Johns (2008), Mechanisms for the land/sea warming contrast exhibited by simulations of climate change, *Climate Dynamics*, *30*(5), 455-465.

Laine, A., M. Kageyama, P. Braconnot, and R. Alkama (2009), Impact of Greenhouse Gas Concentration Changes on Surface Energetics in IPSL-CM4: Regional Warming Patterns, Land-Sea Warming Ratios, and Glacial-Interglacial Differences, *Journal of Climate*, *22*(17), 4621-4635.

Leduc, G., R. Schneider, J.-H. Kim, and G. Lohmann (2010), Holocene and Eemian sea surface temperature trends as revealed by alkenone and Mg/Ca paleothermometry, *Quaternary Science Reviews*, *29*(7-8), 989-1004.

Lu, J., and M. Cai (2009), Seasonality of polar surface warming amplification in climate simulations, *Geophysical Research Letters*, *36*.

MARGO Project Members (2009), Constraints on the magnitude and patterns of ocean cooling at the Last Glacial Maximum, *Nature Geoscience*, *2*(2), 127-132.

Masson-Delmotte, V., et al. (2006), Past and future polar amplification of climate change: climate model intercomparisons and ice-core constraints, *Climate Dynamics*, *26*(5), 513-529.

McArdle, B. H. (1988), The structural relationship: regression in biology, *Canadian Journal of Zoology*, *66*(11), 2329-2339.

Meehl, G.A., et al. (2007), Global Climate Projections. In: Climate Change 2007: The Physical Science Basis. Contribution of Working Group I to the Fourth Assessment Report of the Intergovernmental Panel on Climate Change, edited by S. Solomon, D. Qin, M. Manning, Z. Chen, M. Marquis, K.B. Averyt, M. Tignor and H.L. Miller. Cambridge University Press, Cambridge, United Kingdom and New York, NY, USA.

Miller, G. H., R. B. Alley, J. Brigham-Grette, J. J. Fitzpatrick, L. Polyak, M. C. Serreze, and J. W. C. White (2010), Arctic amplification: can the past constrain the future?, *Quaternary Science Reviews*, *29*(15-16), 1779-1790.

Schmittner, A., N. M. Urban, J. D. Shakun, N. M. Mahowald, P. U. Clark, P. J. Bartlein, A. C. Mix, and A. Rosell-Melé (2011), Climate Sensitivity Estimated from Temperature Reconstructions of the Last Glacial Maximum, *Science*, *334*(6061), 1385-1388.

Screen, J. A., and I. Simmonds (2010), Increasing fall-winter energy loss from the Arctic Ocean and its role in Arctic temperature amplification, *Geophysical Research Letters*, *37*.

Serreze, M. C., and R. G. Barry (2011), Processes and impacts of Arctic amplification: A research synthesis, *Global and Planetary Change*, *77*(1-2), 85-96.

Solomon, A. (2006), Impact of latent heat release on polar climate, *Geophysical Research Letters*, *33*(7).

Stine, A. R., P. Huybers, and I. Y. Fung (2009), Changes in the phase of the annual cycle of surface temperature, *Nature*, *457*(7228), 435-U431.

Sutton, R. T., B. Dong, and J. M. Gregory (2007), Land/sea warming ratio in response to climate change: IPCC AR4 model results and comparison with observations, *Geophysical Research Letters*, *34*(2).

Taylor, K. E., R. J. Stouffer, and G. A. Meehl (2012), An overview of CMIP5 and the experiment design, *Bulletin of the American Meteorological Society*, *93*(4), 485-498.

Winton, M. (2006), Amplified Arctic climate change: What does surface albedo feedback have to do with it?, *Geophysical Research Letters*, *33*(3).

Chapter III

Abbot DS, Walker CC, Tziperman E (2009) Can a Convective Cloud Feedback Help to Eliminate Winter Sea Ice at High CO2 Concentrations? Journal of Climate 22 (21):5719-5731. doi:10.1175/2009jcli2854.1

Alexeev VA, Langen PL, Bates JR (2005) Polar amplification of surface warming on an aquaplanet in "ghost forcing" experiments without sea ice feedbacks. Climate Dynamics 24 (7-8):655-666. doi:10.1007/s00382-005-0018-3

Biasutti M, Sobel AH (2009) Delayed Sahel rainfall and global seasonal cycle in a warmer climate. Geophysical Research Letters 36. doi:10.1029/2009gl041303

Braconnot P, Harrison SP, Kageyama M, Bartlein PJ, Masson-Delmotte V, Abe-Ouchi A, Otto-Bliesner B, Zhao Y (2012) Evaluation of climate models using palaeoclimatic data. Nature Climate Change 2 (6):417-424. doi:10.1038/nclimate1456

Brady EC, Otto-Bliesner BL, Kay JE, Rosenbloom N (2013) Sensitivity to glacial forcing in the CCSM4. Journal of Climate 26 (6):1901-1925. doi:10.1175/jcli-d-11-00416.1

Byrne MP, O'Gorman PA (2013a) Land-ocean warming contrast over a wide range of climates: convective quasi-equilibrium theory and idealized simulations Journal of Climate. doi:10.1175/JCLI-D-12-00262.1

Byrne MP, O'Gorman PA (2013b) Link between land-ocean warming contrast and surface relative humidities in simulations with coupled climate models. Geophysical Research Letters:n/a-n/a. doi:10.1002/grl.50971

Compo GP, Sardeshmukh PD (2009) Oceanic influences on recent continental warming. Climate Dynamics 32 (2-3):333-342. doi:10.1007/s00382-008-0448-9

Deser C, Tomas R, Alexander M, Lawrence D (2010) The Seasonal Atmospheric Response to Projected Arctic Sea Ice Loss in the Late Twenty-First Century. Journal of Climate 23 (2):333-351. doi:10.1175/2009jcli3053.1

Dong B, Gregory JM, Sutton RT (2009) Understanding Land-Sea Warming Contrast in Response to Increasing Greenhouse Gases. Part I: Transient Adjustment. Journal of Climate 22 (11):3079-3097. doi:10.1175/2009jcli2652.1

Dowsett HJ, Robinson MM, Haywood AM, Hill DJ, Dolan AM, Stoll DK, Chan W-L, Abe-Ouchi A, Chandler MA, Rosenbloom NA, Otto-Bliesner BL, Bragg FJ, Lunt DJ, Foley KM, Riesselman CR (2012) Assessing confidence in Pliocene sea surface temperatures to evaluate predictive models. Nature Clim Change 2 (5):365-371. doi:http://www.nature.com/nclimate/journal/v2/n5/abs/nclimate1455.html#supplementary-information

Dwyer J, Biasutti B, Sobel A (2012) Projected changes in the seasonal cycle of surface temperature. Journal of Climate. doi:10.1175/JCLI-D-11-00741.1

Fasullo JT (2010) Robust Land-Ocean Contrasts in Energy and Water Cycle Feedbacks. Journal of Climate 23 (17):4677-4693. doi:10.1175/2010jcli3451.1

Gleckler PJ, Taylor KE, Doutriaux C (2008) Performance metrics for climate models. Journal of Geophysical Research-Atmospheres 113 (D6). doi:10.1029/2007jd008972

Graversen RG, Mauritsen T, Tjernstrom M, Kallen E, Svensson G (2008) Vertical structure of recent Arctic warming. Nature 451 (7174):53-U54. doi:10.1038/nature06502

Graversen RG, Wang M (2009) Polar amplification in a coupled climate model with locked albedo. Climate Dynamics 33 (5):629-643. doi:10.1007/s00382-009-0535-6

Hall A (2004) The role of surface albedo feedback in climate. Journal of Climate 17 (7):1550-1568. doi:10.1175/1520-0442(2004)017<1550:trosaf>2.0.co;2

Harrison SP, Bartlein PJ, Brewer S, Prentice IC, Boyd M, Hessler I, Holmgren K, Izumi K, Willis K (2013) Climate model benchmarking with glacial and mid-Holocene climates. Climate Dynamics:1-18. doi:10.1007/s00382-013-1922-6

Holland MM, Bitz CM (2003) Polar amplification of climate change in coupled models. Climate Dynamics 21 (3-4):221-232. doi:10.1007/s00382-003-0332-6

Holland MM, Bitz CM, Tremblay B, Bailey DA (2008) The role of natural versus forced change in future rapid summer Arctic ice loss. In: DeWeaver ET, Bitz CM, Tremblay L-B (eds) Arctic sea ice decline: observatios, projections, mechanisms, and implications. American Geophysical Union, Washington, D. C.,

Izumi K, Bartlein PJ, Harrison SP (2013) Consistent large-scale temperature responses in warm and cold climates. Geophysical Research Letters 40 (9):1817-1823. doi:10.1002/grl.50350

Jackson JM, Carmack EC, McLaughlin FA, Allen SE, Ingram RG (2010) Identification, characterization, and change of the near-surface temperature maximum in the Canada Basin, 1993-2008. Journal of Geophysical Research-Oceans 115. doi:10.1029/2009jc005265

Jin M, Liang S (2006) An improved land surface emissivity parameter for land surface models using global remote sensing observations. Journal of Climate 19 (12):2867-2881. doi:10.1175/jcli3720.1

Joshi M, Gregory J (2008) Dependence of the land-sea contrast in surface climate response on the nature of the forcing. Geophysical Research Letters 35 (24). doi:10.1029/2008gl036234

Joshi MM, Gregory JM, Webb MJ, Sexton DMH, Johns TC (2008) Mechanisms for the land/sea warming contrast exhibited by simulations of climate change. Climate Dynamics 30 (5):455-465. doi:10.1007/s00382-007-0306-1

Joshi MM, Lambert FH, Webb MJ (2013) An explanation for the difference between twentieth and twenty-first century land–sea warming ratio in climate models. Climate Dynamics 41 (7-8):1853-1869. doi:10.1007/s00382-013-1664-5

Kageyama M, Braconnot P, Bopp L, Mariotti V, Roy T, Woillez M-N, Caubel A, Foujols M-A, Guilyardi E, Khodri M, Lloyd J, Lombard F, Marti O (2013) Mid-Holocene and last glacial maximum climate simulations with the IPSL model: part II: model-data comparisons. Climate Dynamics 40 (9-10):2469-2495. doi:10.1007/s00382-012-1499-5

Karl TR, Hassol SJ, Miller CD, Murray WL (2006) Temperature Trends in the Lower Atmosphere: Steps for Understanding and Reconciling Differences. Synthesis and Assessment Product 1.1. U.S. Climate Change Science Program, Washington, D.C.

Laine A, Kageyama M, Braconnot P, Alkama R (2009) Impact of Greenhouse Gas Concentration Changes on Surface Energetics in IPSL-CM4: Regional Warming Patterns, Land-Sea Warming Ratios, and Glacial-Interglacial Differences. Journal of Climate 22 (17):4621-4635. doi:10.1175/2009jcli2771.1

Langen PL, Alexeev VA (2007) Polar amplification as a preferred response in an idealized aquaplanet GCM. Climate Dynamics 29 (2-3):305-317. doi:10.1007/s00382-006-0221-x

Leibowicz BD, Abbot DS, Emanuel K, Tziperman E (2012) Correlation between present-day model simulation of Arctic cloud radiative forcing and sea ice consistent with positive winter convective cloud feedback. Journal of Advances in Modeling Earth Systems 4. doi:10.1029/2012ms000153

Li G, Harrison SP, Bartlein PJ, Izumi K, Colin Prentice I (2013) Precipitation scaling with temperature in warm and cold climates: An analysis of CMIP5 simulations. Geophysical Research Letters 40 (15):4018-4024. doi:10.1002/grl.50730

Lu J, Cai M (2009) Seasonality of polar surface warming amplification in climate simulations. Geophysical Research Letters 36. doi:10.1029/2009gl040133

Lu J, Cai M (2010) Quantifying contributions to polar warming amplification in an idealized coupled general circulation model. Climate Dynamics 34 (5):669-687. doi:10.1007/s00382-009-0673-x

Manabe S, Stouffer RJ (1980) Sensitivity of a global climate model to an incease of CO2 concentration in the atmosphere. Journal of Geophysical Research-Oceans and Atmospheres, vol 85. doi:10.1029/JC085iC10p05529

Manabe S, Stouffer RJ, Spelman MJ, Bryan K (1991) Transient responses of a coupled ocean atmosphere model to gradual chnages of atmospheric CO2. 1. Annual mean response. Journal of Climate 4 (8):785-818. doi:10.1175/1520-0442(1991)004<0785:troaco>2.0.co;2

Mann ME, Park J (1996) Greenhouse warming and changes in the seasonal cycle of temperature: Model versus observations. Geophysical Research Letters 23 (10):1111-1114. doi:10.1029/96gl01066

Masson-Delmotte V, Kageyama M, Braconnot P, Charbit S, Krinner G, Ritz C, Guilyardi E, Jouzel J, Abe-Ouchi A, Crucifix M, Gladstone RM, Hewitt CD, Kitoh A, LeGrande AN, Marti O, Merkel U, Motoi T, Ohgaito R, Otto-Bliesner B, Peltier WR, Ross I, Valdes PJ, Vettoretti G, Weber SL, Wolk F, Yu Y (2006) Past and future polar amplification of climate change: climate model intercomparisons and ice-core constraints. Climate Dynamics 26 (5):513-529. doi:10.1007/s00382-005-0081-9

Oke TR (1987) Boundary Layer Climates. second edn. Routledge, London and New York

Otto-Bliesner BL, Marsha SJ, Overpeck JT, Miller GH, Hu AX, Mem CLIP (2006) Simulating arctic climate warmth and icefield retreat in the last interglaciation. Science 311 (5768):1751-1753. doi:10.1126/science.1120808

Pithan F, Mauritsen T (2014) Arctic amplification dominated by temperature feedbacks in contemporary climate models. Nature Geosci 7 (3):181-184. doi:10.1038/ngeo2071

Santer BD, Wigley TML, Mears C, Wentz FJ, Klein SA, Seidel DJ, Taylor KE, Thorne PW, Wehner MF, Gleckler PJ, Boyle JS, Collins WD, Dixon KW, Doutriaux C, Free M, Fu Q, Hansen JE, Jones GS, Ruedy R, Karl TR, Lanzante JR, Meehl GA, Ramaswamy V, Russell G, Schmidt GA (2005) Amplification of surface temperature trends and variability in the tropical atmosphere. Science 309 (5740):1551-1556. doi:10.1126/science.1114867

Santer BD, Mears C, Wentz FJ, Taylor KE, Gleckler PJ, Wigley TML, Barnett TP, Boyle JS, Brüggemann W, Gillett NP, Klein SA, Meehl GA, Nozawa T, Pierce DW, Stott PA, Washington WM, Wehner MF (2007) Identification of human-induced changes in atmospheric moisture content. Proceedings of the National Academy of Sciences 104 (39):15248-15253. doi:10.1073/pnas.0702872104

Screen JA, Simmonds I (2010a) The central role of diminishing sea ice in recent Arctic temperature amplification. Nature 464 (7293):1334-1337. doi:10.1038/nature09051

Screen JA, Simmonds I (2010b) Increasing fall-winter energy loss from the Arctic Ocean and its role in Arctic temperature amplification. Geophysical Research Letters 37. doi:10.1029/2010gl044136

Serreze MC, Barry RG (2011) Processes and impacts of Arctic amplification: A research synthesis. Global and Planetary Change 77 (1-2):85-96. doi:10.1016/j.gloplacha.2011.03.004

Serreze MC, Barrett AP, Stroeve JC, Kindig DN, Holland MM (2009) The emergence of surface-based Arctic amplification. Cryosphere 3 (1):11-19

Shupe MD, Intrieri JM (2004) Cloud radiative forcing of the Arctic surface: The influence of cloud properties, surface albedo, and solar zenith angle. Journal of Climate 17 (3):616-628. doi:10.1175/1520-0442(2004)017<0616:crfota>2.0.co;2

Sobel AH, Bretherton CS (2000) Modeling tropical precipitation in a single column. Journal of Climate 13 (24):4378-4392. doi:10.1175/1520-0442(2000)013<4378:mtpias>2.0.co;2

Sobel AH, Camargo SJ (2011) Projected Future Seasonal Changes in Tropical Summer Climate. Journal of Climate 24 (2):473-487. doi:10.1175/2010jcli3748.1

Soden BJ, Broccoli AJ, Hemler RS (2004) On the use of cloud forcing to estimate cloud feedback. Journal of Climate 17 (19):3661-3665. doi:10.1175/1520-0442(2004)017<3661:otuocf>2.0.co;2

Solomon A (2006) Impact of latent heat release on polar climate. Geophysical Research Letters 33 (7). doi:10.1029/2005gl025607

Stine AR, Huybers P (2012) Changes in the Seasonal Cycle of Temperature and Atmospheric Circulation. Journal of Climate 25 (21):7362-7380. doi:10.1175/jcli-d-11-00470.1

Stine AR, Huybers P, Fung IY (2009) Changes in the phase of the annual cycle of surface temperature. Nature 457 (7228):435-U431. doi:10.1038/nature07675

Sutton RT, Dong B, Gregory JM (2007) Land/sea warming ratio in response to climate change: IPCC AR4 model results and comparison with observations. Geophysical Research Letters 34 (2). doi:10.1029/2006gl028164

Taylor KE, Stouffer RJ, Meehl GA (2012) AN OVERVIEW OF CMIP5 AND THE EXPERIMENT DESIGN. Bulletin of the American Meteorological Society 93 (4):485-498. doi:10.1175/bams-d-11-00094.1

Taylor PC, Cai M, Hu A, Meehl J, Washington W, Zhang GJ (2013) A Decomposition of Feedback Contributions to Polar Warming Amplification. Journal of Climate 26 (18):7023-7043. doi:10.1175/jcli-d-12-00696.1

Thomson DJ (1995) THE SEASONS, GLOBAL TEMPERATURE, AND PRECESSION. Science 268 (5207):59-68. doi:10.1126/science.268.5207.59

Wallace CJ, Osborn TJ (2002) Recent and future modulation of the annual cycle. Climate Research 22 (1):1-11. doi:10.3354/cr022001

Wilks DS (2011) Statistical methods in the atmospheric sciences, 3rd edn. International geophysics series, vol 100. Academic Press, New York

Winton M (2006) Amplified Arctic climate change: What does surface albedo feedback have to do with it? Geophysical Research Letters 33 (3). doi:10.1029/2005gl025244

Chapter IV

Bartlein, P.: Past environmental changes: Characteristic features of Quaternary climate variations. In: Past and Future Rapid Environmental Changes, Huntley, B., Cramer, W., Morgan, A., Prentice, H., and Allen, J. M. (Eds.), NATO ASI Series, Springer Berlin Heidelberg, 1997.

Bartlein, P. J., Harrison, S. P., Brewer, S., Connor, S., Davis, B. A. S., Gajewski, K., Guiot, J., Harrison-Prentice, T. I., Henderson, A., Peyron, O., Prentice, I. C., Scholze, M., Seppa, H., Shuman, B., Sugita, S., Thompson, R. S., Viau, A. E., Williams, J., and Wu, H.: Pollen-based continental climate reconstructions at 6 and 21 ka: a global synthesis, Climate Dynamics, 37, 775-802, 2011.

Bartlein, P. J., Prentice, I. C., and Webb, T.: Climatic response surfaces from pollen data for some eastern North-American taxa. In: Journal of Biogeography, 1, 1986.

Blois, J. L., Williams, J. W., Grimm, E. C., Jackson, S. T., and Graham, R. W.: A methodological framework for assessing and reducing temporal uncertainty in paleovegetation mapping from late-Quaternary pollen records, Quaternary Science Reviews, 30, 1926-1939, 2011.

Bradley, R. S.: Paleoclimatology: Reconstructing Climates of the Quaternary, Elsevier/Academic Press, San Diego, 2014.

Burton, A. J., Melillo, J. M., and Frey, S. D.: Adjustment of Forest Ecosystem Root Respiration as Temperature Warms, Journal of Integrative Plant Biology, 50, 1467-1483, 2008.

Collatz, G. J., Ball, J. T., Grivet, C., and Berry, J. A.: Physiological and environmental-regulation of stomatal conductance, photosynthesis and transpiration - A model that includes a laminar boundary-layer Agricultural and Forest Meteorology, 54, 107-136, 1991.

Collatz, G. J., Ribas-Carbo, M., and Berry, J. A.: Coupled photosynthesis-stomatal conductance model for leaves of C4 plants, Australian Journal of Plant Physiology, 19, 519-538, 1992.

Cowling, S. A.: Simulated effects of low atmospheric CO2 on structure and composition of North American vegetation at the Last Glacial Maximum, Global Ecology and Biogeography, 8, 81-93, 1999.

Cowling, S. A. and Sykes, M. T.: Physiological significance of low atmospheric CO2 for plant-climate interactions, Quaternary Research, 52, 237-242, 1999.

DeFries R, Hansen M.C.: ISLSCP II Continuous Fields of Vegetation Cover, 1992-1993. In Hall, Forrest G., G. Collatz, B. Meeson, S. Los, E. Brown de Colstoun, and D. Landis (eds.). ISLSCP Initiative II Collection. Data set. Available on-line [http://daac.ornl.gov/] from Oak Ridge National Laboratory Distributed Active Archive Center, Oak Ridge, Tennessee, U.S.A. doi:10.3334/ORNLDAAC/931, 2009

Edwards, M. E., Anderson, P. M., Brubaker, L. B., Ager, T. A., Andreev, A. A., Bigelow, N. H., Cwynar, L. C., Eisner, W. R., Harrison, S. P., Hu, F. S., Jolly, D., Lozhkin, A. V., MacDonald, G. M., Mock, C. J., Ritchie, J. C., Sher, A. V., Spear, R. W., Williams, J. W., and Yu, G.: Pollen-based biomes for Beringia 18,000, 6000 and 0 C-14 yr BP, Journal of Biogeography, 27, 521-554, 2000.

Farquhar, G. D.: Carbon dioxide and vegetation, Science, 278, 1411-1411, 1997.

Farquhar, G. D., Caemmerer, S. V., and Berry, J. A.: A biochemical-model of photosynthetic CO2 assimilation in leaves of C-3 species, Planta, 149, 78-90, 1980.

Fekete, B. M., Vörösmarty, C. J., and Grabs, W.: High-resolution fields of global runoff combining observed river discharge and simulated water balances, Global Biogeochemical Cycles, 16, 15-11-15-10, 2002.

Gelman, A., Carlin, J. B., Stern, H. S., and Rubin, D. B.: Bayesian Data Analysis, Second Edition, CHAPMAN and HALL/CRC, New York, 2003.

Gonzales, L. M., Williams, J. W., and Grimm, E. C.: Expanded response-surfaces: a new method to reconstruct paleoclimates from fossil pollen assemblages that lack modern analogues, Quaternary Science Reviews, 28, 3315-3332, 2009.

Guiot, J., Torre, F., Jolly, D., Peyron, O., Boreux, J. J., and Cheddadi, R.: Inverse vegetation modeling by Monte Carlo sampling to reconstruct palaeoclimates under changed precipitation seasonality and CO2 conditions: application to glacial climate in Mediterranean region, Ecological Modelling, 127, 119-140, 2000.

Guiot, J., Wu, H. B., Garreta, V., Hatte, C., and Magny, M.: A few prospective ideas on climate reconstruction: from a statistical single proxy approach towards a multi-proxy and dynamical approach, Climate of the Past, 5, 571-583, 2009.

Haque, A.: Estimating actual areal evapotranspiration from potential evapotranspiration using physical models based on complementary relationships and meteorological data, Bulletin of Engineering Geology and the Environment, 62, 57-63, 2003.

Harris, I., Jones, P. D., Osborn, T. J., and Lister, D. H.: Updated high-resolution grids of monthly climatic observations – the CRU TS3.10 Dataset, International Journal of Climatology, 34, 623-642, 2014.

Harrison, S. P.: Paleoclimate Modeling | Data–Model Comparisons. In: Encyclopedia of Quaternary Science (Second Edition), Elias, S. A. and Mock, C. J. (Eds.), Elsevier, Amsterdam, 2013.

Harrison, S. P., Prentice, I. C., Barboni, D., Kohfeld, K. E., Ni, J., and Sutra, J.-P.: Ecophysiological and bioclimatic foundations for a global plant functional classification, Journal of Vegetation Science, 21, 300-317, 2010.

Hastings, W. K.: Monte Carlo sampling methods using Markov chains and their application, Biometrika, 57, 97-109, 1970.

Haxeltine, A. and Prentice, I. C.: BIOME3: An equilibrium terrestrial biosphere model based on ecophysiological constraints, resource availability, and competition among plant functional types, Global Biogeochemical Cycles, 10, 693-709, 1996.

Hobbins, M. T., Ramirez, J. A., Brown, T. C., and Claessens, L.: The complementary relationship in estimation of regional evapotranspiration: The Complementary Relationship Areal Evapotranspiration and Advection-Aridity models, Water Resources Research, 37, 1367-1387, 2001.

Huntingford, C. and Monteith, J. L.: The behaviour of a mixed-layer model of the convective boundary layer coupled to a big leaf model of surface energy partitioning, Boundary-Layer Meteorology, 88, 87-101, 1998.

IPCC: Climate Change 2007: The Physical Science Basis. Contribution of Working Group I to the Fourth Assessment Report of the Intergovernmental Panel on Climate Change. Solomon, S., Qin, D., Manning, M., Chen, Z., Marquis, M., Averyt, K. B., Tingnor, M., and Miller, M. L. (Eds.), Cambridge University Press, Cambridge, United Kingdom and New York, NY, USA, 2007.

IPCC: Climate Change 2013: The Physical Science Basis. Contribution of Working Group I to the Fifth Assessment Report of the Intergovernmental Panel on Climate Change Stocker, T. F., Qin, D., Plattner, G.-K., Tignor, M., Allen, S. K., Boschung, J., Nauels, A., Xia, Y., Bex, V., and Midgley, P. M. (Eds.), Cambridge University Press, Cambridge, United Kingdom and New York, NY, USA, 2013.

Jackson, S. T. and Williams, J. W.: Modern analogs in Quaternary paleoecology: Here today, gone yesterday, gone tomorrow?, Annual Review of Earth and Planetary Sciences, 32, 495-537, 2004.

Jolly, D. and Haxeltine, A.: Effect of low glacial atmospheric CO2 on tropical African montane vegetation, Science, 276, 786-788, 1997.

Kaplan, J. O., Bigelow, N. H., Prentice, I. C., Harrison, S. P., Bartlein, P. J., Christensen, T. R., Cramer, W., Matveyeva, N. V., McGuire, A. D., Murray, D. F., Razzhivin, V. Y., Smith, B., Walker, D. A., Anderson, P. M., Andreev, A. A., Brubaker, L. B., Edwards, M. E., and Lozhkin, A. V.: Climate change and Arctic ecosystems: 2. Modeling, paleodata-model comparisons, and future projections, Journal of Geophysical Research-Atmospheres, 108, 2003.

Kelley, D. I., Prentice, I. C., Harrison, S. P., Wang, H., Simard, M., Fisher, J. B., and Willis, K. O.: A comprehensive benchmarking system for evaluating global vegetation models, Biogeosciences, 10, 3313-3340, 2013.

Kohfeld, K. E. and Harrison, S. P.: How well can we simulate past climates? Evaluating the models using global palaeoenvironmental datasets, Quaternary Science Reviews, 19, 321-346, 2000.

Li, G., Harrison, S. P., Bartlein, P. J., Izumi, K., and Colin Prentice, I.: Precipitation scaling with temperature in warm and cold climates: An analysis of CMIP5 simulations, Geophysical Research Letters, 40, 4018-4024, 2013.

Metropolis, N., Rosenbluth, A. W., Rosenbluth, M. N., Teller, A. H., and Teller, E.: Equation of State Calculations by Fast Computing Machines, Journal of Chemical Physics, 21, 1087-1092, 1953.

Monteith, J. L.: Accommodation between transpiring vegetation and the convective boundary-layer Journal of Hydrology, 166, 251-263, 1995.

New, M., Lister, D., Hulme, M., and Makin, I.: A high-resolution data set of surface climate over global land areas, Climate Research, 21, 1-25, 2002.

Ni, J., Yu, G., Harrison, S. P., and Prentice, I. C.: Palaeovegetation in China during the late Quaternary: Biome reconstructions based on a global scheme of plant functional types, Palaeogeography Palaeoclimatology Palaeoecology, 289, 44-61, 2010.

Overpeck, J. T., Webb, T., and Prentice, I. C.: Quantitative interpretation of fossil pollen spectra - dissimilarity coefficients and the method of modern analogs. In: Quaternary Research, 1, 1985.

Peyron, O., Guiot, J., Cheddadi, R., Tarasov, P., Reille, M., de Beaulieu, J. L., Bottema, S., and Andrieu, V.: Climatic reconstruction in Europe for 18,000 yr B.P. from pollen data, Quaternary Research, 49, 183-196, 1998.

Prentice, I. C., Cramer, W., Harrison, S. P., Leemans, R., Monserud, R. A., and Solomon, A. M.: A global biome model based on plant physiology and dominance, soil properties and climate, Journal of Biogeography, 19, 117-134, 1992.

Prentice, I. C. and Harrison, S. P.: Ecosystem effects of CO2 concentration: evidence from past climates, Climate of the Past, 5, 297-307, 2009.

Prentice, I. C. and Webb, T.: BIOME 6000: reconstructing global mid-Holocene vegetation patterns from palaeoecological records, Journal of Biogeography, 25, 997-1005, 1998.

Priestley, C. H. B. and Taylor, R. J.: Assessment of surface heat-flux and evaporation using large-scale parameters, Monthly Weather Review, 100, 81-92, 1972.

Raupach, M. R.: Combination theory and equilibrium evaporation, Quarterly Journal of the Royal Meteorological Society, 127, 1149-1181, 2001.

Sloan, L. C. and Barron, E. J.: A comparison of Eocene climate model results to quantified paleoclimatic interpretations Palaeogeography Palaeoclimatology Palaeoecology, 93, 183-202, 1992.

Street-Perrott, F. A., Huang, Y. S., Perrott, R. A., Eglinton, G., Barker, P., BenKhelifa, L., Harkness, D. D., and Olago, D. O.: Impact of lower atmospheric carbon dioxide on tropical mountain ecosystems, Science, 278, 1422-1426, 1997.

Taylor, K. E.: Summarizing multiple aspects of model performance in a single diagram, Journal of Geophysical Research: Atmospheres, 106, 7183-7192, 2001.

Taylor, K. E., Stouffer, R. J., and Meehl, G. A.: An overview of CMIP5 and the experiment design, Bulletin of the American Meteorological Society, 93, 485-498, 2012.

Thompson, R. S. and Anderson, K. H.: Biomes of western North America at 18,000, 6000 and 0 C-14 yr BP reconstructed from pollen and packrat midden data, Journal of Biogeography, 27, 555-584, 2000.

Thornthwaite, C. W. and Mather, J. R.: The water balance, s.n., Centerton, N.J., 1955.

Thornthwaite, C. W., Mather, J. R., Carter, D. B., and Drexel Institute of Technology: Instructions and tables for computing potential evapotranspiration and the water balance, Drexel Institute of Technology, Laboratory of Climatology, Centerton, N.J., 1957.

Viau, A. E., Gajewski, K., Sawada, M. C., and Fines, P.: Millennial-scale temperature variations in North America during the Holocene, Journal of Geophysical Research: Atmospheres, 111, D09102, 2006.

Williams, J. W.: Variations in tree cover in North America since the last glacial maximum, Global and Planetary Change, 35, 1-23, 2003.

Williams, J. W., Shuman, B. N., Webb, T., Bartlein, P. J., and Leduc, P. L.: Late-quaternary vegetation dynamics in north america: Scaling from taxa to biomes, Ecological Monographs, 74, 309-334, 2004.

Williams, J. W., Summers, R. L., and Webb Iii, T.: Applying plant functional types to construct biome maps from eastern North American pollen data: comparisons with model results, Quaternary Science Reviews, 17, 607-627, 1998.

Williams, J. W., Webb, T., Richard, P. H., and Newby, P.: Late Quaternary biomes of Canada and the eastern United States, Journal of Biogeography, 27, 585-607, 2000.

Willmott, C. J. and Feddema, J. J.: A More Rational Climatic Moisture Index*, The Professional Geographer, 44, 84-88, 1992.

Wu, H., Guiot, J., Brewer, S., and Guo, Z.: Climatic changes in Eurasia and Africa at the last glacial maximum and mid-Holocene: reconstruction from pollen data using inverse vegetation modelling, Climate Dynamics, 29, 211-229, 2007.

Wu, H., Guiot, J., Peng, C., and Guo, Z.: New coupled model used inversely for reconstructing past terrestrial carbon storage from pollen data: validation of model using modern data, Global Change Biology, 15, 82-96, 2009.

Zhao, M., Heinsch, F. A., Nemani, R. R., and Running, S. W.: Improvements of the MODIS terrestrial gross and net primary production global data set, Remote Sensing of Environment, 95, 164-176, 2005.

Zhao, M. and Running, S. W.: Drought-Induced Reduction in Global Terrestrial Net Primary Production from 2000 Through 2009, Science, 329, 940-943, 2010.

Chapter V

Bartlein PJ, Harrison SP, Brewer S, Connor S, Davis BAS, Gajewski K, Guiot J, Harrison-Prentice TI, Henderson A, Peyron O, Prentice IC, Scholze M, Seppa H, Shuman B, Sugita S, Thompson RS, Viau AE, Williams J, Wu H (2011) Pollen-based continental climate reconstructions at 6 and 21 ka: a global synthesis. Climate Dynamics 37 (3-4):775-802. doi:10.1007/s00382-010-0904-1

Harrison SP (2013) Paleoclimate Modeling | Data–Model Comparisons. In: Elias SA, Mock CJ (eds) Encyclopedia of Quaternary Science (Second Edition). Elsevier, Amsterdam, pp 135-146. doi:http://dx.doi.org/10.1016/B978-0-444-53643-3.00007-8

IPCC (2007) Climate Change 2007: The Physical Science Basis. Contribution of Working Group I to the Fourth Assessment Report of the Intergovernmental Panel on Climate Change. In: Solomon S, Qin D, Manning M et al. (eds). Cambridge University Press, Cambridge, United Kingdom and New York, NY, USA, p 996

IPCC (2013) Climate Change 2013: The Physical Science Basis. Contribution of Working Group I to the Fifth Assessment Report of the Intergovernmental Panel on Climate Change In: Stocker TF, Qin D, Plattner G-K et al. (eds). Cambridge University Press, Cambridge, United Kingdom and New York, NY, USA, p 1535